Characterization of Sulfur-Rich Microbial Organic Matter in Jurassic Carbonates Using Laser-Assisted Mass Spectrometry

Siveen Thlaijeh, Kevin Lepot, Yvain Carpentier, Armelle Riboulleau, Dumitru Duca, Marin Vojkovic, Anuradha Tewari, Johan Sarazin, Mathilde Bon, Nicolas Nuns, et al.

Characterization of sulfur-rich microbial organic matter in Jurassic carbonates using laser-assisted mass spectrometry

S. Thlaijeh[1, 2], K. Lepot[2, 3, *], Y. Carpentier[1], A. Riboulleau[2], D. Duca[1], M. Vojkovic[1,4], A. Tewari[2], J. Sarazin[5], M. Bon[1,2,6], N. Nuns[7], N. Tribovillard[2], C. Focsa[1]

This is the accepted version of the following article: Thlaijeh S, Lepot K, Carpentier Y, et al. Characterization of Sulfur-Rich Microbial Organic Matter in Jurassic Carbonates Using Laser-Assisted Mass Spectrometry. Astrobiology 2024;24(1), *which has now been formally published in final form at* **Astrobiology** *at* **https://doi.org/10.1089/ast.2023.0008 .**

[1] Univ. Lille, CNRS, UMR 8523 - PhLAM - Physique des Lasers Atomes et Molécules, F-59000 Lille, France

[2] Univ. Lille, CNRS, Univ. Littoral Côte d'Opale, UMR 8187 - LOG – Laboratoire d'Océanologie et de Géosciences, F-59000 Lille, France

[3] Institut Universitaire de France (IUF)

[4] Department of Physics, Faculty of Science, University of Split, Ruđera Boškovića 33, 21 000 Split, Croatia

[5] Univ. Lille, CNRS, INRAE, Centrale Lille, UMR 8207 - UMET - Unité Matériaux et Transformations, F-59000 Lille, France

[6] Department of Geology (WE13), Ghent University, Krijgslaan 281/S8, Ghent, 9000, Belgium

[7] Univ. Lille, CNRS, INRAE, Centrale Lille, Univ. Artois, FR 2638 - IMEC - Institut Michel-Eugène Chevreul, F-59000 Lille, France

* Corresponding author: kevin.lepot@univ-lille.fr

Short running title: laser mass spectrometry of sulfurized OM

Keywords: laser mass spectrometry, desorption-ionization, biosignatures, sulfurized organic matter, microbial mats, thiophenes

Laser desorption-ionization mass spectrometry shows great potential for *in situ* molecular analysis of planetary surfaces and microanalysis of space-returned samples or (micro)fossils. Coupled with pyrolysis gas chromatography-mass spectrometry (Py-GC-MS) in ESA's ExoMars project, this technique could help assess further the origin of sulfur-bearing organic matter (OM) recently detected on Mars. To unravel this potential, we analyzed sulfurized microbial OM from ca. 150 million year-old carbonates with laser desorption-ionization mass spectrometry (single- and two-step: LDI-MS and L2MS), in comparison with time-of-flight secondary-ion mass spectrometry (ToF-SIMS), GC-MS, and Py-GC-MS. We show that LDI-MS and L2MS readily detect sulfur-bearing moieties such as (alkyl)thiophenes and (alkyl)benzothiophenes. The mineral matrix, however, made the identification of sulfur-bearing molecules challenging in our L2MS experiment. The dominance of small aromatic hydrocarbons (≤14 carbons) in the LDI-MS and L2MS of the extracted soluble and insoluble OM and of the bulk rock is consistent with the low thermal maturity of the sediment, and contrasts with the predominance of larger polycyclic aromatic structures commonly observed in meteorites with these techniques. We detected inorganic ions, in particular VO^+, in demineralized OM that likely originate from geoporphyrins, which derive from chlorophylls during sediment diagenesis. Finally, insoluble OM yielded distinct compositions compared to extracted soluble OM, with a greater abundance of ions of m/z over 175 and additional N-moieties. This highlights the potential of laser-assisted mass spectrometry to decipher the composition of macromolecular OM, in particular to investigate the preservation of biomacromolecules in microfossils. Studies comparing diverse biogenic and abiogenic OM are needed to further assess the use of this technique to search for biosignatures.

1. Introduction

Chlorinated (Freissinet et al., 2015; Szopa et al., 2020) and sulfurized (Eigenbrode et al., 2018) organic molecules have been detected on Mars by the Sample Analysis at Mars (SAM) instrument suite (Mahaffy et al., 2012) using evolved gas analysis and pyrolysis gas chromatography-mass spectrometry (Py-GC-MS). The detected S-bearing molecules included thiophene (C_4H_4S) and methylated thiophenes (C_5H_6S, C_6H_8S) (Eigenbrode et al., 2018). Thiophenic moieties are common products of diagenetic addition of sulfur to organic matter (Sinninghe Damsté and de Leeuw, 1990; Werne et al., 2004) observed in bitumen extracts and pyrolysates of kerogen (solvent-insoluble organic matter) (van Kaam-Peters and Sinninghe Damsté, 1997; Mongenot et al., 1999; Riboulleau et al., 2000). Thiophenes can be preserved in low-grade metamorphic rocks for up to 2.7 billion years (Lepot et al., 2019). Sulfurization protects organic matter (OM) against diagenetic (bio)degradation (Sinninghe Damsté and de Leeuw, 1990) and may have contributed to the preservation of the OM in 3 billion-year-old sediments on Mars (Eigenbrode et al., 2018). It is thus desirable to further study sulfurized sedimentary OM using analytical methods that can be carried on *in situ* planetary investigations, as well as methods that could minimize sample destruction for precious samples, e.g., those that may be recovered from Mars.

Laser mass spectrometry is among those methods (Goesmann et al., 2017; Ligterink et al., 2021, 2020). Two-step laser mass spectrometry (L2MS) couples laser desorption/ablation (LD), laser ionization (LI), and mass spectrometry (MS) traditionally using time-of-flight (ToF) mass spectrometers (Clemett and Zare, 1996). The first laser step is used to transfer from condensed to gas phase a fraction of the sample through desorption and/or ablation, preserving as much as possible the intact molecular compounds. The second laser beam intercepts and ionizes gas-phase neutrals. Ions are then separated according to their mass-to-charge ratio (m/z) in the ToF-MS. Depending on the sample nature and experimental conditions (Donnarumma et al., 2021), desorption and ionization may also occur with a single laser, the technique is then usually referred to as laser-desorption-ionization (LDI). The use of post-desorption ionization laser pulse can help minimize the energy used for desorption and minimize aggregation of ions and neutrals (Hurtado et al., 2010) and/or break up such aggregates (e.g., for inorganics: Tulej et al., 2018).

Secondary ion mass spectrometry uses focused ion beams to sputter charged particles that are analyzed by ToF-MS in ToF-SIMS (Thiel and Sjövall, 2015), although the high energy of primary ions accelerated at kilovolts yields more extensive molecular fragmentation than the low-energy of photons (e.g., 4.66 eV at 266 nm).

An advantage over some other mass spectrometric techniques is that these techniques require little sample preparation (although flat samples are required for ToF-SIMS: Fadel et al., 2020). Moreover, focusing of incident laser/ion beams allows spatially-resolved analyses in both types of techniques. This provides important applications, complementary to other bulk-rock MS techniques, in planetary science and paleontology. ToF-SIMS has been carried aboard the Rosetta spacecraft and used to detect and image small carbonaceous molecule fragments in particles sampled *in situ* in a comet (Fray et al., 2016). It has also been used to identify and localize macromolecules in fossils such as melanin in reptile skins up to 196 Ma (million years) old (Lindgren et al., 2014), blood-derived porphyrins in 46 Ma mosquitos (Greenwalt et al., 2013) and to characterize and image microbial OM in Jurassic rocks (Fadel et al., 2020). An LDI-ion-trap-MS instrument has been integrated to the Mars Organic Molecule Analyzer instrument for the ExoMars mission (MOMA, Goesmann et al., 2017). LDI-MS and L2MS relying on ToF-MS have been used to characterize meteoritic OM (Messenger et al., 1998;

Sabbah et al., 2010), cometary dust recovered by the Stardust spacecraft (Sandford et al., 2010), as well as sedimentary OM (Mahajan et al., 2001; Pomerantz et al., 2008; Sabbah et al., 2011; Schultz et al., 2014; Smaniotto et al., 2008; Zhan et al., 1997). Those studies allowed detailed analysis of polycyclic aromatic hydrocarbons (PAHs) and/or other aromatic moieties, helped by the high sensitivity to aromatic moieties offered by resonance-enhanced multiphoton ionization at ~266 nm (REMPI, Boesl and Zimmermann, 2021; Clemett and Zare, 1996).

Traditional ToF-MS instruments provide a low mass resolution (commonly m/Δm ~<2000; Faccinetto et al., 2015) that limit the distinction of molecules with similar nominal (integer value) masses (Briois et al., 2016), in particular in complex mixtures with mass/charge ratios well above 150 (Smaniotto et al., 2008). More recently, radiofrequency-driven ion trap/guides coupled to ToF-MS, Orbitrap™ MS and FT-ICR (Fourier-transform ion cyclotron resonance) MS provide increased mass resolution (m/Δm) of ~5–50k, ~20–400k and 0.5–1+M, respectively (Gross, 2017). These methods may be used for *in situ* cosmochemistry/planetary missions, as exemplified by the recent development of the laser-ablation/-desorption CosmOrbitrap system (Arevalo et al., 2023; Briois et al., 2016; Selliez et al., 2019). LDI-FTICR-MS has been used to characterize the soluble fraction (bitumen) of fossil OM (Cho et al., 2012), as well as insoluble OM in meteorite samples (Danger et al., 2020). These studies provided insights into the molecular diversity and highlighted various heteroatomic families of molecules and/or (macro)molecule fragment ions in those samples.

Thus far, we lack complete laser desorption/ablation mass spectrometric data on sulfurized sedimentary OM. More specifically, we lack such analysis on the same rock in *in situ* conditions (that is, without separation of the mineral and soluble/insoluble organic components) with comparative analysis of the solvent-soluble bitumen and of thoroughly extracted macromolecular component, that is, kerogen. Such comparative analyses are important to assess the potential for *in situ* analysis in laboratory or beyond Earth. They are important to assess contaminants and migration from other sources, as kerogen is usually considered less prone to include such contaminants than bitumen (Vandenbroucke and Largeau, 2007). Kerogen compositional heterogeneities such as those seen by IR spectroscopy in microfossil assemblages (Lepot, 2021) may be investigated at the individual microfossil scale that can be targeted by LDI/L2MS.

Here, we analyzed sulfurized OM in carbonate deposits of the paleo-lagoon of Orbagnoux, French Jura, which dates from the Jurassic (Kimmeridgian, ca. 150 Ma) (Tribovillard et al., 1992). This deposit has been thoroughly characterized with microscopy techniques, IR and X-ray spectroscopy, NMR, GC-MS on extracts and pyro-/chemo-lysis products, and ToF-SIMS (Fadel et al., 2020; van Kaam-Peters et al., 1998; van Kaam-Peters and Sinninghe Damsté, 1997; Mongenot et al., 1999; Sarret et al., 2002; Tribovillard et al., 2000, 1992). These studies indicate a predominant contribution from oxygenic photosynthesizers (cyanobacteria) to the OM, along with signatures of unicellular algae (coccolithophorids), and anoxygenic photosynthetic bacteria thriving in euxinic (H_2S-rich) conditions. These make the Orbagnoux deposit a relevant counterpart to the prokaryote-dominated fossil ecosystems of the deeper Precambrian (4000–541 Ma) record (Javaux and Lepot, 2018; Lepot, 2020). The Orbagnoux OM is thermally immature (van Kaam-Peters and Sinninghe Damsté, 1997; Tribovillard et al., 1992), unlike most Precambrian deposits. Such sediments with immature to low-maturity OM may be preserved close to the surface of Mars thanks to its current lack of plate tectonics (McMahon et al., 2018). Applying a combination of high mass-resolution LDI/L2MS, ToF-SIMS, and Py-GC-MS to Orbagnoux sediments, we develop further a methodology to analyze organic (micro)fossils in ancient rocks and provide important reference data for future *in situ* astrobiology missions.

2. Geological context & sample

The “Calcaire en plaquettes” formation of the Kimmeridgian of Orbagnoux, French Southern Jura, comprises five calcareous facies: massive limestones, dark- and light-parallel laminae (Fig. 1) and dark- and light- undulated laminae (Tribovillard et al., 1992). Here, we studied two samples, named ORBA3 and DP, from the underground mine of the Société des Mines d’Orbagnoux (a hamlet close to Corbonod, latitude 45.991894°, longitude 5.791269). The sample ORBA3 comprises both the dark- and light-parallel laminae, whereas the sample DP comprises only dark-parallel laminae.

Light-parallel laminae comprise ~88 wt% $CaCO_3$, chiefly in the form of fossils of coccolithophorids and total organic carbon (TOC) averaging at ca. 3.6 wt%, whereas the dark-parallel laminae display TOC of ca. 4.5–12 wt% and 75–82 wt% $CaCO_3$ (Mongenot et al., 2000; Tribovillard et al., 2000). In the dark-parallel laminae facies, OM occurs as stacks of layers a few micrometers to several tens of micrometers in thickness interbedded with $CaCO_3$-rich laminae (Fadel et al., 2020; Mongenot et al., 2000). Initial observation of the amorphous structure of OM in dark-parallel laminae has been used to argue for an origin after cross-linking by sulfur of organic molecules from planktic algae, planktic photosynthetic bacteria, and/or microbial mats (van Kaam-Peters et al., 1998; Mongenot et al., 1999; Tribovillard et al., 2000, 1992). Observation of sulfurized biomarkers in modern stromatolite-forming microbial mats (Pagès et al., 2015) is consistent with a benthic mat contribution to the Orbagnoux OM.

Moreover, alveolar textures of amorphous OM in the dark-parallel layers may be inherited from microbial extracellular polysaccharides, and the observation of filamentous and spherical microfossils suggests that these OM layers may comprise bacteria-dominated microbial mats (Pacton et al., 2006). The dark-parallel laminae show ~ 0.54 wt% Fe (as FeS_2 remaining in the kerogen after demineralization) and 13-18 wt% organic sulfur (Mongenot et al., 2000). In this facies OM sulfurization has thus been enabled by the euxinic (H_2S-rich) conditions allowed by the low abundance of Fe-yielding siliciclastic input, which could only contribute to minor sulfur sequestration in pyrite (Mongenot et al., 2000). Both bitumen and kerogen in Orbagnoux are extensively sulfurized (van Kaam-Peters and Sinninghe Damsté, 1997; Mongenot et al., 1999). For the kerogen, this likely resulted largely in cross-linking of lipids by sulfur at the earliest diagenetic stages, thereby protecting OM from biodegradation.

The kerogen is highly immature as indicated by H/C atomic ratios of 1.3–1.45 and RockEval pyrolysis parameters (Mongenot et al., 2000; Tribovillard et al., 2000), and has thus not entered catagenesis. Fourier-transform infrared spectroscopy and solid-state ^{13}C nuclear magnetic resonance show the highly-aliphatic, low-aromatic character of the OM in the Orbagnoux deposit (Mongenot et al., 1999). The dominance of hopanoid over steroid biomarkers supports the hypothesis that the OM was primarily produced by cyanobacteria with minor algal contribution (van Kaam-Peters et al., 1998). Nevertheless, we note that anoxygenic photosynthesizers may also produce some hopanoids (Rashby et al., 2007). Indeed, the detection of isorenieratene derivatives in the bitumen indicates the presence of photosynthetic sulfur oxidizing bacteria (van Kaam-Peters and Sinninghe Damsté, 1997). Kerogen pyrolysis products also support a predominant contribution of cyanobacterial lipids, and a lesser contribution of algal (likely coccolithophorid-derived) lipids (Mongenot et al., 1999).

3. Methods

3.1. **Sample preparation**

The ORBA3 rock sample, from the same stratigraphic level as that studied in Fadel et al. (2020), was analyzed directly along fresh fractures of the dark organic-rich layers. Bitumen obtained after extraction of soluble molecules in dichloromethane (DCM) and methanol (Me), and the kerogen defined as the solid phase retained after extraction by these solvents and demineralization in HF and HCl, were also analyzed. Acid demineralization and solvent-based separation of bitumen (soluble OM) and kerogen (insoluble OM) have been commonly used for the study of terrestrial rocks and meteorites (e.g., Brocks et al., 2003; Vinogradoff et al., 2017). All mechanical materials, steel equipment and glassware needed for grinding and extracting our samples were rinsed with acetone, and HPLC-grade solvents (ethanol and DCM). The dark laminae of the rock were crushed into millimetric/coarse pieces between multiple sheets of aluminum foil (which was combusted at 400°C to remove contaminants). Some pluri-millimetric flat pieces of rock were selected for analysis of OM along the fresh fracture surfaces, after sticking using copper tape on a silicon wafer. The remaining pieces were powdered (89 g) in an agate mortar mill. The powder was extracted in a solvent-reflux (Soxhlet) apparatus for 48 hours where round-bottom flasks were filled with 200 ml DCM and glass-fiber thimbles filled with no more than 50 g of rock powder. Silicon wafers, used as sample-deposition substrates for laser desorption-ionization analyses, were also cleaned by Soxhlet extraction. After 48 hours of extraction, the organic soluble fraction (bitumen) was dissolved in DCM, which was evaporated using a Buchi Rotavapor (R-300) to obtain a dry bitumen fraction. The Soxhlet extraction yielded 1.6 g of bitumen (1.7% extraction yield). The powder after extraction of the bitumen weighed 87 g.

A quantity of 9.5 g of the Soxhlet-extracted powder of ORBA3 was further extracted with DCM/MeOH (2:1 by volume) by Soxhlet extractor prior to treatments with 38% hydrofluoric and 15% hydrochloric acid to remove silicates and carbonates. The residue was rinsed with distilled water to remove residual HF in the sample. Dried kerogen formed millimetric nuggets that were flattened (they deform, but do not break) in an agate mortar in DCM. The kerogen flakes were either attached to the sample holder using a double-sided copper tape, or deposited directly onto silicon wafers.

The DP sample was extracted in DCM after crushing. The extract was further fractionated on a silica column using a 9:1 cyclohexane:DCM mixture, yielding an apolar bitumen fraction. In order to further assess the fragmentation of a reference geoporphyrin biomarker in comparison with the Orbagnoux samples, vanadium etioporphyrin III oxide, in crystalline form (Alfa Aesar™) was dissolved in DCM and deposited on a silicon wafer for L2MS analysis.

3.2. **Laser desorption-ionization MS**

We used a custom-built high-resolution L2MS instrument (HR-L2MS, Fasmatech S&T). The samples, deposited onto silicon wafers were exposed under vacuum (10^{-6} to 10^{-5} mbar) to top-hat transverse profile beams of the 2^{nd} or 4^{th} harmonic of a Nd:YAG laser (Quantel Brilliant, λ= 532 nm or 266 nm, 4 ns pulse duration, 10 Hz repetition rate), focused to a diameter of 320 to 400 µm. The fluence of the laser was adjusted between 0.01 and 0.6 J/cm² (using a circular variable reflective neutral-density filter), in order to obtain significant ion signal with minimal molecular fragmentation. In LDI-MS configuration, charged species already ionized by the desorption/ablation beam are carried in the ion trap. In L2MS configuration, the ejected plume

of molecules/atoms from the solid sample is irradiated by an orthogonal beam generated by the 4th harmonic of a second Nd:YAG laser (Quantel Brilliant, λ= 266 nm, 4 ns pulses, 10 Hz) shaped into a rectangular sheet of 0.5 cm x 0.25 cm directed parallel to the sample surface at ca. 3.5 mm distance, and fired with a delay of 4 µs relative to the desorption laser pulses. Post-ionization laser fluences ranged between 0.05 and 0.14 J/cm² (Table S2).

Formed ions are extracted and carried orthogonally by a set of electrodes into a segmented multipolar radiofrequency- and DC-driven ion guide/trap. There, ion packets are submitted to pulsed He gas cooling and compressed radially, before being transferred into a RF hexapolar field and further into an orthogonal reflectron ToF MS. This configuration allows for mass resolutions up to 20,000 m/Δm in the studied mass range (here commonly >10,000). Several portions of the ion packet ("mass windows") are selected based on the time delay between ion injection and ion trap. The signals recorded for all selected mass windows are combined into a single mass spectrum. Additional details on the HR-L2MS instrumentation can be found in Slavicinska et al. (2022).

3.3. **ToF-SIMS**

The time-of-flight TOF.SIMS 5 instrument (ION-TOF GmbH) of the advanced characterization platform from Chevreul Institute (Lille University) was used to analyze the Orbagnoux bitumen deposited on a silicon wafer. The primary ion beam of Bi_3^+ was operated at 25 keV, 0.29 pA. Pulses of ions, within a focused beam of ~1 µm diameter at the sample surface, and a pulse length of 1 ns, were rastered over a sample surface of 500 µm x 500 µm. The signal collected on the time-of-flight detector was integrated over a spatial region of interest, yielding a spectrum with a mass resolution (m/Δm) of 3000 at m/z=55 for $C_4H_7^+$.

3.4. **Mass calibration and formula assignments**

For LDI-MS and L2MS, an initial external calibration using various calibrants (tocopherol, fullerene, naphthalene, or NIST 16 PAH mixture) was performed, which usually allowed tentative assignments of the peaks within <500 ppm deviation. Clusters of $C_nH_{0-3}^-$ ions detected at near-integer m/z values were systematically detected in negative polarity, allowing final internal calibration within ca. ±30 ppm (difference between measured and exact mass expressed in ppm as defined in Table S1). Clusters of $C_nH_{0-3}^+$ ions similarly helped intermediate calibration of the positive polarity mass spectra; although these were not always detected at low desorption fluence, increase in desorption fluence allowed their detection, which in turn provided external calibration for the lower-fluence mass spectra, also yielding ca. ±30 ppm accuracy.

Final internal calibration of the positive mass-spectra was performed using peaks that were uniquely attributed to chemical formulae thanks to lack of isobars within precision at low mass and/or isotope pattern distributions (usually provided by S isotopes, e.g. Fig. S1), yielding attributions within ca. ±20 ppm. For example, the spectrum of Fig. 2A was calibrated with peaks of C_3HS^+, $C_3H_3S^+$, $C_6H_7^+$, $C_4H_5S^+$, $C_4H_7S^+$, C_7H_7+, $C_6H_7O^+$, $C_6H_7S^+$, $C_7H_9S^+$, $C_8H_6S^+$, $C_{10}HS^+$, $C_{13}H_9^+$, $C_{14}H_{11}S^+$, $C_{15}H_9S^+$, $C_{24}H_9S^+$, $C_{27}H_7S^+$, which yielded deviations after assignment of the calibration peaks within -20 to +11 ppm (mean -0.15 ppm, standard deviation = 9 ppm, n=16). For ToF-SIMS, initial internal calibration was performed with C^+, CH_3^+, $C_2H_2^+$ (from fragmentation of the sample) and Cs^+ (contaminant) ion peak positions, also yielding initial deviations of < ±100 ppm, and final internal calibration was performed using main peaks assigned as described above, yielded deviations < ±30 ppm.

Formula assignment was performed in mMass (Strohalm et al., 2010) by constraining candidates within $C_{0–100}H_{0–300}S_{0–4}N_{0–4}O_{0–4}$ and deviations within 30 ppm (e.g., Table S1). Among proposed results, formulae with combinations of three or more heteroatoms (N, S, O) and high H/C such as $C_5H_8N_2O_2^+$, $C_{19}H_{18}NS_2^+$ (yielding exact masses similar to those, e.g., of low H/C hydrocarbons) have been ruled out, which is supported by their absence in LDI-FT-ICR-MS analyses of bitumen (Cho et al., 2012).

3.5. **Mass-defect plots**

Due to the high number of peaks selected with our low-signal threshold (filtering intensities >800, reaching to more than a thousand in some spectra (Fig. 2A), mass-defect plots (Sleno, 2012) were drawn to illustrate the diversity of ions detected and to highlight chemical families and infer their fragmentation patterns. Mass-defect plots show nominal masses (nearest integer value of the measured masses) against mass defects (equation 1) or against Kendrick mass defects (equation 2, Reemtsma, 2009). In these plots, the symbol radius was made proportional to the intensity of each peak relative to that of the most intense peak. In order to highlight alkylation series, we used a Kendrick mass-defect plot when necessary. "Conventional" mass defect plots (1) were better adapted for spectra dominated by low H fragments/clusters and inorganic species.

(1) Mass defect = measured mass – nominal mass

(2) Kendrick mass defect = (nominal mass of CH_2 / true mass of CH_2) * measured mass – nominal mass

3.6. **GC-MS**

The apolar extract of DP was analyzed with a Perkin Elmer 680 gas chromatograph equipped with an auto sampler and coupled with a Perkin Elmer 600C mass spectrometer at the PC2A laboratory. A 1 µL of fraction was injected in the GC with inlet at 250°C, a DB5-MS-UI column initiated at 50°C for 1 min and heated to 310°C at 4°C.min^{-1} and maintained 15 minutes at 310°C, using a helium flow of 1 mL.min^{-1} and the split-less mode. Mass scans were acquired from m/z 45 to 500 (0.2 s/scan, interscan delay 0.1 s), using an ionization energy of 70 eV.

The kerogen of ORBA3 was analyzed using pyrolysis gas chromatography-mass spectrometry (Py-GC-MS) at the UMET laboratory. The sample was pyrolyzed using a double shot at 300 °C and 600 °C for 0.5 min with a Frontier Lab Multi-shot Pyrolyzer (EGA/PY-3030D). The pyrolyzer is coupled to a Shimadzu GCMS-QP2010 SE system, with a SLB-5MS column. The sample was injected in split-less mode. The initial oven temperature was kept at 40°C for 2 minutes and then ramped to 300°C at a rate of 8°C/min and kept constant for 5 min. The solvent delay was set for 2 minutes. Ionization was performed with 70 eV electrons and a source at 230 °C. The interface temperature was 280 °C. The analysis was carried out in full scan mode over the mass range of 40–600 m/z.

4. Results and interpretations

4.1. **Bitumen**

4.1.1. Bitumen: LDI-MS at 266 nm

Analysis of the bitumen extract in LDI-MS using 266 nm desorption at a moderate fluence of 0.6 J/cm² produced a very-rich mass spectrum displaying more than 1380 peaks above the signal threshold of 800 in intensity (Fig. 2A). Some nominal mass intervals displayed a few peaks resolved thanks to a mean mass resolution (m/Δm) of ca. 12k (Fig. 2A, inset).

In the Kendrick mass defect plot (Fig. 2B), red symbols indicate $C_xH_yS^+$ ions where no C_xH_y interference was detected and for which ^{34}S isotope peak/shoulders were located at the m+2 nominal mass (e.g., Fig. S1). The $C_nH_{0-3}^+$ cluster ions may interfere with identification of such sulfur-bearing molecules. Indeed, at a given nominal mass, $C_xH_y^+$ and $C_{x-3}H_{y+4}S^+$ ions, where x>3, with a mass difference of 4.4 mDa, can only be separated with a mass resolution (m/ΔM) of ~40k at 134 u. However, the distinct $C_nH_{0-3}^+$ series that could be identified at higher fluences (not shown) and in 532 nm desorption experiments (next section) can be ruled out here by the absence of C_n^+ peaks together with S-isotope patterns.

Pink circles (Fig. 2B) are attributed to $C_xH_yS^+$ ions solely on the basis of their mass defect value, not on isotope pattern, as in most cases $[M+2H]^+$ ion peaks were too intense to allow discrimination of ^{34}S isotopes shoulders. Blue symbols are attributed to $C_xH_y^+$ (hydrocarbon) ions.

Bi-colored symbols (Fig. 2B) with blue and red/pink colors are interpreted as a coalescence of $C_xH_y^+$ and $C_iH_jS^+$ peaks, in which case the red color indicates a $C_iH_j{}^{34}S^+$ shoulder/peak at the m+2 nominal mass, and pink an attribution of $C_iH_jS^+$ solely on mass defect value. The coalescence of $C_xH_y^+$ and $C_iH_jS^+$ peaks is most prominent with intense peaks occurring between two "alkylation" lines while low-intensity peaks cluster on these lines (e.g., $C_4H_7(CH_2)_n^+$ and $C_{10}H_8(CH_2)_n^+$ horizontals in Fig. 2B). Ion coalescence is indeed know to be favored by high ion abundances (Kaufmann and Walker, 2018). We note that due to the interference of $C_xH_y^+$ and $C_iH_jS^+$ peaks, $C_xH_y^+$ ion peaks cannot be used reliably for precise internal calibration. The best peaks for such calibration are those with unique interpretation, that is, low mass-defect and $C_iH_jS^+$ peaks (in red), and low-mass $C_xH_y^+$ molecules.

Yellow and green circles in Fig. 2B indicate $C_xH_yN^+$ and $C_iH_jO^+$ ions, respectively. Grey circles represent peaks where assignment was not possible and ^{13}C-isotope peaks are shown with black circles.

Aromatic hydrocarbons are prominent in the mass spectrum. The $C_7H_7(CH_2)_n^+$ series, observed here up to $C_{11}H_{15}^+$, is characteristic of alkylbenzene fragmentation through cleavage and rearrangements (McLafferty and Tureek, 1993). Alkyl-PAHs, from $C_9H_7(CH_2)_n^+$ through–at least–$C_{13}H_9(CH_2)_n^+$ are detected and dominated by $C_{10}H_8(CH_2)_n^+$ (likely alkylnaphthalenes). Ions with Kendrick mass defects below the alkylbenzene line, including $C_5H_9^+$ (highest H/C detected), $C_5H_7(CH_2)_n^+$ (up to $C_9H_{15}^+$), and $C_5H_5(CH_2)_n^+$ (up to $C_{10}H_{15}^+$) correspond to more saturated, likely cyclic compounds and/or their fragments.

The ions with high Kendrick mass-defects **(**Fig. 2B, and thus low mass-defect in Fig. S3A) are attributed to sulfur-bearing compounds. Among those, $C_5H_5S(CH_2)_{0-5}^+$ are typical fragments of alkylthiophenes ($C_4H_3S+nCH_2$) as observed in electron ionization MS (McLafferty and Tureek, 1993; NIST Mass Spectrometry Data Center, 2022), although some of these may represent

protonated benzene-thio(l)s such as $[C_7H_8S+H]^+$ (methylthiobenzene). Higher H/C sulfurated ions such as $C_8H_{13}S^+$ may represent protonated alkylthiophenes. Even higher H/C sulfurized ions along the $C_4H_7S(CH_2)_n{}^+$ series (with n of up to 3 or more) point to more saturated cyclic molecules such as thiacycloalkanes (McLafferty and Tureek, 1993). Aromatic sulfides include $C_8H_6S^+$ (benzothiophene), $C_9H_7S(CH_2)_{0\text{-}4}{}^+$ - likely alkylbenzothiophenes, $C_{14}H_{11}S^+$ (phenobenzothiophenium ion), as well as possible aromatic sulfur-bearing molecules with branched/cyclic alkyl side-chains such as $C_{10}H_{13}S^+$. In addition, weak signal of C_nHS^+ cluster ions is detected, indicating extensive fragmentation of some sulfur-bearing molecules.

The two main oxygenated species $C_6H_7O^+$ and $C_{10}H_9O^+$ likely represent protonated versions of aromatic alcohols such as phenol (C_6H_6O) and naphthalenol ($C_{10}H_8O$), respectively. The $C_3H_6O_2{}^+$ ion may represent a carbonyl/carboxyl group associated with alkyl chain fragment, e.g., from fragmentation of fatty acids. Nitrogen-bearing molecules are evidenced with the $C_6H_7N^+$ ions that likely represent aromatics such as aniline and/or picoline.

4.1.2. Bitumen: L2MS and LDI-MS at 532 nm desorption

Using 532 nm radiation for desorption, the ion signal was much weaker than that obtained for LDI-MS using 266 nm desorption (Fig. S3). Here the lower signal intensity prevented reliable distinction of low-H clusters/fragments $C_xH_y{}^+$ and $C_{x\text{-}3}H_{y+4}S^+$ molecules in the high mass-defect peaks using ^{34}S isotope peaks/shoulders.

In L2MS at the lowest desorption fluence, only a few low mass-defect peaks with the highest signal were clearly identified as S-bearing ions, also suggestive of fragmented alkylthiophenes (Fig. 3). Mass-defect plots highlight that non-aromatic ions are prominent in the signal in the domain where H/C>1 (Fig. 3 and S2b, $C_5H_7{}^+$ at m/z<100, and $C_8H_{13}{}^+$ at m/z>100), which are distinct from the dominant ions in the same region in LDI-MS at 266 nm (Fig. 2B: $C_6H_7{}^+$, $C_6H_9{}^+$ and $C_7H_7{}^+$ at m/z<100, $C_{10}H_{13}{}^+$ at m/z>100, with the latter two likely from alkylbenzenes). The dominant (poly)aromatics detected with 532 nm-desorption L2MS also generally display a smaller mass than those seen with 266 nm-LDI-MS.

In comparison with L2MS, at 532 nm-desorption, LDI-MS displayed decreased hydrocarbon signal (with exception of that attributed to $C_9H_7{}^+$, the base peak similar to L2MS), a relative increase in signal of low-H (fragmented?) sulfurated species such as $C_7H_7S^+$ and $C_8H_4S^+$, and generated C_nHS^+ as well as $C_nH_{0\text{-}3}{}^+$ clusters that were not seen in L2MS (Fig. 3, empty green symbols versus blue symbols). An increase in low H/C sulfur-bearing ions (e.g., $C_8H_4S^+$) is observed in LDI-MS relative to L2MS using the same desorption fluence.

An increase in desorption fluence in L2MS generated abundant $C_nH_{0\text{-}3}{}^+$ and C_nHS^+ cluster ions and a strong decrease in the hydrocarbon and sulfurated molecules detection (Fig. 3 and S3). The negative polarity LDI-MS spectrum recorded at the same desorption fluence essentially displayed $C_nH_{0\text{-}3}{}^-$ and C_nHS^- clusters (Fig. 4A). This indicates intensive fragmentation by the desorption laser at 0.24 J/cm².

Altogether, using desorption at 532 nm, the detection of hydrocarbons and sulfurated molecules was best achieved using L2MS (with 266 nm ionization laser). This contrasts with the 266 nm LDI-MS experiment where hydrocarbons and sulfurated molecules were already well represented without addition of a second ionization laser. Fragmentation was observed using 532 nm desorption even at moderate fluences, whereas higher fluences could be used at 266 nm desorption without significant generation of $C_nH_{0\text{-}3}{}^+$ and C_nHS^+ clusters (Fig. 2).

The VO^+, VO_2^+ and HVO^+ ions could be detected using desorption at 532 nm in LDI-MS and in L2MS (Fig. 3). A faint VO^+ peak was also detected in LDI-MS using 266 nm desorption (not shown). The geoporphyrin class of molecules is the most likely contributor of VO^+, HVO^+, and VO_2^+ (McKenna et al., 2021; Munoz et al., 2019). Indeed, L2MS of vanadium-etioporphyrin (Fig. S4) also produced VO^+. However, our analysis of the Orbagnoux bitumen did not detect the much stronger signal (than that of VO^+) of organic fragments at m/z > 400 (Fig. S4) that are typical of weakly-fragmented porphyrins (Cho et al., 2014; Dale et al., 1996; Pomerantz et al., 2009). Additional inorganic species detected in the bitumen with L2MS include $CaOH^+$, As^+, AsH^+, and Fe^+ (Fig. 3).

4.1.3. Bitumen: ToF-SIMS

The ORBA3 bitumen was further analyzed using ToF-SIMS (Fig. 5). Compared to LDI-MS and L2MS, the positive polarity ToF-SIMS spectrum shows a shift in peak intensities toward lower mass range indicating high fragmentation. The mass spectrum is dominated by fragments with H/C >1, with the most intense peaks being $C_3H_5^+$ and $C_4H_7^+$. PAHs are also detected (Fig. 5), as well as larger ions with higher mass defects and H/C>1, which could correspond to alkylbenzene fragments. This observation is consistent with the ToF-SIMS mass spectrum recorded on organic laminae in polished semi-thin sections of the same Orbagnoux sample (Fadel et al., 2020). Sulfur-bearing ions are also detected and are dominated by the CHS^+ fragment, and ions derived from molecules and/or fragments of alkylthiophenes and alkylbenzothiophenes. Inorganic ions included Ni^+, VO^+, as well as Mn^+, Fe^+, Cr^+, K^+ and Na^+ are also detected.

4.1.4. DP bitumen in GC-MS

Integration of the total GC-MS mass spectrum obtained on the DP bitumen (Fig. 6A) coupled to analysis of selected ion mass chromatograms (Fig. 6B-C and Fig. S5) provides clues to interpret the molecules and their fragments detected in laser desorption-ionization of Orbagnoux bitumen extracts. The most prominent ion at m/z 57 and 55 are mostly fragments of alkanes and alkenes (Fig. S5); these fragments are only faintly detected in L2MS (Fig. 3). The intense GC-MS signals at m/z 111, 125 and 139 are dominated by *n*-alkyl-thiophenes (Fig. 6B), *n*-alkyl-ethylthiophenes + isoprenoid alkylthiophenes, and *n*-alkyl-propylthiophenes (Fig. S5), respectively. These three main alkyl-thiophenes fragments detected in GC-MS are thus consistent with the three most intense ions seen on the alkyl-thiophene line in LDI-MS (Fig. 2). The GC-MS signal at m/z 161 is dominated by *n*-alkyl-methylbenzothiophenes (Fig. S5). Its abundance in the total ion count is consistent with the high signal of this fragment ($C_{10}H_9S^+$) detected in LDI-MS (Fig. 2). Similarly, the abundance of the $C_9H_7S^+$ ion in LDI-MS correlates well with the GC-MS peak at m/z 147 (Fig. 6A), which is another major fragment of alkylbenzothiophenes (Sinninghe Damsté and de Leeuw, 1990).

The mass chromatograms at m/z 105 shows peaks of low relative intensity, indicating the weak contribution of alkyl-methylbenzenes (Fig. 6C). The highest peak intensity of the mass chromatogram at m/z 91 only displayed an abundance of 0.76 % (relative to TIC), indicating the low abundance of alkylbenzenes. In contrast, aryl-isoprenoids and benzohopanes (Fig. 6C) contributed more significantly to the TIC, making these aromatic molecules likely sources for alkylbenzene fragments and possibly higher H/C fragments detected in LDI-MS (Fig. 2**)**. We could not identify PAHs, possibly due to co-elutions and/or low abundances.

4.2. **Kerogen**

4.2.1. Kerogen: LDI-MS & L2MS using 266 nm desorption

The kerogen yielded a mass spectrum in L2MS and LDI-MS using 266 nm desorption that is much less intense than that recorded on the bitumen (Fig. S3). Increasing the desorption fluence to 0.42 J/cm² (not shown), that is, closer to the fluence used on the bitumen LDI-MS of Fig. 2A, did not increase significantly the signal of the main organic ions detected and only increased the generation of carbon clusters (in particular C_{10}^+ and C_{15}^+) and of inorganic ions.

Due to the relatively low signal intensity, ^{34}S-isotopologues could only be investigated for a few high-intensity peaks, and only seven sulfurated species were clearly identified using ^{34}S-isotope (m+2) shoulders. These include benzothiophene ($C_8H_6S^+$), C_3HS^+ (fragments or clusters), $C_7H_7S^+$ and $C_8H_7S^+$ that might represent alkylthiophene fragments or e.g., aromatic molecules with sulfurated alkyl chains, and $C_9H_7S^+$ that likely comes from a heterocyclic compound (e.g., thiochromenium ion). The main S species identified from the kerogen are generally consistent with those detected in the bitumen, although a smaller number could be clearly identified in the former.

Additional major peaks lie along the catacondensed or pericondensed PAH composition lines (noted a-g in Fig. 7), or shifted by the mass of one hydrogen below these lines. Accordingly, (a) can be attributed to $C_9H_7^+$ (indene–H fragment or isomer), (b) to $C_{10}H_8^+$ (naphthalene), (c) to $C_{11}H_9^+$, (d) $C_{12}H_8^+$, (e) $C_{13}H_9^+$ (fluorene–H or isomer), (f) $C_{15}H_9^+$, (g) $C_{16}H_{10}^+$ (pyrene or isomer). These PAH species are consistent with those detected in the bitumen (Fig. 2B). The hydrocarbons with H/C>1 are poorly represented for low-mass ions (<100 u.) in the kerogen, in sharp contrast with analyses on the bitumen (Fig. S2). However, the intensity of the ion signal at m/z over 175 is notably higher for the kerogen than for the bitumen (Fig. 7 and S2). This higher-mass signal likely includes PAHs (Fig. 7 and between the PAH* and PAH§ lines in Fig. S2C), alkylated PAHs (some with H/C >1), and sulfurated molecules (lying well below the PAH§ line).

A number of peaks have been attributed to nitrogenated species (Fig. 7), including: α ($C_8H_{10}N^+$), β ($C_9H_9N^+$), χ ($C_{10}H_{10}N^+$), ε ($C_{11}H_9N^+$), ϕ ($C_{12}H_9N^+$), γ ($C_{15}H_{10}N^+$), and η ($C_{11}H_8N^+$). With their low H/C ratio, these species likely include heterocyclic molecules with functional groups such as pyrrole, indole, quinoline, and/or pyridine. These were not detected in the bitumen, which only showed $C_6H_7N^+$ (Fig. 2B). In addition, two main oxygenated ions are detected in the kerogen: $C_6H_7O^+$ ([phenol+H]$^+$) and $C_{10}H_9O^+$ (e.g., [naphthalenol+H]$^+$), consistent with those detected in the bitumen.

Finally, the negative polarity LDI-MS spectrum from the kerogen is dominated by $C_nH_{0\text{-}3}^-$ and C_nHS^- cluster ions (Fig. 4B), similar to that of the bitumen, but also displayed $C_2S_2^-$ and likely $C_6S_2^-$.

4.2.2. Kerogen: pyrolysis GC-MS

During the 300°C pyrolysis step (Fig. S6), only a few faint peaks are detected between 2 and 30 minutes retention time, which include bisphenol A and other phenolic compounds and ketones, which likely represent contaminants from an unidentified plastic source, possibly the polypropylene bottles used for HF maceration or the Py-GCMS apparatus. We also infer that high-retention time peaks observed after 30 mins are likely such contaminants.

The main molecules detected during the 600°C pyrolysis step are shown in Fig. 8A, and include aromatic hydrocarbons (and alkylated aromatics), thiophene and alkylthiophenes, (alkyl)benzothiophenes, and phenols (again dominated by bisphenol A). Aside from the phenols, none of these species are detected under pyrolysis at 300°C. The boiling temperature of methylthiophene is 116°C, that of toluene 111°C, naphthalene 217°C, benzothiophene 221°C (Brown and Stein, 2022), whereas that of bisphenol A is 360°C (National Center for Biotechnology Information, 2022). This indicates that the main species detected during pyrolysis at 600°C (but not at 300°C) are indigenous to the Orbagnoux kerogen. Moreover, the observation that they did not evaporate at 300°C argues that they were not merely adsorbed onto the kerogen, but rather derive from the fragmentation of its macromolecular structure.

The peak at m/z 91 dominates the total GC-MS spectrum (Fig. 8B). Its mass chromatogram (Fig. S7) shows that it is dominated by alkylated aromatic hydrocarbons, alkylbenzothiophenes, with a contribution of alkylphenols (including those from bisphenol A) – it is thus dominated by the fragment C_7H_7. This fragment is only weakly detected in the laser-desorption-ionization mass spectra recorded on the kerogen (Fig. 7) whereas it was prominent in the bitumen (Fig. 2).

Also prominent in the total GC-MS spectrum, the signal at m/z 97 (Fig. S8) is dominated by contributions of alkylthiophenes (thus by the fragment C_5H_5S) and that at m/z 111 by the contributions of alkyl-methylthiophenes (thus by the fragment C_6H_7S). Fragments are detected at these masses in laser-desorption MS of the kerogen but were only tentatively assigned to these sulfurized fragments due to low isotopologue signal (Fig. 7).

The total GC-MS peak at m/z 147 is dominated by the contributions of alkylbenzothiophenes (Fig. S9), thus by the $C_9H_7S^+$ fragment. This molecule/fragment is also abundant in the laser-desorption mass spectra of the bitumen and of the kerogen (Fig. 2A, Fig. 7). The benzothiophene molecule, abundant in the pyrolysis GC-MS of the kerogen (Fig. 8A) is also represented by the dominant S-bearing ion $C_8H_6S^+$ in laser desorption mass spectra of kerogen and bitumen (Fig. 2B, Fig. 7).

The total GC-MS peak at m/z 55 is dominated by the contribution of alkenes, and thus by the fragment by C_4H_7, and is more intense than that at m/z 57, which is dominated by alkanes (thus by C_4H_9 fragments), c.f. Fig. S10. These fragments were relatively faint in laser-desorption ionization of the kerogen and the bitumen (Fig. 2A, Fig. 7A) but prominent in ToF-SIMS (Fig. 5).

The total GC-MS peak at m/z 115 is dominated by indene, methylindene, benzothiophenes, phenylthiophene, and bisphenol (Fig. S11), thus it is essentially represented by C_9H_7 molecules/fragments. These are also intense in the laser-desorption mass spectra recorded on the bitumen and on the kerogen (Fig. 2A, Fig. 7A). The ions generated at m/z 128 in Py-GC-MS are dominated by those of naphthalene ($C_{10}H_8$, Fig. S12) which also comprise a major contribution in laser-desorption ionization mass spectra of kerogen and bitumen.

Altogether, Py-GC-MS at 600°C is consistent with the composition of the Orbagnoux kerogen inferred from LDI-MS and L2MS. However, we note that relative to Py-GC-MS alkyl-chain fragments are under-represented in laser-desorption experiment of the kerogen compared to fragments bearing thiophene or aromatic groups, and that polycyclic aromatic hydrocarbons appear more prominent in laser-desorption experiments, in particular for those larger than phenanthrene, which are not evidenced in GC-MS.

4.3. **Rock**

Analysis of the freshly-fractured piece of rock with L2MS using 532 nm desorption required a desorption fluence of ca. 0.2 J/cm² to generate significant signal (Fig. 9). At this desorption fluence, similarities can be noticed with the L2MS spectrum recorded on the extracted bitumen with a similar setup (Fig. 9 vs. Fig. 3). These similarities include the prominence of $C_nH_{0-3}^+$ cluster ions, with the same dominance of C_{11}^+, although the rock was dominated by C_n^+ clusters whereas the bitumen displayed a stronger signal of $C_nH_2^+$. Aromatic hydrocarbons are dominated by $C_7H_7^+$, $C_9H_7^+$, $C_{10}H_8^+$, $C_{11}H_9^+$, and H/C>1 hydrocarbons are detected with the highest H/C observed for $C_9H_{15}^+$. This pattern is consistent with that observed in L2MS of the bitumen recorded at a similar fluence (Fig. 3, in red).

The main oxygenated species (Fig. 9, $C_6H_7O^+$, and $C_{10}H_9O^+$) are similar to those that dominate in the analyses of the bitumen and the kerogen using 532 nm or 266 nm desorption (Fig. 2, Fig. 3, Fig. 7). This strongly supports that the O-species detected in the bitumen and the kerogen with laser-desorption mass spectrometry are not from laboratory contaminants, unlike the bisphenol-A and some related molecules/fragments detected with Py-GC-MS.

Nitrogenated species with H/C of ~1 are detected from the rock, consistent with those detected in the kerogen (α, β, χ, ϕ in Fig. 7 and Fig. 9).

A number of near-zero to negative mass-defect ions, not detected in the extracted organic phases, have been tentatively attributed to CaS_n^+ and $Ca_xO_yH_z^+$ (Fig. 9), although other assignments may be possible for some.

In this context of low ion intensity, overlap of $C_nH_{0-3}^+$ clusters, and the additional presence of inorganic ions, sulfurized organic molecules could not be as clearly evidenced as in extracted bitumen and/or kerogen. Nevertheless, they appear as C_nHS^+ fragments, with an important contribution of C_7HS^+ and C_9HS^+ similar to that observed in the bitumen using the same desorption wavelength (Fig. 3). Moreover, the negative polarity spectrum is dominated by C_n^- and C_nHS^- fragments (Fig. 4C), again similar to that recorded on the bitumen.

5. Discussion

5.1. **Hydrocarbons**

PAHs are abundantly detected in the Orbagnoux OM with L2MS and LDI-MS, consistent with previous L2MS detection of PAHs with three or more rings made on other rocks rich in immature OM (Zhan et al., 1997). PAHs were also detected with L2MS in mature to high-maturity OM (Mahajan et al., 2001). Interestingly, in the latter study the lower abundance of alkyl-PAHs relative to parent PAHs in the kerogen compared to the unextracted rocks has been proposed as an effect of laser pyrolysis associated with the breakdown of the kerogen macromolecule (Mahajan et al., 2001). However, here we do not see a clear increase in parent PAHs over alkyl-PAHs in the kerogen relative to the bitumen (see peaks between PAH* and H/C=1 lines in Fig. 7 *versus* alkylation series in Fig. 2B). The detection of PAHs using ToF-SIMS further supports that detected PAHs are not produced from other types of molecules by laser pyrolysis in the bitumen. PAHs are only weakly detected in pyrolysis GC-MS of the kerogen at 600°C, consistent with the low thermal maturity of the Orbagnoux OM. Thus the origin of these PAHs could be from early diagenetic transformation of some polycyclic highly-saturated molecules (Tan et al., 1996; Wakeham et al., 1980) or from ancient biomass burning (Masclet et al., 1995).

PAHs and alkyl-PAHs series with up to five rings can be found in bitumen of thermally immature to mature rocks (Copelin and Larter, 1983). Di- to tetra-aromatic derivatives of benzohopanes can also be found in immature OM deposits (Rybicki et al., 2017), and though we could not identify them in the DP bitumen with GC-MS, their fragments may have contributed to the PAH signal detected in LDI-MS and L2MS. Interestingly, some rocks with a thermal maturity in the late stage of oil generation display PAHs with four or more rings as important products of the catalytic hydropyrolysis of the kerogen, whereas these could not be detected in the bitumen (Brocks et al., 2003). This is consistent with our LDI-MS and L2MS results displaying the dominance of relatively small (alkyl)-PAHs in the bitumen and the relatively higher signal at m/z above 175 detected in kerogen, which is likely dominated by (alkyl)-PAHs. Nevertheless, small aromatics ($\leq$ 14 carbons) strongly dominate the mass spectra of bitumen and whole rock, and to a lesser extent of the kerogen. Interestingly, this contrasts with the studies of bulk and soluble meteoritic OM with L2MS (Clemett et al., 1998; Elsila et al., 2005; Hahn et al., 1988; Sabbah et al., 2022, 2019, 2010; Zenobi et al., 1992, 1989), in particular with the same HR-L2MS setup as that used herein (Slavicinska et al., 2022; 532 nm desorption and 266 nm ionization), where larger PAHs dominate the spectra. We note that larger PAHs are also expected in highly-mature terrestrial carbonaceous matter as observed with L2MS (Mahajan et al., 2001) and consistent with pyrolysis GC-MS studies (Brocks et al., 2003; Marshall et al., 2007).

The prominent signal of PAHs and alkyl PAHs in the bitumen and extracted kerogen can be explained by the use of 266 nm photons, which can promote these molecules to resonant energy levels, thus permitting their subsequent ionization by a second photon of the same wavelength (REMPI, Boesl and Zimmermann, 2021; Clemett and Zare, 1996). PAHs and alkyl-PAHs are thus readily ionized with two 266 nm photons (Desgroux et al., 2013; Lias et al., 2022). The ionization fluences used here in L2MS are within optimal values that maximize ionization of PAHs with minimal fragmentation (Thomson et al., 2007). The desorption fluences used are also within optimal values for L2MS of "free" PAHs (Mihesan et al., 2008). Nevertheless, we note that variations in REMPI efficiencies occur among various PAHs, depending on the shape of their absorption spectrum in the UV domain as well as the lifetime of their excited singlet state (Haefliger and Zenobi, 1998). This may explain the lower detection of anthracene (e.g., Kipfer et al., 2022) relative to other PAHs or to its isomer phenanthrene (Faccinetto et al., 2011; Haefliger and Zenobi, 1998). However, differences in size distributions of PAHs have been evidenced for combustion products with L2MS (Ngo et al., 2020). This supports that the distinct PAH patterns observed between the Orbagnoux OM and, e.g., meteorites (discussed above), is not only an effect of distinct analytical parameters (e.g., wavelength and/or fluence of desorption and/or post-ionization).

In contrast with PAHs, alkenes and alkanes would require the energy of at least two such photons to reach their lowest molecular absorption energy level (Boesl and Zimmermann, 2021), and that of an additional photon to cross their ionization threshold (Desgroux et al., 2013; Lias et al., 2022). Nevertheless, high H/C fragments are detected with LDI-MS and/or L2MS such as $C_4H_9^+$ in the kerogen and bitumen, and more in the bitumen only such as $C_8H_{13}^+$ and $C_9H_{15}^+$ (Fig. 2, Fig. 3, and Fig. 7). The latter two may have formed by protonation of cyclic highly-saturated molecules with two double bonds, such as 4-ethenyl-cyclohexene (C_8H_{12}) and 1-(2-propenyl)-cyclohexene (C_9H_{15}). The latter have ionization energies of 8.93 eV and 8.49 eV, respectively (Lias et al., 2022), also within reach of two-photon ionization at 266 nm. The ion $C_4H_9^+$ results from fragmentation of alkanes. The fragments of alkanes and alkenes, although weakly detected with LDI/L2MS, are consistent with the highly-aliphatic nature (Fig. 6, Fig. S5) of the Orbagnoux type-1 microbial OM (van Kaam-Peters and Sinninghe Damsté, 1997; Mongenot et al., 1999; Tribovillard et al., 1992). The small alkene and alkane fragments

$C_3H_5^+$, $C_4H_7^+$ and $C_4H_9^+$ are dominant in the ToF-SIMS of the bitumen (Fig. 5), thus reflecting the high aliphaticity of the sample.

5.2. **Sulfurated molecules**

Ions with formulae consistent with thiophenes, alkylthiophenes and alkyl-methylthiophenes fragments, as well as benzothiophene and fragments of alkylbenzothiophenes are well represented in LDI-MS and L2MS spectra of the kerogen and bitumen, consistent with the prominence of such molecules seen in GC-MS. Thiophene has an aromatic structure with π−electron delocalization over the whole ring structure (Kumar and Das, 2012). The ionization energy of thiophene is 8.86 eV, that of methylthiophene ~8.6 eV; that of dimethylthiophene ~8.2 eV, that of ethyl-thiophene ~8.7 eV, that of 2-butyl-thiophene 8.5 eV, and that of benzothiophene 8.17 eV (Lias et al., 2022). All these are well within reach of ionization by two 266 nm photons. These sulfurated molecules are also well detected with 532 nm LDI-MS, hence suggesting ionization with four photons is possible with the fluences used. However, increased fragmentation is observed with 532 nm LDI-MS, as indicated by the predominance of C_nHS^+ cluster ions and low H/C ions such as $C_8H_4S^+$, whereas these ions were absent or faint in the L2MS and LDI-MS using 266 nm for either second-step ionization or for LDI.

The main fragments of alkylthiophenes, alkyl-methylthiophenes, and alkylbenzothiophenes are also prominent in ToF-SIMS of the bitumen, along with the CHS^+ cluster/fragment, which also supports that the thiophenic moieties detected in LDI-MS and L2MS are not laser-pyrolysis byproducts but rather fragments of indigenous molecules. Indeed, the detection of thiophenic moieties in L2MS and LDI-MS of kerogen and bitumen is consistent with their detection in extracts with GC-MS and in kerogen *via* Py-GC-MS (as reported here and in van Kaam-Peters et al., 1998; van Kaam-Peters and Sinninghe Damsté, 1997; Mongenot et al., 1999) and with X-ray absorption spectroscopy of kerogen (Sarret et al., 2002). Interestingly, signatures of benzothiophenes such as $C_8H_6S^+$ and $C_9H_7S^+$ are weak in ToF-SIMS, suggesting that their detection in LDI-MS and L2MS may be favored by a (REMPI?) ionization scheme linked with their polycyclic aromatic structure associating the thiophene with a phenyl group.

Furthermore, LDI-MS and/or L2MS of the Orbagnoux OM revealed C_nHS^+ and C_nHS^- clusters, as well as $C_2S_2^-$. We suggest that these derive preferentially from the fragmentation of (alkyl)-sulfides (R-S-R) and (alkyl)-disulfides (R-S-S-R) groups that represent ca. 25% and ca. 12%, respectively of the S species in the kerogen of dark-parallel laminae (Sarret et al., 2002). Pyrolysis experiments show that alkyl-(di)-sulfides are the S moieties most prone to cracking at 400°C, leaving kerogen residues dominated by thiophenes (Sarret et al., 2002).

We note that thiophenes, alkylthiophenes, benzothiophenes and alkylbenzothiophenes have been detected in meteoritic insoluble OM with GC-MS through pyrolysis and catalytic hydropyrolysis (Remusat et al., 2005; Sephton and Gilmour, 2005). Low-temperature desorption/pyrolysis GC-MS yielded alkylthiophenes from the Murchison meteorite (Levy et al., 1973). Benzothiophenes were detected in minor amounts with L2MS in meteorites (Slavicinska et al., 2022). Several sulfur-bearing molecule classes are thus detected in meteorites as well as in sedimentary OM.

5.3. **Nitrogenated molecules**

Low H/C molecules with one N suggestive of heterocyclic molecules such as pyrroles, indoles, quinolines, and/or pyridines are detected with LDI-MS and L2MS in the Orbagnoux kerogen, and with L2MS in the rock. Heterocyclic N-molecules are consistent with pyrolysis products of recent biomass and with what is detected in petroleum and in rocks of OM maturity similar

to that of Orbagnoux (Bennett et al., 2004; Knicker et al., 1996). Their detection is broadly consistent with that of such families of molecules using LDI-MS (355 nm desorption) in crude oils (Cho et al., 2012) and in the insoluble OM of meteorites (Danger et al., 2020). Indeed, a low ionization energy is required to ionize N-bearing heterocyclic molecules (Cho et al., 2012), e.g., 7.5 eV for carbazole ($C_{12}H_9N$, Lias et al., 2022), putting many of these N-bearing heterocyclic molecules within the reach of two-photon ionization at 266 nm. However, in stark contrast with the 355 nm LDI-MS study of crude oils by Cho et al. (2012), these highly unsaturated nitrogenated hydrocarbons were not detected in the Orbagnoux bitumen, which only showed $C_6H_7N^+$ using 266 nm LDI-MS. This might be explained by an overwhelmingly high sensitivity to aromatic hydrocarbons (including PAHs) and sulfurated hydrocarbons due to REMPI at 266 nm, relative to the ionization scheme of nitrogenated species. Cho et al. (2012) noted that 355 nm LDI-MS appeared more sensitive to N- relative to S-bearing positive ions. However, these authors studied bitumen which are relatively poor in organic S (0.11–2.1%) whereas the Orbagnoux kerogen in the dark-parallel laminae reaches 0.07–0.1 atomic S/C ratios (Mongenot et al., 2000). In ToF-SIMS of the Orbagnoux bitumen, hydrocarbons and sulfurated hydrocarbons also strongly dominated the positive ion signal. It is possible that the Orbagnoux kerogen may be enriched in N-moieties relative to the bitumen. The detection of sulfurated hydrocarbons and PAHs in the kerogen requires fragmentation of the macromolecular structure, which may favor the concomitant fragmentation and ionization of N-species.

5.4. **Oxygenated molecules**

Two main oxygenated ions $C_6H_7O^+$ ([phenol+H]$^+$) and $C_{10}H_9O^+$ (e.g., [naphthalenol+H]$^+$) were detected in the bitumen, kerogen and fresh rock, together with minor other O-bearing fragments in the bitumen, and possibly (though not assigned with certainty) in the kerogen. Phenol and naphtalenol have ionization energies of 8.49 and 8.6 eV, respectively (Lias et al., 2022) and intense absorption features/bands around 270 nm (Talrose et al., 2021), allowing a resonant two-photon ionization scheme at 266 nm. The low abundance of oxygenated hydrocarbons is consistent with their lower signal (relative to hydrocarbons) in positive LDI-MS recorded at 355 nm on crude oils (Cho et al., 2012). Oxygenated ions are also scarce and limited to low-mass fragments ion ToF-SIMS of the bitumen (Fig. 5) and of the rock (Fadel et al., 2020). This scarcity of O-species in positive ion ToF-SIMS and LDI/L2MS is altogether consistent with low oxygen concentration in the bulk of the Orbagnoux OM, characteristic of a type-I microbial origin (Tribovillard et al., 1992).

5.5. **Carbonaceous cluster formation**

Detection of $C_nH_{0\text{-}3}^+$, C_nHS^+ cluster ions appear to be linked with variation in wavelength and fluences of the desorption laser. In particular, for the bitumen the 532 nm desorption wavelength appears more prone to generate these clusters in positive polarity mass spectra than that at 266 nm. Fragmentation of PAHs down to C^+ ions and including production of $C_nH_{0\text{-}3}^+$ clusters has already been observed with L2MS using 532 nm desorption (Faccinetto et al., 2008; Mihesan et al., 2008) at fluences comparable to those stimulating the formation of $C_nH_{0\text{-}3}^+$ cluster ions herein (Fig. 3). Carbon clusters are indeed known to form by laser irradiation of graphite, in soot-producing flames, and by photolysis or pyrolysis of small hydrocarbons (Van Orden and Saykally, 1998).

Increased signal of $C_nH_{0\text{-}3}^+$ and of fullerenes was observed with fluences as low as 0.04 J/cm² using 355 nm LDI-MS on insoluble meteoritic OM (Danger et al., 2020). The observation that the intensity and distribution of C_{42} to C_{100} fullerenes remained stable with increases in fluence of 1064 nm desorption on a meteorite suggests that fullerenes are indigenous (Sabbah et al.,

2022). In contrast, the same study showed that increasing desorption fluence on pyrolytic graphite produced increases in small (m/z <400) $C_nH_{0-3}^+$ clusters, thus arguing for their laser-induced formation. Here we detected no fullerenes with L2MS or LDI-MS of the Orbagnoux OM, even at the highest fluences used (up to 1.5 J/cm² in L2MS using 266 nm desorption, not shown). Only small clusters formed in positive polarity with increasing desorption fluence in the Orbagnoux OM, in particular using 532 nm desorption for the bitumen (Fig. 3).

These small clusters (in particular C_{10}^+ to C_{18}^+) appeared even more predominant during analysis of the fresh rock (Fig. 9) than on the bitumen (Fig. 3) or the kerogen (not shown). We suggest that this might be the result of a matrix effect possibly linked with inorganic species increasing fragmentation of organic molecules in the desorption plume, or favoring the ionization of carbon-rich clusters over higher H/C hydrocarbons such as PAHs. As discussed above, while the wavelengths used allow ionization of aromatics with minimal fragmentation, aliphatic molecules (or side-chains, or bridges in the macromolecular OM) may be less efficiently ionized, and in turn more readily fragmented (Boesl and Zimmermann, 2021). As bitumen are enriched in free aliphatic molecules (relative to extracted kerogen), they are more prone to generate carbon clusters and other heteroatomic clusters by fragmentation in the desorption/ionization conditions used here (as well as in SIMS).

Negative polarity mass spectra of the Orbagnoux OM chiefly comprise clusters of $C_nH_{0-3}^-$, C_nHS^-, and $C_nS_2^-$ (Fig. 4). On the rock, the negative polarity mass spectrum only comprises such carbonaceous clusters (Fig. 4C), in contrast with the positive polarity MS, which is crowded with inorganic ions (Fig. 9). The predominance of such clusters in negative ion spectra is also typical of ToF-SIMS analyses of fossil OM as well as polymers (Fadel et al., 2020; Lindgren et al., 2012).

5.6. **Geoporphyrins?**

Several inorganic ions are detected from the bitumen with L2MS (VO^+, HVO^+, VO_2^+, Fe^+, $CaOH^+$, As^+, AsH^+) and with ToF-SIMS (Fe^+, Cr^+, Ni^+, Mn^+, VO^+, K^+, Na^+). $CaOH^+$ is likely a faint remnant of the dominant carbonate matrix taken in the bitumen; similarly K^+ and Na^+ are possible faint contaminants or from the minor elements of the Orbagnoux rocks, and are over-represented in ToF-SIMS due to the very high sensitivity of the technique to these cations (e.g., Thiel and Sjövall, 2015). In contrast, V and Ni represent elements that occur at 30–70 ppm concentrations in the bulk of Orbagnoux rocks (Mongenot et al., 2000). Thus the detection of their cations with ToF-SIMS and/or L2MS in the bitumen argues that these elements have been concentrated by the OM extraction.

Geoporphyrins are a likely source of organo-metallic molecules. These can be diagenetic products of biomolecules such as chlorophylls, where the chelated Mg^{2+} within the heme group is most commonly replaced by Ni^{2+}, VO^{2+}, or Fe^{2+} (El-Sabagh et al., 2017; Killops and Killops, 2005). In addition, reduced porphyrins with nickel are produced biologically by methanogenic Archaea as the enzyme cofactor F430 (Krüger et al., 2003). Our observation of a red ring during chromatographic fractionation of the DP bitumen indicates that geoporphyrins are common in Orbagnoux samples. Cations of Fe, Mn, and Cr can also originate from geoporphyrins (McKenna et al., 2021; Munoz et al., 2019). The VO^+ and HVO^+ ions were also detected in the kerogen (not shown), suggesting a possible binding of geoporphyrins to its macromolecular network. However, the remains of mineral phases (CaF_2 and FeS_2) in the kerogen so far prevent unambiguous assignment of the metallic ions to the kerogen. The VO^+ ions were also detected in the fresh rock, possibly from VO-porphyrins or minerals (V^{III}-oxides or -hydroxides, clays: Tribovillard et al., 2006).

Importantly, we could not detect organic fragments from geoporphyrins. This might be due to a "matrix" suppression effect (Knochenmuss, 2003; McCombie and Knochenmuss, 2004) generated by other bitumen molecules. Indeed, porphyrin-class molecules have been used as matrices in matrix-assisted LDI-MS (Chen and Ling, 2002), although–to the best of our knowledge–matrix suppression effect of the porphyrin matrix (by charge transfer to analytes) is not known, in particular for geoporphyrin-relevant molecules. Here, the inorganic metallic ions have been best detected in analytical conditions that also generated carbon clusters, that is, conditions more prone to fragmentation of organic molecules. In these analyses, the fragmentation may have been too extensive to distinguish diagnostic high-mass organic fragments from geoporphyrins.

It is likely that the V, Fe, Ni, Cr, and Mn detected in the bitumen were organically-bound. Trapping of molybdenum by sulfurized OM has been evidenced in Orbagnoux rocks (Tribovillard et al., 2004) by correlations between total organic carbon (TOC) values and Mo/Al* enrichment factors (where Mo/Al* = (Mo/Al) sample / (Mo/Al) average shale). Using published bulk-rock data (Mongenot et al., 2000), we plotted V/Al* and Ni/Al* ratios against TOC, but only found an increasing trend with weak linear correlation R^2 of 0.48 and 0.56, respectively. In contrast, raw V/Al and Ni/Al ratios yielded positive correlations with linear correlation R^2 of 0.72 and 0.75. Due to the aluminous content (which may indicate input of mineral V and Ni in clay mineral) being extremely small, these correlations of V/Al and Ni/Al further support the association of these metals with organic molecules in the Orbagnoux bitumen.

5.7. **Effect of mineral matrix**

Here, even in presence of abundant organic matter in the fresh rock, relatively low signal and interference of inorganic ions (or possibly formation of organic-inorganic adducts) made the detection and interpretation of L2MS data less straightforward than that recorded on extracted OM. In contrast, PAHs and functionalized polycyclic aromatic pigment molecules appeared readily detected at trace levels with LDI-MS on mineral surfaces (Goesmann et al., 2017; Li et al., 2015), possibly due to their high ionization efficiency (as discussed for PAHs above). Here, the mineral matrix was dominated by Ca-carbonate minerals, for which possible sedimentary counterparts are still–to our knowledge–lacking on Mars (McMahon et al., 2018). However, similar difficulties in detecting/assigning organic molecules arose in LDI-MS of silicified "fresh" microorganisms (Siljeström et al., 2021) and Antarctic sediments (Bishop et al., 2013).

Differences in matrix effects have been observed for various minerals, possibly linked with variations in desorption efficiency of the trace PAH studied (Goesmann et al., 2017; Li et al., 2015), to which we may add possible suppression effects as discussed above. In the case of OM-rich samples such as "fresh" microorganisms or immature fossil OM, the low absorption and/or ionization efficiencies at 266 nm likely limit more the signal intensity than mineral matrix adsorption. Several possibilities could help enhance this signal in L2MS, including use of distinct desorption wavelengths (e.g., resonant IR desorption for some classes of molecules: Mihesan et al., 2006; Uckert et al., 2018), or single-photon post-ionization with VUV radiation (Hanley and Zimmermann, 2009).

6. Conclusions and perspectives

Previous reports of L2MS studies on fossil OM essentially reported on PAHs. Here we show that L2MS as well as LDI-MS can detect a wider range of organic molecules in immature fossil

OM. These include fragments of hydrocarbons with high H/C ratios, although these are relatively small and faintly detected relative to low H/C aromatics, likely due to the selective fragmentation of aliphatic groups and preferential ionization of aromatics via two-photon REMPI schemes. Vacuum UV wavelengths (<200 nm) may be used to enable single-photon ionization schemes in order to span a greater molecular diversity with laser-assisted MS (Hanley and Zimmermann, 2009; Streibel et al., 2021), likely similar to that reached by SIMS. L2MS, as shown herein, would likely provide lower fragmentation than SIMS due to lower energy of UV photons compared to primary ions.

We show that the L2MS (as well as LDI-MS) technique is very sensitive to sulfurated molecules where S is included in an aromatic structure. We performed experiments with highly concentrated samples (solidified bitumen and kerogen) and organic-matter rich rock (likely 5-12 wt% organic C), thus evaluation of the detection limits is beyond the scope of the present study. We note, however, that attomole-range limits of detection (per laser shot) have been reported for PAHs in L2MS using a similar orthogonal reflectron ToF-MS as used herein (Sabbah et al., 2017). The major difficulty arising in distinguishing these sulfurated molecules is the requirement of i) high mass-resolution, and/or ii) minimization of the formation of carbonaceous clusters with very low H/C that may overlap with sulfurated molecules in mass spectra, iii) and/or additional tandem MS. High-mass resolution has been attained in space-prototype LDI-Orbitrap^{TM} instruments (Arevalo et al., 2023; Briois et al., 2016; Selliez et al., 2019), and tandem MS is feasible with the MOMA LDI-MS instrument (Goesmann et al., 2017). L2MS, which can help minimize the formation of low H/C clusters as shown here, has also been developed for space mission prototypes (Getty et al., 2017, 2012).

Unfortunately, we show that low-H carbonaceous clusters may be generated at moderate desorption fluence (0.2 J/cm², 532 nm) more abundantly from OM in mineral matrices compared to the demineralized situation. Here this did not prevent detection of sulfurated organic molecules in the rock, thanks to the generation of negatively charged S-bearing carbonaceous clusters. Minimization of fragmentation and/or matrix effects should be further assessed with higher (IR) desorption wavelengths (Sabbah et al., 2022; Uckert et al., 2018). Laser-assisted mass spectrometry thus appears a promising technique to analyze sulfurated molecules *in situ* (e.g., with the MOMA experiment) and/or in precious samples such as those that will be returned from Mars. Further investigation of fossil OM using additional desorption/ionization wavelength(s) would likely benefit the investigation of organics *in situ* in rocks with L2MS and LDI-MS.

Small aromatics (≤ 14 carbons) dominate in LDI and L2MS spectra of the immature Orbagnoux rock, bitumen, and to a lesser extent of the kerogen. Larger aromatic structures are generally observed with L2MS in meteorites, and are also expected from highly mature terrestrial OM. Sulfur-bearing molecules as those detected in Orbagnoux with LDI/L2MS may also be found in meteorites, although possibly in lower amounts relative to hydrocarbons. Further comparative studies of fossil OM of various maturities and origins and abiotic OM (including meteorites) with similar LDI/L2MS analytical parameters may help distinguish potential biosignatures.

Kerogens (from fossil OM) usually absorb best in the UV, and close to maximum for 266 nm (energy of 4.66 eV) photons (Ferralis et al., 2015). This likely contributed to the detection of aromatics with LDI-MS at 266 nm in the Orbagnoux kerogen. Here, differences appear between analyses of bitumen and kerogen (which was thoroughly extracted from soluble molecules), in particular as the latter shows a higher signal at m/z over 175 (likely dominated by alkylated PAHs) and more prominent N-moieties. This suggests that fragmentation of the

macromolecular structure of kerogen contributes to the ions detected in our L2MS and LDI-MS experiments. In contrast, a previous study argued that 355 nm desorption with a slightly lower fluence (~0.04 J/cm²) as those used here could not fragment the macromolecular structure of meteoritic insoluble OM, and could only release trapped/adsorbed (not covalently-bound) molecules (Danger et al., 2020). This might be linked to different responses of OM between 266 and 355 nm LDI-MS (Aubriet et al., 2018).

Using pyrolysis GC-MS, van Kaam-Peters and Sinninghe Damsté (1997) observed a "*striking similarity between the kerogen and asphaltene pyrolysates*". This similarity is consistent with formation of the kerogen by sulfur cross-linking of labile molecules (Werne et al., 2004). However, we observed possible enrichments in N-moieties in the kerogen. These may correspond to contribution of bacterial biomass, e.g. from cyanobacteria, in line with the observation of ultralaminae suggestive of cyanobacterial photosynthetic membranes in the Orbagnoux kerogen (Pacton et al., 2006). The possibility to show distinct molecular signatures in the kerogen (compared to the extracted bitumen) with L2MS or LDI-MS offers perspective to distinguish further the molecular composition of individual microfossils. Indeed, heterogeneities discerned with spectroscopy among different morphospecies of the same rock (Lepot, 2021) strongly argue for selective preservation of biomacromolecule derivatives (Vandenbroucke and Largeau, 2007). Their individual mass spectrometric characterization enabled by the small sampling size offered by lasers may open the way to chemotaxonomy.

Abbreviations used

DCM = dichloromethane (solvent to extract soluble organic molecules)

FT-ICR = Fourier-transform ion cyclotron resonance (type of mass analysis)

GC-MS = gas chromatography-mass spectrometry

LD = laser desorption and/or ablation

LDI = laser desorption-ionization

LI = laser ionization

LDI-MS = single-step laser desorption-ionization mass spectrometry

L2MS = two-step (LD followed by LI) laser desorption-ionization mass spectrometry

Me = methanol (solvent)

MOMA = Mars Organic Molecule Analyzer

MS = mass spectrometry

NMR = Nuclear magnetic resonance (spectroscopy method)

OM = organic matter

PAH = polycyclic aromatic hydrocarbon

Ppm = parts per million (here used for mass measurement errors)

Py-GC-MS = pyrolysis GC-MS

REMPI = resonance-enhanced multiphoton ionization

TIC = total ion count

ToF = time-of-flight (type of mass analyzer)

ToF-SIMS = time-of-flight secondary-ion mass spectrometry

Aknowledgements

Dmitrii Egorov and Tirthankar Mitra (PhLAM) are thanked for help with L2MS experiments. Sylvie Regnier (Unité Evolution, Ecologie et Paléontologie, EEP, U. Lille) is thanked for performing kerogen extraction. Monique Gentric is thanked for the budget management at the University of Lille. Sandra Ventalon (LOG, U. Lille) is thanked for help with microscopy. Daniel Colin (technical director of Société des Mines d'Orbagnoux) is thanked for his help during rock sampling. We thank three anonymous reviewers for their insightful comments that helped improve this manuscript, as well as Dr. S.L. Cady, Editor in Chief.

Author contributions

Project design by KL, CF, YC and ST. N.T. collected the sample and discussed its petrography and chemistry (by ST and KL). ST prepared samples with help of AT, AR, and KL. ST performed all L2MS experiments, with help of DD, MV, YC, KL, CF and MB. ST, AT and JS performed Py-GC-MS. AR performed GC-MS. ST and NN performed ToF-SIMS. L2MS and ToF-SIMS data analyzed by ST, KL, CF, YC and DD. KL, ST, AT and AR analyzed Py-GC-MS data. KL and ST wrote the manuscript, with contributions from all co-authors.

Conflict of Interest

The authors have no conflicts of interest to declare.

Funding Information

Funding was provided by the French National Research Agency (ANR) M6fossils grant under contract ANR-15-CE31-0003-01 to K.L and the Région Hauts-de-France (Visionn'AIRR program, project iM4). S.T. doctoral contract received a co-funding by Région Hauts-de-France. The authors thank the Région Hauts-de-France, and the Ministère de l'Enseignement Supérieur et de la Recherche, and the European Fund for Regional Economic Development for their financial support through the CPER Climibio program. The CaPPA project (Chemical and Physical Properties of the Atmosphere) is funded by the French National Research Agency (ANR) through the PIA (Programme d'Investissement d'Avenir) under contract « ANR-11-

LABX-0005-01 » and by the Regional Council « Hauts-de-France » and the « European Funds for Regional Economic Development » (FEDER).

References

Arevalo R, Willhite L, Bardyn A, et al. Laser Desorption Mass Spectrometry with an Orbitrap Analyser for in Situ Astrobiology. Nat Astron 2023;7(3):359–365; doi: 10.1038/s41550-022-01866-x.

Aubriet F, Ghislain T, Hertzog J, et al. Characterization of Biomass and Biochar by LDI-FTICRMS – Effect of the Laser Wavelength and Biomass Material. J Am Soc Mass Spectrom 2018;29(10):1951–1962; doi: 10.1007/s13361-018-2005-z.

Bennett B, Lager A, Russell CA, et al. Hydropyrolysis of Algae, Bacteria, Archaea and Lake Sediments; Insights into the Origin of Nitrogen Compounds in Petroleum. Org Geochem 2004;35(11-12 SPEC. ISS.):1427–1439; doi: 10.1016/j.orggeochem.2004.07.006.

Bishop JL, Franz HB, Goetz W, et al. Coordinated Analyses of Antarctic Sediments as Mars Analog Materials Using Reflectance Spectroscopy and Current Flight-like Instruments for CheMin, SAM and MOMA. Icarus 2013;224(2):309–325; doi: 10.1016/j.icarus.2012.05.014.

Boesl U and Zimmermann R. Fundamentals and Mechanisms of Resonance-Enhanced Multiphoton Ionization (REMPI) in Vacuum and Its Application in Molecular Spectroscopy. In: Photoionization and Photo-Induced Processes in Mass Spectrometry Wiley; 2021; pp. 23–88; doi: 10.1002/9783527682201.ch2.

Briois C, Thissen R, Thirkell L, et al. Orbitrap Mass Analyser for in Situ Characterisation of Planetary Environments: Performance Evaluation of a Laboratory Prototype. Planet Space Sci 2016;131:33–45; doi: 10.1016/j.pss.2016.06.012.

Brocks JJ, Love GD, Snape CE, et al. Release of Bound Aromatic Hydrocarbons from Late Archean and Mesoproterozoic Kerogens via Hydropyrolysis. Geochim Cosmochim Acta 2003;67(8):1521–1530; doi: 10.1016/S0016-7037(00)01302-9.

Brown RL and Stein SE. Boiling Point Data. In: WebBook de Chimie NIST, Base de Données Standard de Référence NIST Numéro 69. (Linstrom PJ and Mallard WG. eds) National Institute of Standards and Technology: Gaithersburg MD, 20899; 2022; doi: 10.18434/T4D303.

Chen Y-T and Ling Y-C. Detection of Water-Soluble Vitamins by Matrix-Assisted Laser Desorption/Ionization Time-of-Flight Mass Spectrometry Using Porphyrin Matrices. J Mass Spectrom 2002;37(7):716–730; doi: 10.1002/jms.332.

Cho Y, Witt M, Jin JM, et al. Evaluation of Laser Desorption Ionization Coupled to Fourier Transform Ion Cyclotron Resonance Mass Spectrometry To Study Metalloporphyrin Complexes. Energy & Fuels 2014;28(11):6699–6706; doi: 10.1021/ef500997m.

Cho Y, Witt M, Kim YH, et al. Characterization of Crude Oils at the Molecular Level by Use of Laser Desorption Ionization Fourier-Transform Ion Cyclotron Resonance Mass Spectrometry. Anal Chem 2012;84(20):8587–8594; doi: 10.1021/ac301615m.

Clemett SJ, Dulay MT, Seb Gillette J, et al. Evidence for the Extraterrestrial Origin of

Polycyclic Aromatic Hydrocarbons in the Martian Meteorite ALH84001. Faraday Discuss 1998;109(109):417–436; doi: 10.1039/a709130c.

Clemett SJ and Zare RN. Microprobe Two-Step Laser Mass Spectrometry as an Analytical Tool for Meteoritic Samples. IAU Symp 178 Mol Astrophys Probes Process 1996;178:305.

Copelin EC and Larter SR. Chemical Characterization of Aromatic Hydrocarbons, Kerogen, and Humic Acids in Deep Sea Drilling Project Leg 71 Cores. In: Initial Reports of the Deep Sea Drilling Project, 71 U.S. Government Printing Office: Washington; 1983; doi: 10.2973/dsdp.proc.71.140.1983.

Dale MJ, Costello KF, Jones AC, et al. Investigation of Porphyrins and Metalloporphyrins Using Two-Step Laser Mass Spectrometry. J Mass Spectrom 1996;31(6):590–601; doi: 10.1002/(SICI)1096-9888(199606)31:6<590::AID-JMS308>3.0.CO;2-C.

Danger G, Ruf A, Maillard J, et al. Unprecedented Molecular Diversity Revealed in Meteoritic Insoluble Organic Matter: The Paris Meteorite's Case. Planet Sci J 2020;1(3):55; doi: 10.3847/PSJ/abb60f.

Desgroux P, Mercier X and Thomson KA. Study of the Formation of Soot and Its Precursors in Flames Using Optical Diagnostics. Proc Combust Inst 2013;34(1):1713–1738; doi: 10.1016/j.proci.2012.09.004.

Donnarumma F, Murray KK and Hanley L. Fundamentals of Laser Desorption Ionization. In: Photoionization and Photo-Induced Processes in Mass Spectrometry Wiley; 2021; pp. 305–325; doi: 10.1002/9783527682201.ch9.

Eigenbrode JL, Summons RE, Steele A, et al. Organic Matter Preserved in 3-Billion-Year-Old Mudstones at Gale Crater, Mars. Science (80-) 2018;360(6393):1096–1101; doi: 10.1126/science.aas9185.

El-Sabagh SM, Faramawi S, Harb FM, et al. Preliminary Study of Metalloporphyrins in Some Oil Shales, Red Sea, Egypt. Egypt J Pet 2017;26(1):135–143; doi: 10.1016/j.ejpe.2015.11.004.

Elsila JE, de Leon NP, Buseck PR, et al. Alkylation of Polycyclic Aromatic Hydrocarbons in Carbonaceous Chondrites. Geochim Cosmochim Acta 2005;69(5):1349–1357; doi: 10.1016/j.gca.2004.09.009.

Faccinetto A, Desgroux P, Ziskind M, et al. High-Sensitivity Detection of Polycyclic Aromatic Hydrocarbons Adsorbed onto Soot Particles Using Laser Desorption/Laser Ionization/Time-of-Flight Mass Spectrometry: An Approach to Studying the Soot Inception Process in Low-Pressure Flames. Combust Flame 2011;158(2):227–239; doi: 10.1016/j.combustflame.2010.08.012.

Faccinetto A, Focsa C, Desgroux P, et al. Progress toward the Quantitative Analysis of PAHs Adsorbed on Soot by Laser Desorption/Laser Ionization/Time-of-Flight Mass Spectrometry. Environ Sci Technol 2015;49(17):10510–10520; doi: 10.1021/acs.est.5b02703.

Faccinetto A, Thomson K, Ziskind M, et al. Coupling of Desorption and Photoionization Processes in Two-Step Laser Mass Spectrometry of Polycyclic Aromatic Hydrocarbons. Appl Phys A Mater Sci Process 2008;92(4):969–974; doi: 10.1007/s00339-008-4605-0.

Fadel A, Lepot K, Nuns N, et al. New Preparation Techniques for Molecular and In-Situ

Analysis of Ancient Organic Micro- and Nanostructures. Geobiology 2020;18(4):445–461; doi: 10.1111/gbi.12380.

Ferralis N, Liu Y, Bake KD, et al. Direct Correlation between Aromatization of Carbon-Rich Organic Matter and Its Visible Electronic Absorption Edge. Carbon N Y 2015;88:139–147; doi: 10.1016/j.carbon.2015.02.075.

Fray N, Bardyn A, Cottin H, et al. High-Molecular-Weight Organic Matter in the Particles of Comet 67P/Churyumov-Gerasimenko. Nature 2016;538(7623):72–74; doi: 10.1038/nature19320.

Freissinet C, Glavin DP, Mahaffy PR, et al. Organic Molecules in the Sheepbed Mudstone, Gale Crater, Mars. J Geophys Res Planets 2015;120(3):495–514; doi: 10.1002/2014JE004737.

Getty SA, Brinckerhoff WB, Cornish T, et al. Compact Two-Step Laser Time-of-Flight Mass Spectrometer for in Situ Analyses of Aromatic Organics on Planetary Missions. Rapid Commun Mass Spectrom 2012;26(23):2786–2790; doi: 10.1002/rcm.6393.

Getty SA, Elsila J, Balvin M, et al. Molecular Analyzer for Complex Refractory Organic-Rich Surfaces (MACROS). IEEE Aerosp Conf Proc 2017; doi: 10.1109/AERO.2017.7943706.

Goesmann F, Brinckerhoff WB, Raulin F, et al. The Mars Organic Molecule Analyzer (MOMA) Instrument: Characterization of Organic Material in Martian Sediments. Astrobiology 2017;17(6–7):655–685; doi: 10.1089/ast.2016.1551.

Greenwalt DE, Goreva YS, Siljestrom SM, et al. Hemoglobin-Derived Porphyrins Preserved in a Middle Eocene Blood-Engorged Mosquito. Proc Natl Acad Sci 2013;110(46):18496–18500; doi: 10.1073/pnas.1310885110.

Gross JH. Mass Spectrometry. Springer International Publishing: Cham; 2017.; doi: 10.1007/978-3-319-54398-7.

Haefliger OP and Zenobi R. Laser Mass Spectrometric Analysis of Polycyclic Aromatic Hydrocarbons with Wide Wavelength Range Laser Multiphoton Ionization Spectroscopy. Anal Chem 1998;70(13):2660–2665; doi: 10.1021/ac971264f.

Hahn JH, Zenobi R, Bada JL, et al. Application of Two-Step Laser Mass Spectrometry to Cosmogeochemistry: Direct Analysis of Meteorites. Science (80-) 1988;239(4847):1523–1525; doi: 10.1126/science.239.4847.1523.

Hanley L and Zimmermann R. Light and Molecular Ions: The Emergence of Vacuum UV Single-Photon Ionization in MS. Anal Chem 2009;81(11):4174–4182; doi: 10.1021/ac8013675.

Hurtado P, Gámez F and Martínez-Haya B. One- and Two-Step Ultraviolet and Infrared Laser Desorption Ionization Mass Spectrometry of Asphaltenes. Energy & Fuels 2010;24(11):6067–6073; doi: 10.1021/ef101139f.

Javaux EJ and Lepot K. The Paleoproterozoic Fossil Record: Implications for the Evolution of the Biosphere during Earth's Middle-Age. Earth-Science Rev 2018;176(September 2017):68–86; doi: 10.1016/j.earscirev.2017.10.001.

van Kaam-Peters HME, Rijpstra WIC, de Leeuw JW, et al. A High Resolution Biomarker

Study of Different Lithofacies of Organic Sulfur-Rich Carbonate Rocks of a Kimmeridgian Lagoon (French Southern Jura). Org Geochem 1998;28(3–4):151–177; doi: 10.1016/S0146-6380(97)00132-0.

van Kaam-Peters HME and Sinninghe Damsté JS. Characterisation of an Extremely Organic Sulphur-Rich, 150 Ma Old Carbonaceous Rock: Palaeoenvironmental Implications. Org Geochem 1997;27(7–8):371–397; doi: 10.1016/S0146-6380(97)00082-X.

Kaufmann A and Walker S. Coalescence and Self-Bunching Observed in Commercial High-Resolution Mass Spectrometry Instrumentation. Rapid Commun Mass Spectrom 2018;32(6):503–515; doi: 10.1002/rcm.8054.

Killops S and Killops V. Introduction to Organic Geochemistry, 2nd Edition. Blackwell: Oxford; 2005.

Kipfer KA, Ligterink NFW, Bouwman J, et al. Toward Detecting Polycyclic Aromatic Hydrocarbons on Planetary Objects with ORIGIN. Planet Sci J 2022;3(2):43; doi: 10.3847/PSJ/ac4e15.

Knicker H, Scaroni AW and Hatcher PG. 13C and 15N NMR Spectroscopic Investigation on the Formation of Fossil Algal Residues. Org Geochem 1996;24(6–7):661–669; doi: 10.1016/0146-6380(96)00057-5.

Knochenmuss R. A Quantitative Model of Ultraviolet Matrix-Assisted Laser Desorption/Ionization Including Analyte Ion Generation. Anal Chem 2003;75(10):2199–2207; doi: 10.1021/ac034032r.

Krüger M, Meyerdierks A, Glöckner FO, et al. A Conspicuous Nickel Protein in Microbial Mats That Oxidize Methane Anaerobically. Nature 2003;426(6968):878–881; doi: 10.1038/nature02207.

Lepot K. Signatures of Early Microbial Life from the Archean (4 to 2.5 Ga) Eon. Earth-Science Rev 2020;209:103296; doi: 10.1016/j.earscirev.2020.103296.

Lepot K. Microfossils, Analytical Techniques. In: Encyclopedia of Astrobiology. (Al. GM et. ed) Springer Berlin Heidelberg: Berlin, Heidelberg; 2021; pp. 1–16; doi: 10.1007/978-3-642-27833-4_1711-4.

Lepot K, Williford KH, Philippot P, et al. Extreme 13C-Depletions and Organic Sulfur Content Argue for S-Fueled Anaerobic Methane Oxidation in 2.72 Ga Old Stromatolites. Geochim Cosmochim Acta 2019;244:522–547; doi: 10.1016/j.gca.2018.10.014.

Levy RL, Grayson MA and Wolf CJ. The Organic Analysis of the Murchison Meteorite. Geochim Cosmochim Acta 1973;37(3):467–483; doi: 10.1016/0016-7037(73)90212-3.

Li X, Danell RM, Brinckerhoff WB, et al. Detection of Trace Organics in Mars Analog Samples Containing Perchlorate by Laser Desorption/Ionization Mass Spectrometry. Astrobiology 2015;15(2):104–110; doi: 10.1089/ast.2014.1203.

Lias SG, Bartmess JE, Liebman JF, et al. Ion Energetics Data. In: WebBook de Chimie NIST, Base de Données Standard de Référence NIST Numéro 69 National Institute of Standards and Technology: Gaithersburg MD, 20899; 2022; doi: 10.18434/T4D303.

Ligterink N, Riedo A, Tulej M, et al. Detecting the Elemental and Molecular Signatures of

Life: Laser-Based Mass Spectrometry Technologies. 2021.; doi: 10.3847/25c2cfeb.782ec4d0.

Ligterink NFW, Grimaudo V, Moreno-García P, et al. ORIGIN: A Novel and Compact Laser Desorption – Mass Spectrometry System for Sensitive in Situ Detection of Amino Acids on Extraterrestrial Surfaces. Sci Rep 2020;10(1):9641; doi: 10.1038/s41598-020-66240-1.

Lindgren J, Sjövall P, Carney RM, et al. Skin Pigmentation Provides Evidence of Convergent Melanism in Extinct Marine Reptiles. Nature 2014;506(7489):484–488; doi: 10.1038/nature12899.

Lindgren J, Uvdal P, Sjövall P, et al. Molecular Preservation of the Pigment Melanin in Fossil Melanosomes. Nat Commun 2012;3:824; doi: 10.1038/ncomms1819.

Mahaffy PR, Webster CR, Cabane M, et al. The Sample Analysis at Mars Investigation and Instrument Suite. Space Sci Rev 2012;170(1–4):401–478; doi: 10.1007/s11214-012-9879-z.

Mahajan TB, Plows FL, Gillette JS, et al. Comparison of Microprobe Two-Step Laser Desorption/Laser Ionization Mass Spectrometry and Gas Chromatography/ Mass Spectrometry Studies of Polycyclic Aromatic Hydrocarbons in Ancient Terrestrial Rocks. J Am Soc Mass Spectrom 2001;12(9):989–1001; doi: 10.1016/S1044-0305(01)00279-3.

Marshall CP, Love GD, Snape CE, et al. Structural Characterization of Kerogen in 3.4 Ga Archaean Cherts from the Pilbara Craton, Western Australia. Precambrian Res 2007;155(1–2):1–23; doi: 10.1016/j.precamres.2006.12.014.

Masclet P, Cachier H, Liousse C, et al. Emissions of Polycyclic Aromatic Hydrocarbons by Savanna Fires. J Atmos Chem 1995;22(1–2):41–54; doi: 10.1007/BF00708180.

McCombie G and Knochenmuss R. Small-Molecule MALDI Using the Matrix Suppression Effect To Reduce or Eliminate Matrix Background Interferences. Anal Chem 2004;76(17):4990–4997; doi: 10.1021/ac049581r.

McKenna AM, Chacón-Patiño ML, Salvato Vallverdu G, et al. Advances and Challenges in the Molecular Characterization of Petroporphyrins. Energy & Fuels 2021;35(22):18056–18077; doi: 10.1021/acs.energyfuels.1c02002.

McLafferty FW and Tureek F. Interpretation of Mass Spectra. Fourth edi. University Science Books: Sausalito, CA; 1993.

McMahon S, Bosak T, Grotzinger JP, et al. A Field Guide to Finding Fossils on Mars. J Geophys Res Planets 2018;123(5):1012–1040; doi: 10.1029/2017JE005478.

Messenger S, Amari S, Gao X, et al. Indigenous Polycyclic Aromatic Hydrocarbons in Circumstellar Graphite Grains from Primitive Meteorites. Astrophys J 1998;502(1):284–295; doi: 10.1086/305874.

Mihesan C, Ziskind M, Therssen E, et al. IR Laser Resonant Desorption of Polycyclic Aromatic Hydrocarbons. Chem Phys Lett 2006;423(4–6):407–412; doi: 10.1016/j.cplett.2006.04.032.

Mihesan C, Ziskind M, Therssen E, et al. Parametric Study of Polycyclic Aromatic Hydrocarbon Laser Desorption. J Phys Condens Matter 2008;20(2):025221; doi: 10.1088/0953-8984/20/02/025221.

Mongenot T, Derenne S, Largeau C, et al. Spectroscopic, Kinetic and Pyrolytic Studies of Kerogen from the Dark Parallel Laminae Facies of the Sulphur-Rich Orbagnoux Deposit (Upper Kimmeridgian, Jura). Org Geochem 1999;30(1):39–56; doi: 10.1016/S0146-6380(98)00199-5.

Mongenot T, Tribovillard NP, Arbey F, et al. Comparative Studies of a High Resolution Sampling of the Different Facies of the Organic-Rich Orbagnoux Deposit (Upper Kimmeridgian, Jura): Petrographic and Bulk Geochemical Approach. Extent and Origin of Interfacies and Intrafacies Variations. Bull la Soc Geol Fr 2000;171(1):23–36.

Munoz G, Gunessee BK, Bégué D, et al. Redox Activity of Nickel and Vanadium Porphyrins: A Possible Mechanism behind Petroleum Genesis and Maturation? RSC Adv 2019;9(17):9509–9516; doi: 10.1039/C9RA01104H.

National Center for Biotechnology Information. PubChem Compound Summary for CID 6623, Bisphenol A. 2022. Available from: https://pubchem.ncbi.nlm.nih.gov/compound/bisphenol-A [Last accessed: 6/29/2022].

Ngo LD, Duca D, Carpentier Y, et al. Chemical Discrimination of the Particulate and Gas Phases of MiniCAST Exhausts Using a Two-Filter Collection Method. Atmos Meas Tech 2020;13(2):951–967; doi: 10.5194/amt-13-951-2020.

NIST Mass Spectrometry Data Center. Mass Spectra. National Institute of Standards and Technology: Gaithersburg MD; 2022.; doi: 10.18434/T4D303.

Van Orden A and Saykally RJ. Small Carbon Clusters: Spectroscopy, Structure, and Energetics. Chem Rev 1998;98(6):2313–2357; doi: 10.1021/cr970086n.

Pacton M, Fiet N and Gorin G. Revisiting Amorphous Organic Matter in Kimmeridgian Laminites: What Is the Role of the Vulcanization Process in the Amorphization of Organic Matter? Terra Nov 2006;18(6):380–387; doi: 10.1111/j.1365-3121.2006.00702.x.

Pagès A, Grice K, Welsh DT, et al. Lipid Biomarker and Isotopic Study of Community Distribution and Biomarker Preservation in a Laminated Microbial Mat from Shark Bay, Western Australia. Microb Ecol 2015;70(2):459–472; doi: 10.1007/s00248-015-0598-3.

Pomerantz AE, Hammond MR, Morrow AL, et al. Two-Step Laser Mass Spectrometry of Asphaltenes. J Am Chem Soc 2008;130(23):7216–7217; doi: 10.1021/ja801927v.

Pomerantz AE, Hammond MR, Morrow AL, et al. Asphaltene Molecular-Mass Distribution Determined by Two-Step Laser Mass Spectrometry. Energy and Fuels 2009;23(3):1162–1168; doi: 10.1021/ef8006239.

Rashby SE, Sessions AL, Summons RE, et al. Biosynthesis of 2-Methylbacteriohopanepolyols by an Anoxygenic Phototroph. Proc Natl Acad Sci U S A 2007;104(38):15099–15104; doi: 10.1073/pnas.0704912104.

Reemtsma T. Determination of Molecular Formulas of Natural Organic Matter Molecules by (Ultra-) High-Resolution Mass Spectrometry. J Chromatogr A 2009;1216(18):3687–3701; doi: 10.1016/j.chroma.2009.02.033.

Remusat L, Derenne S, Robert F, et al. New Pyrolytic and Spectroscopic Data on Orgueil and Murchison Insoluble Organic Matter: A Different Origin than Soluble? Geochim Cosmochim Acta 2005;69(15):3919–3932; doi: 10.1016/j.gca.2005.02.032.

Riboulleau A, Derenne S, Sarret G, et al. Pyrolytic and Spectroscopic Study of a Sulphur-Rich Kerogen from the “Kashpir Oil Shales” (Upper Jurassic, Russian Platform). Org Geochem 2000;31(12):1641–1661.

Rybicki M, Marynowski L and Simoneit BRT. Benzohopane Series, Their Novel Di-, Tri-, and Tetraaromatic Derivatives, and Diaromatic 23- and 24-Norbenzohopanes from the Lower Jurassic Blanowice Formation, Southern Poland. Energy & Fuels 2017;31(3):2617–2624; doi: 10.1021/acs.energyfuels.6b03154.

Sabbah H, Bonnamy A, Papanastasiou D, et al. Identification of PAH Isomeric Structure in Cosmic Dust Analogs: The AROMA Setup. Astrophys J 2017;843(1):34; doi: 10.3847/1538-4357/aa73dd.

Sabbah H, Carlos M, Jenniskens P, et al. Detection of Cosmic Fullerenes in the Almahata Sitta Meteorite: Are They an Interstellar Heritage? Astrophys J 2022;931(2):91; doi: 10.3847/1538-4357/ac69dd.

Sabbah H, Carlos M and Joblin C. Characterization of Large Carbonaceous Molecules in Cosmic Dust Analogues and Meteorites. Proc Int Astron Union 2019;15(S350):103–106; doi: 10.1017/S1743921319008354.

Sabbah H, Morrow AL, Jenniskens P, et al. Polycyclic Aromatic Hydrocarbons in Asteroid 2008 TC3: Dispersion of Organic Compounds inside Asteroids. Meteorit Planet Sci 2010;45(10–11):1710–1717; doi: 10.1111/j.1945-5100.2010.01103.x.

Sabbah H, Morrow AL, Pomerantz AE, et al. Evidence for Island Structures as the Dominant Architecture of Asphaltenes. Energy and Fuels 2011;25(4):1597–1604; doi: 10.1021/ef101522w.

Sandford SA, Bajt S, Clemett SJ, et al. Assessment and Control of Organic and Other Contaminants Associated with the Stardust Sample Return from Comet 81P/Wild 2. Meteorit Planet Sci 2010;45(3):406–433; doi: 10.1111/j.1945-5100.2010.01031.x.

Sarret G, Mongenot T, Connan J, et al. Sulfur Speciation in Kerogens of the Orbagnoux Deposit (Upper Kimmeridgian, Jura) by XANES Spectroscopy and Pyrolysis. Org Geochem 2002;33(8):877–895; doi: 10.1016/S0146-6380(02)00066-9.

Schultz PH, Harris RS, Clemett SJ, et al. Preserved Flora and Organics in Impact Melt Breccias. Geology 2014;42:515–518.

Selliez L, Briois C, Carrasco N, et al. Identification of Organic Molecules with a Laboratory Prototype Based on the Laser Ablation-CosmOrbitrap. Planet Space Sci 2019;170:42–51; doi: 10.1016/j.pss.2019.03.003.

Sephton M and Gilmour I. Macromolecular Organic Materials in Carbonaceous Chondrites: A Review of Their Sources and Their Role in the Origin of Life on the Early Earth. Impacts and the Early Earth 2005;27–49; doi: 10.1007/bfb0027755.

Siljeström S, Li X, Brinckerhoff W, et al. ExoMars Mars Organic Molecule Analyzer (MOMA) Laser Desorption/Ionization Mass Spectrometry (LDI-MS) Analysis of Phototrophic Communities from a Silica-Depositing Hot Spring in Yellowstone National Park, USA. Astrobiology 2021;21(12):1515–1525; doi: 10.1089/ast.2020.2368.

Sinninghe Damsté JS and de Leeuw JW. Analysis, Structure and Geochemical Significance of

Organically-Bound Sulphur in the Geosphere: State of the Art and Future Research. Org Geochem 1990;16(4–6):1077–1101; doi: 10.1016/0146-6380(90)90145-P.

Slavicinska K, Duca D, Egorov D, et al. Link between Polycyclic Aromatic Hydrocarbon Size and Aqueous Alteration in Carbonaceous Chondrites Revealed by Laser Mass Spectrometry. ACS Earth Sp Chem 2022;6(6):1413–1428; doi: 10.1021/acsearthspacechem.2c00022.

Sleno L. The Use of Mass Defect in Modern Mass Spectrometry. J Mass Spectrom 2012;47(2):226–236; doi: 10.1002/jms.2953.

Smaniotto A, Montanari L, Flego C, et al. Can Crude Oils Be Distinguished by Different Component Distribution Obtained by Laser Desorption Ionization Mass Spectrometry and Evaluated by Chemometrics? Rapid Commun Mass Spectrom 2008;22(10):1597–1606; doi: 10.1002/rcm.3551.

Streibel T, Czech H and Zimmermann R. Analytical Application of Single-Photon Ionization Mass Spectrometry (SPI - MS) . Photoionization Photo-Induced Process Mass Spectrom 2021;89–124; doi: 10.1002/9783527682201.ch3.

Strohalm M, Kavan D, Novák P, et al. MMass 3: A Cross-Platform Software Environment for Precise Analysis of Mass Spectrometric Data. Anal Chem 2010;82(11):4648–4651; doi: 10.1021/ac100818g.

Szopa C, Freissinet C, Glavin DP, et al. First Detections of Dichlorobenzene Isomers and Trichloromethylpropane from Organic Matter Indigenous to Mars Mudstone in Gale Crater, Mars: Results from the Sample Analysis at Mars Instrument Onboard the Curiosity Rover. Astrobiology 2020;20(2):292–306; doi: 10.1089/ast.2018.1908.

Talrose V, Stern EB, Goncharova AA, et al. UV/Visible Spectra. In: WebBook de Chimie NIST, Base de Données Standard de Référence NIST Numéro 69. (Linstrom PJ and Mallard WG. eds) National Institute of Standards and Technology: Gaithersburg MD, 20899; 2021; doi: 10.18434/T4D303.

Tan YL, Kong A and Monetti MA. Biogenic Polycyclic Aromatic Hydrocarbons in an Alaskan Arctic Lake Sediment. Polycycl Aromat Compd 1996;9(1–4):185–192; doi: 10.1080/10406639608031217.

Thiel V and Sjövall P. Time-of-Flight Secondary Ion Mass Spectrometry (TOF-SIMS): Principles and Practice in the Biogeosciences. In: Principles and Practice of Analytical Techniques in Geosciences. (Grice K. ed) The Royal Society of Chemistry; 2015; pp. 122–170; doi: 10.1039/9781782625025-00122.

Thomson K, Ziskind M, Mihesan C, et al. Influence of the Photoionization Process on the Fragmentation of Laser Desorbed Polycyclic Aromatic Hydrocarbons. Appl Surf Sci 2007;253(15):6435–6441; doi: 10.1016/j.apsusc.2007.01.050.

Tribovillard N, Algeo TJ, Lyons T, et al. Trace Metals as Paleoredox and Paleoproductivity Proxies: An Update. Chem Geol 2006;232(1–2):12–32; doi: 10.1016/j.chemgeo.2006.02.012.

Tribovillard N, Riboulleau A, Lyons T, et al. Enhanced Trapping of Molybdenum by Sulfurized Marine Organic Matter of Marine Origin in Mesozoic Limestones and Shales. Chem Geol 2004;213(4):385–401; doi: 10.1016/j.chemgeo.2004.08.011.

Tribovillard N, Trentesaux A, Trichet J, et al. A Jurassic Counterpart for Modern Kopara of

the Pacific Atolls: Lagoonal, Organic Matter-Rich, Laminated Carbonate of Orbagnoux (Jura Mountains, France). Palaeogeogr Palaeoclimatol Palaeoecol 2000;156(3–4):277–288; doi: 10.1016/S0031-0182(99)00145-5.

Tribovillard NP, Gorin GE, Belin S, et al. Organic-Rich Biolaminated Facies from a Kimmeridgian Lagoonal Environment in the French Southern Jura Mountains-A Way of Estimating Accumulation Rate Variations. Palaeogeogr Palaeoclimatol Palaeoecol 1992;99(1–2):163–177; doi: 10.1016/0031-0182(92)90013-U.

Tulej M, Wiesendanger R, Riedo A, et al. Mass Spectrometric Analysis of the Mg Plasma Produced by Double-Pulse Femtosecond Laser Irradiation. J Anal At Spectrom 2018;33(8):1292–1303; doi: 10.1039/C8JA00036K.

Uckert K, Grubisic A, Li X, et al. IR Resonance-Enhanced Organic Detection with Two-Step Laser Desorption Time-of-Flight Mass Spectrometry. Icarus 2018;299:15–21; doi: 10.1016/j.icarus.2017.07.006.

Vandenbroucke M and Largeau C. Kerogen Origin, Evolution and Structure. Org Geochem 2007;38(5):719–833; doi: 10.1016/j.orggeochem.2007.01.001.

Vinogradoff V, Le Guillou C, Bernard S, et al. Paris vs. Murchison: Impact of Hydrothermal Alteration on Organic Matter in CM Chondrites. Geochim Cosmochim Acta 2017;212:234–252; doi: 10.1016/j.gca.2017.06.009.

Wakeham SG, Schaffner C and Giger W. Poly Cyclic Aromatic Hydrocarbons in Recent Lake Sediments—II. Compounds Derived from Biogenic Precursors during Early Diagenesis. Geochim Cosmochim Acta 1980;44(3):415–429; doi: 10.1016/0016-7037(80)90041-1.

Werne JP, Hollander DJ, Lyons TW, et al. Organic Sulfur Biogeochemistry : Recent Advances and Future Research Directions. Geol Soc Anerica 2004;379(4):135–150.

Zenobi R, Philippoz J-M, Buseck PR, et al. Spatially Resolved Organic Analysis of the Allende Meteorite. Science (80-) 1989;246(4933):1026–1029.

Zenobi R, Philippoz JM, Zare RN, et al. Organic Compounds in the Forest Vale, H4 Ordinary Chondrite. Geochim Cosmochim Acta 1992;56(7):2899–2905; doi: 10.1016/0016-7037(92)90366-Q.

Zhan Q, Zenobi R, Buseck PR, et al. Analysis of Polycyclic Aromatic Hydrocarbons in Kerogens Using Two-Step Laser Mass Spectrometry. Energy & Fuels 1997;11(1):144–149; doi: 10.1021/ef960120l.

Figure Captions

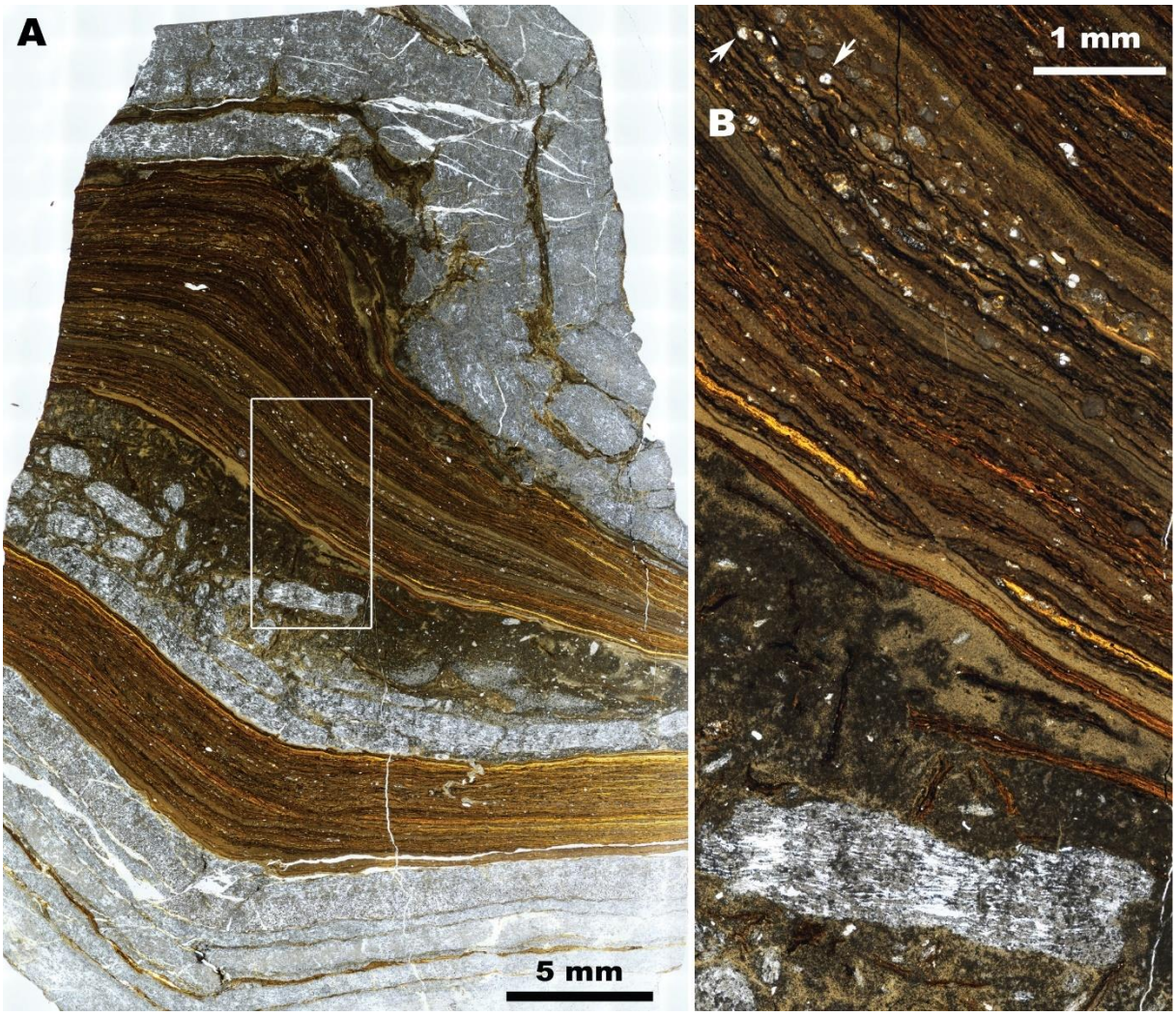

Fig. 1. Photomicrographs of the studied ORBA3 sample, of dark- and light-parallel laminae facies. Mosaic of high-dynamic-range images (multi-exposure image combination) recorded with a X5 objective on a Nikon Ni-E microscope. **(A)** Full thin section, and **(B)** zoom on the boxed area in (A). Light-grey parallel laminae comprise organic-matter-lean carbonate. Dark-parallel laminae comprise orange/brown organic-matter-rich laminae, where foraminifera are seen (arrows). Some carbonate layers in the central part of the section are brecciated.

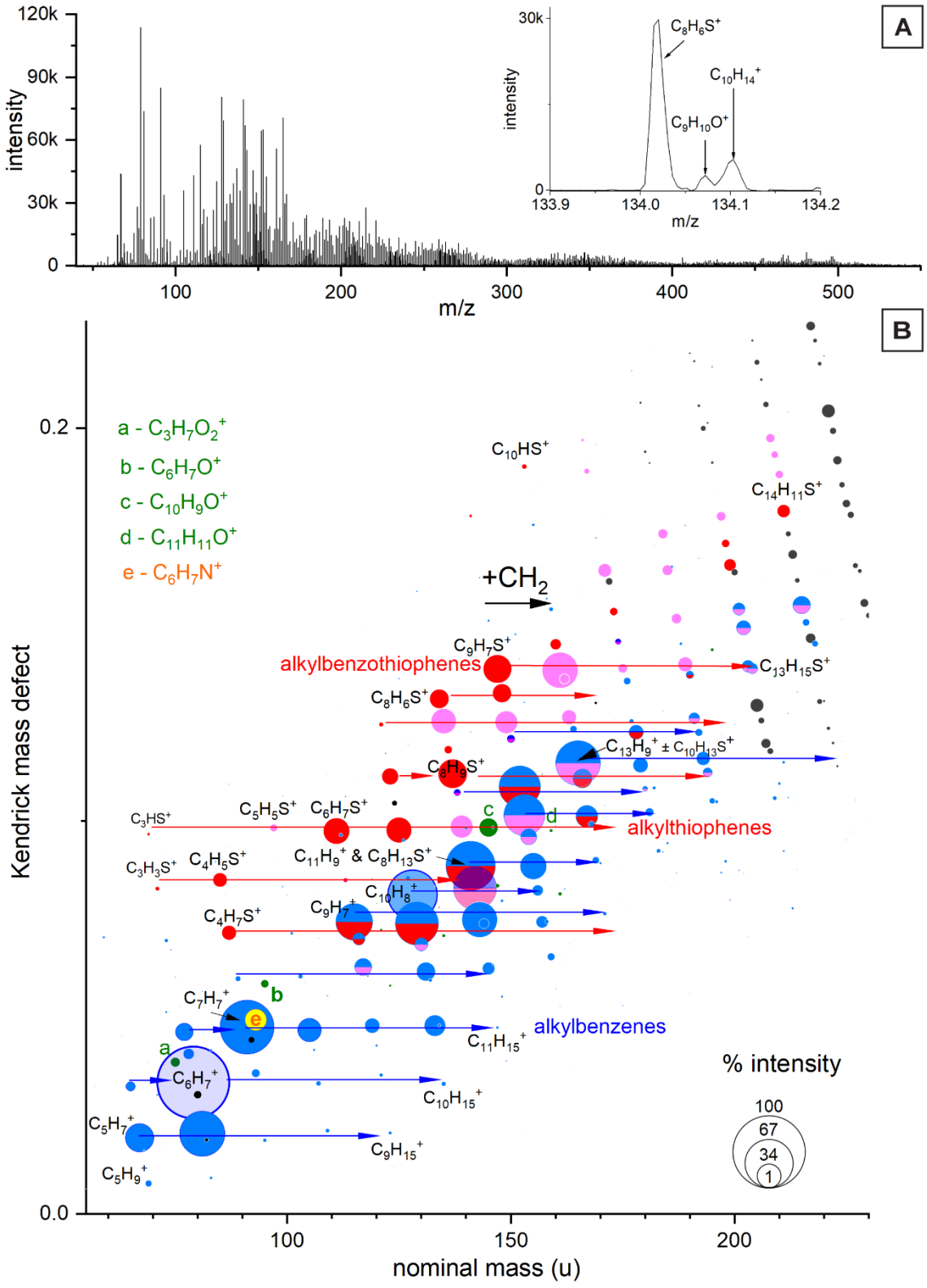

Fig. 2. ORBA3 bitumen, LDI-MS using 266 nm desorption. Desorption fluence used: 0.6 J/cm² over 320 µm spot. **(A)** Positive polarity mass spectrum with zoom on m/z 134. **(B)** Kendrick mass-defect plot from (A), zoomed on 55<m/z<230; see full, conventional mass-defect plot in Fig. S2A. Arrows indicate alkylation (+CH_2) series for hydrocarbons (blue) and sulfurized molecules (red). See main text for peak assignments and associated symbol colors. Alkylbenzene, alkylbenzothiophene, and alkylthiophene series are further supported by GC-MS data.

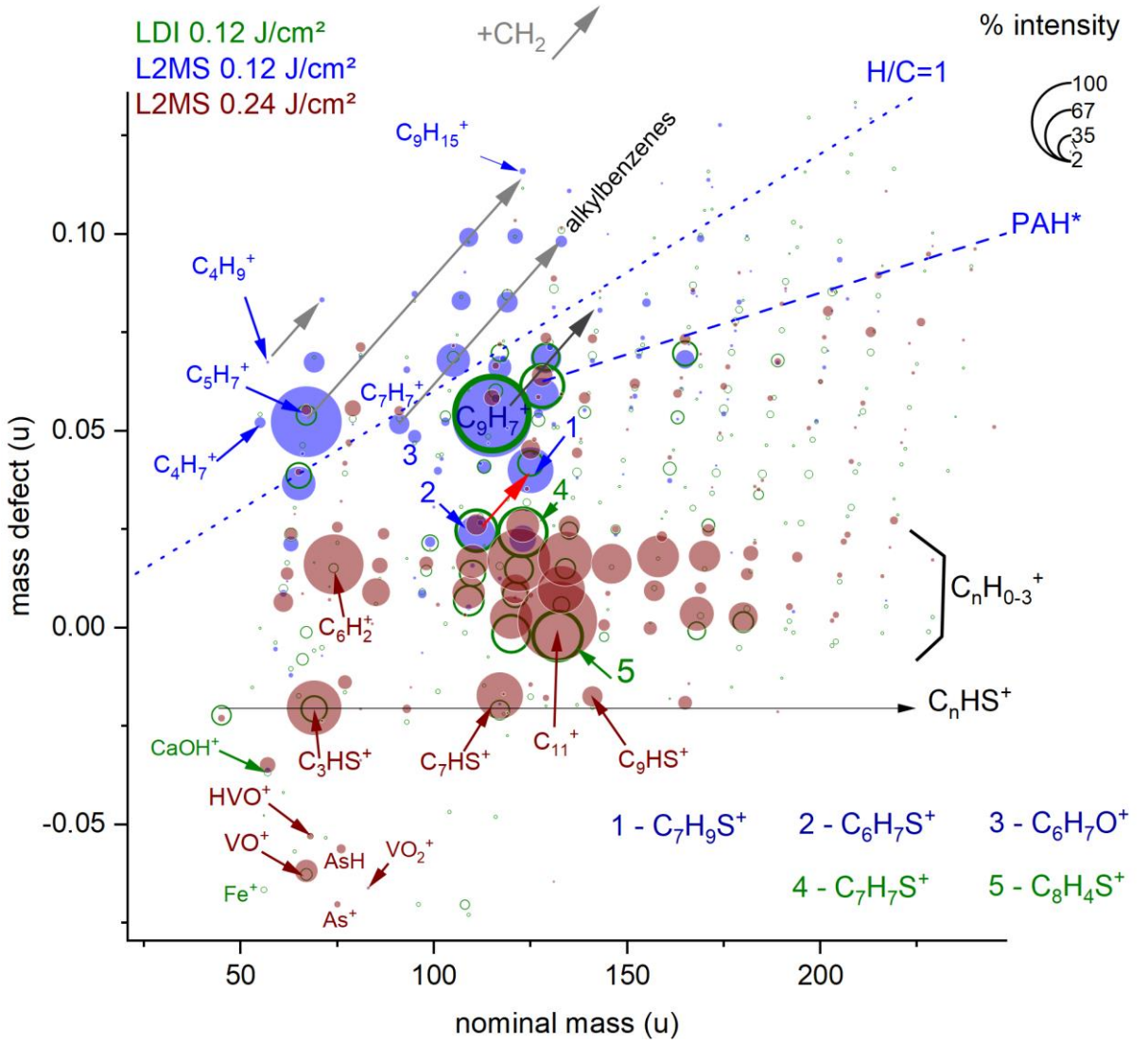

Fig. 3. ORBA3 bitumen, mass-defect plots of LDI-MS and L2MS positive-polarity mass spectra recorded using 532 nm desorption. Zoomed-out version in Figs. S2B and S3B-E. Desorption fluence was 0.12 J/cm² (blue symbols for L2MS, empty green symbols for LDI-MS) or 0.24 J/cm² in L2MS (brown symbols). The L2MS ionization laser (λ = 266 nm) had a fluence of 0.14 J/cm^2. Initial external calibration with fullerene, final calibration with $C_nH_{0-3}^+$ clusters performed internally for LDI-MS at 0.12 J/cm² and L2MS at 0.24 J/cm² desorption, and performed externally for L2MS at 0.12 J/cm² using the peak positions of these clusters in the 0.24 J/cm² experiment. The upper blue-dotted line shows the H/C ratio frontier, and the PAH* line shows the upper mass-defect limit of non-alkylated PAH compositions defined by catacondensed PAHs; these lines apply only to C_xH_y species. In contrast to Kendrick mass-defect plot, here alkylation series (+CH_2) appear as ~diagonals (grey lines for hydrocarbons, red line for alkylthiophenes).

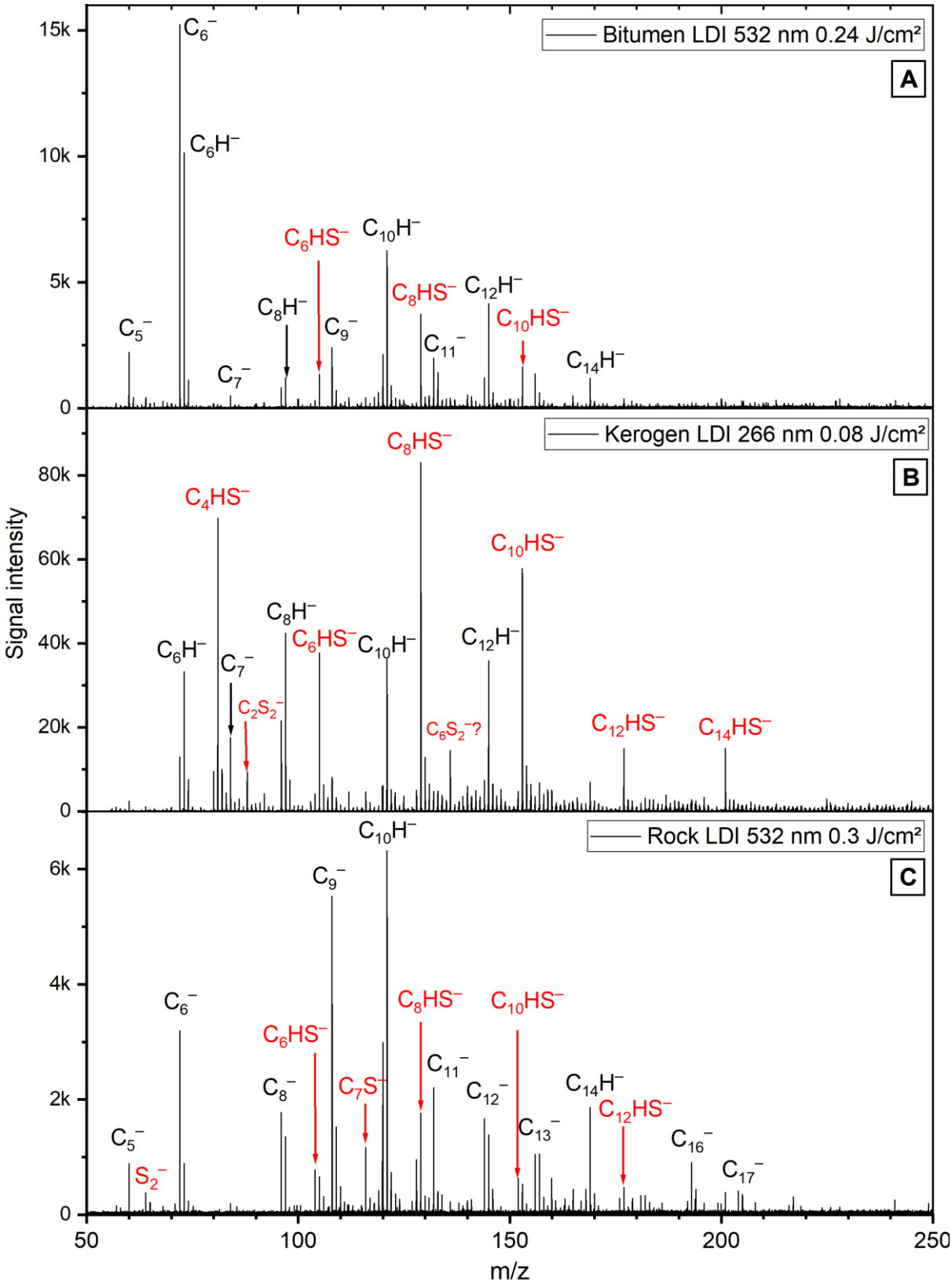

Fig. 4. ORBA3 subsamples, negative polarity LDI-MS spectra. Desorption wavelengths and fluences, and sample types are indicated in insets.

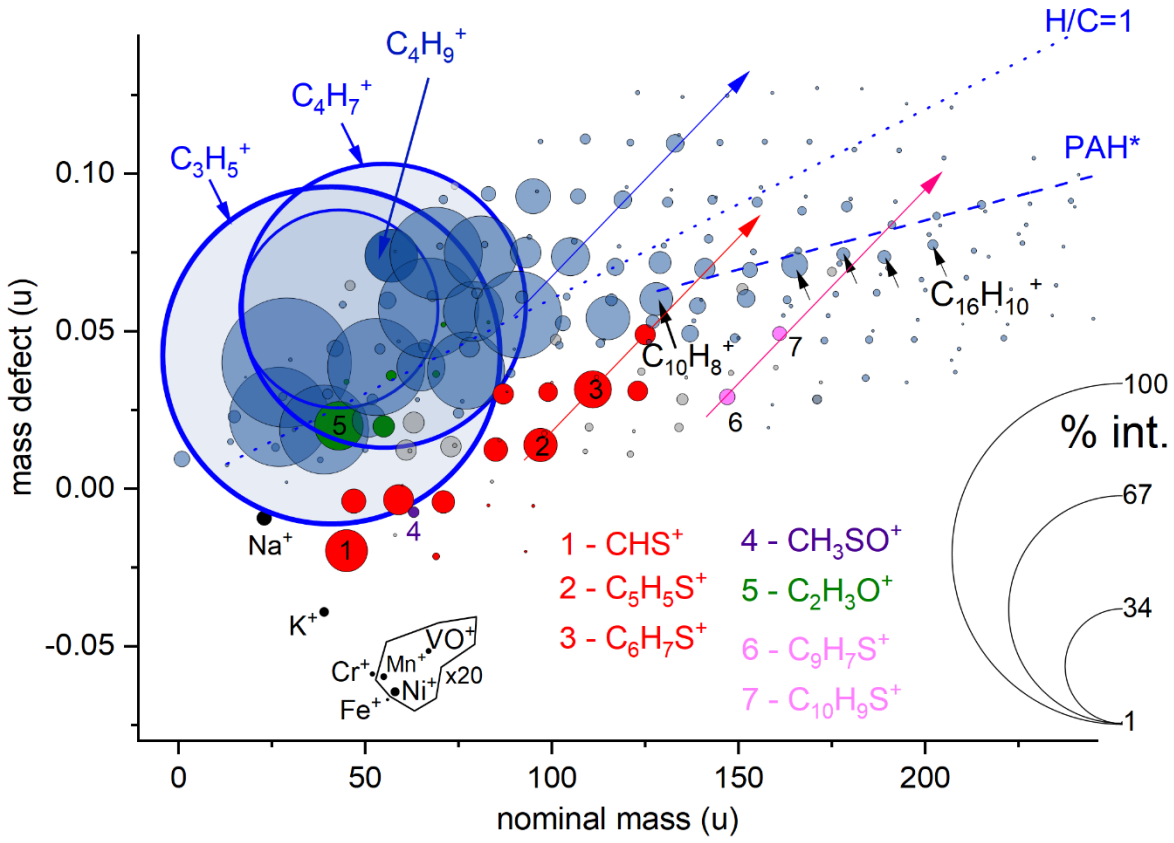

Fig. 5. ToF-SIMS of the ORBA3 bitumen, mass-defect plot generated from the positive polarity mass spectrum. Spots in red and pink indicate sulfur-bearing species, spots in blue are assigned to hydrocarbons (although some may include S-species), and grey spots remain unassigned. Colored arrows highlight the positions of alkylation (+CH_2) series of alkylbenzenes (blue), alkylthiophenes (red), and alkyl-benzothiophenes (pink). Black arrows indicate PAHs.

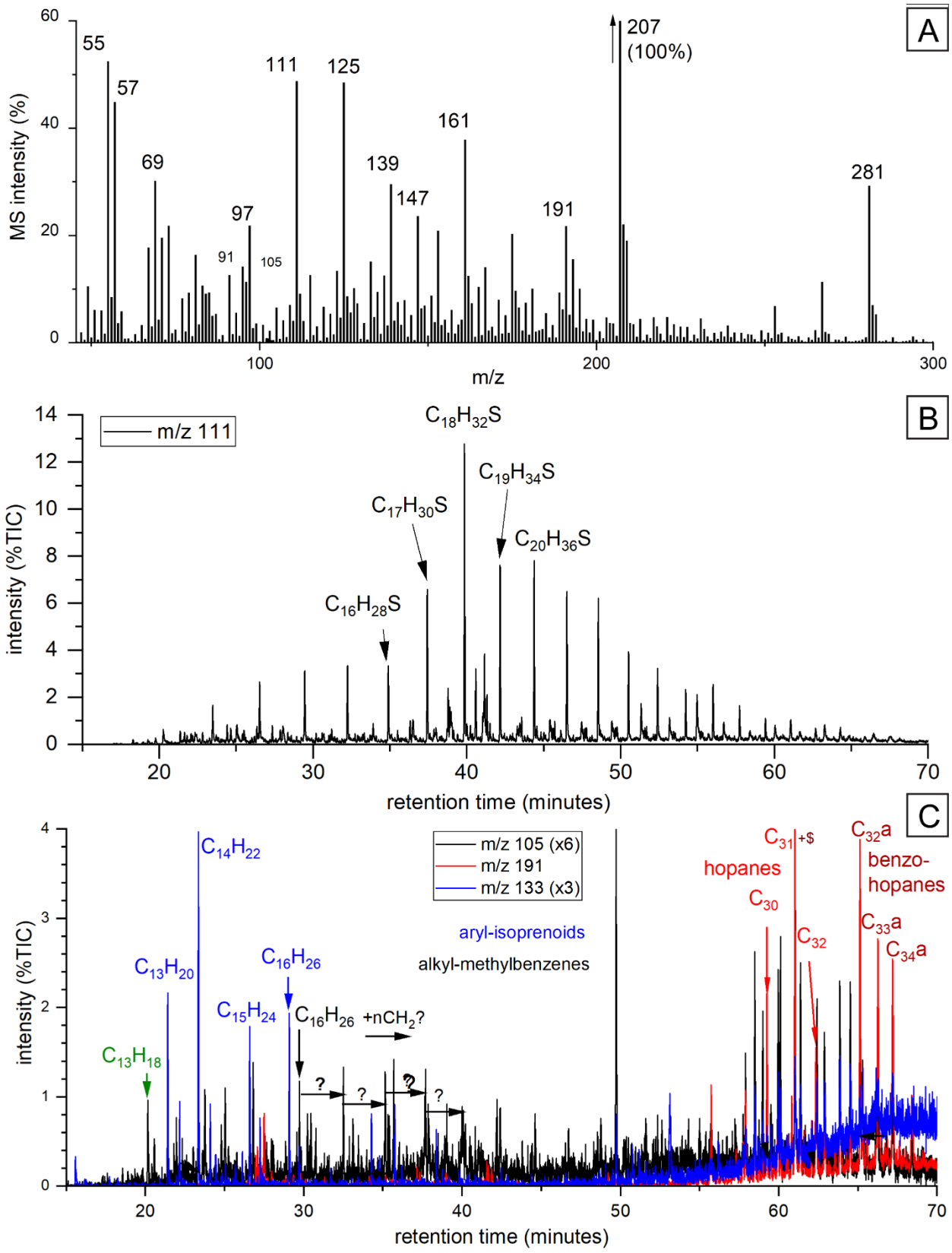

Fig. 6. GC-MS of the bitumen of Orbagnoux sample DP. (A) Total GC-MS mass spectrum obtained by integrating all mass spectra for all retention times. The signals at m/z 207 and 281 are dominated by column bleed. **(B)** Mass chromatogram of m/z 111 showing series of alkyl-methylthiophenes. **(C)** Mass chromatograms of m/z 105, 133 and 191 showing alkylated aromatics including benzohopanes, alkyl-methylbenzenes and benzohopanes, as well as

hopanes (and e.g., C_{32}-hopene, $, co-eluting with C_{31}-hopane). Ion intensities in B-C are normalized to the maximum intensity of the total ion chromatogram (TIC= total ion count, here measured at a given retention time).

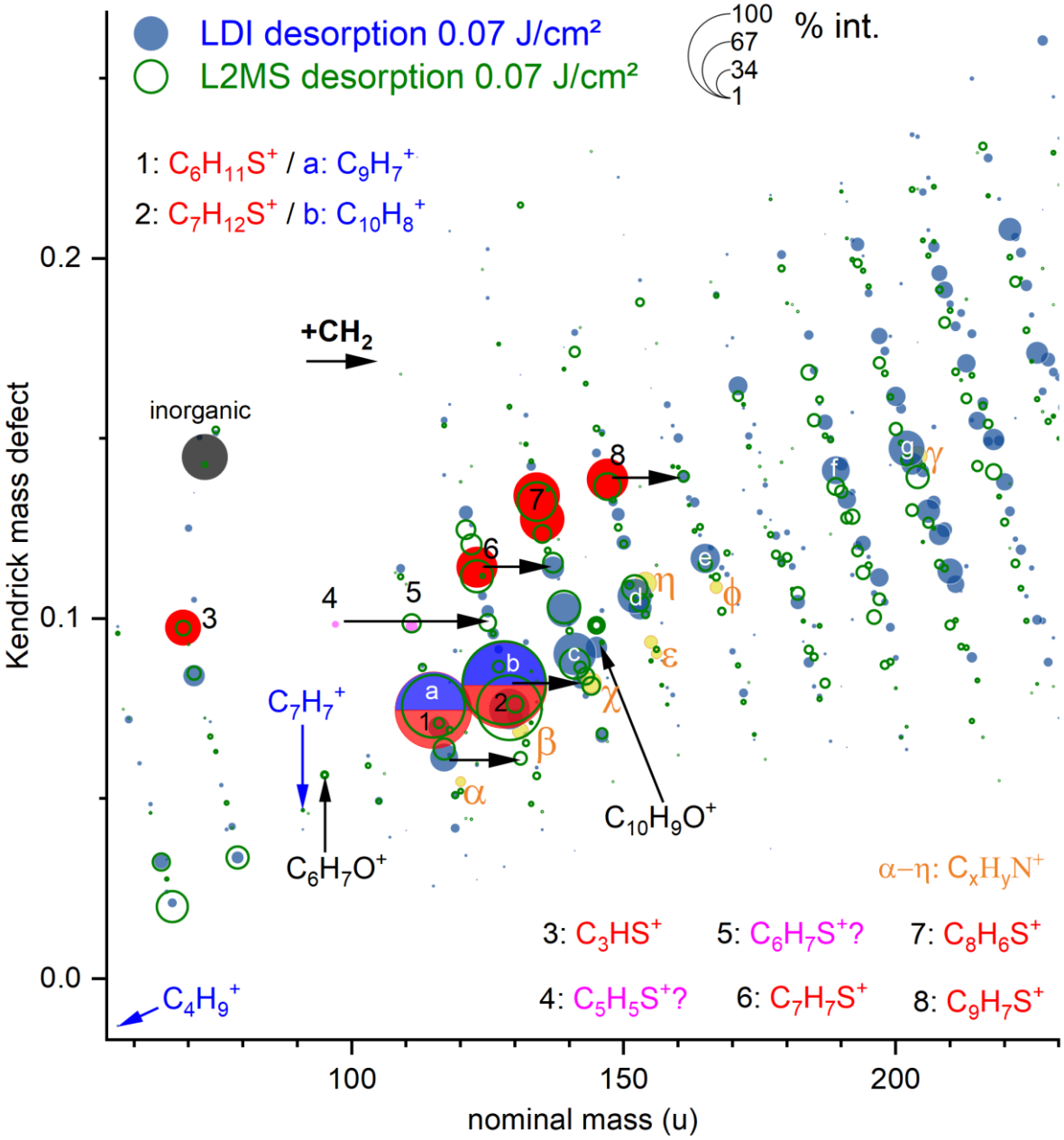

Fig. 7. ORBA3 kerogen analyzed with L2MS and LDI-MS, in positive polarity, using desorption at 266 nm. Mass defect plot from positive polarity spectra recorded in LDI-MS and L2MS, with 0.07 J/cm² fluence for desorption, and 0.08 J/cm² fluence for ionization at 266 nm in L2MS. See Figs. S2C and S3F-G for full spectra. L2MS peaks shown in open green circles. In the LDI-MS spectrum, species identified as sulfurated molecules are shown in red, peaks with likely interference of hydrocarbons and sulfurated molecules are shown in blue/red combination disks, peaks assigned to $C_xH_yN^+$ in yellow (α–η), and other peaks without isotope support to assignments are shown in dark blue. Peaks 4, 5 (pink) are tentatively attributed to sulfurated fragments. Peaks (a-g) are attributed to PAHs (see main text).

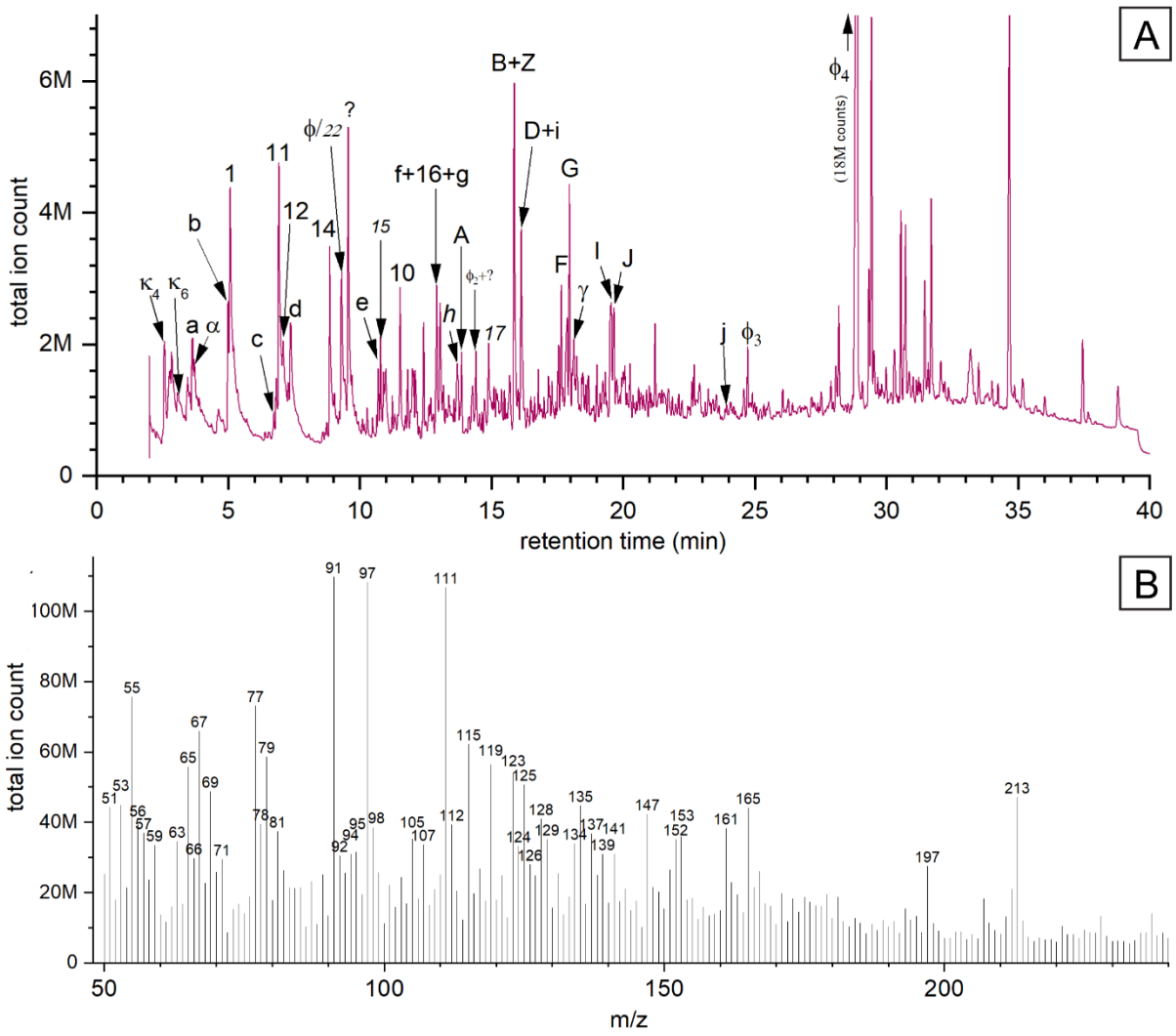

Fig. 8. ORBA3 kerogen pyrolysis at 600°C. (A) Total ion count chromatogram showning: Alkenes: κ_4 (C_4H_8), κ_6 (C_6H_{12}). **Aromatic hydrocarbons**: a (benzene), b (toluene C_7H_8), c (ethylbenzene C_8H_{10}), d (xylene C_8H_{10}), e (indene C_9H_8), f (tetramethylbenzene $C_{10}H_{14}$), g (methylindene, $C_{10}H_{10}$), h (naphthalene $C_{10}H_8$), i (2-methylnaphtalene $C_{11}H_{10}$), j (likely phenanthrene $C_{14}H_{10}$), **alkylthiophenes:** 1 (methylthiophene C_5H_6S), 10 (butenylthiophene $C_8H_{10}S$), 11 (dimethylthiophenes C_6H_8S), 12 to 17 (alkyl-methylthiophenes: $C_{n=1-5}H_{2n+1}C_5H_5S$), 22 (trimethylthiophene $C_7H_{10}S$). **Benzothiophenes:** A (benzothiophene C_8H_6S), B and D (methylbenzothiophenes C_9H_8S), F and G (dimethyl- or ethyl-benzothiophenes $C_{10}H_{10}S$), J(ethyl-methylbenzothiophene $C_{11}H_{12}S$). **Thiophenes (other)**: α (thiophene, C_4H_4S), γ (phenylthiophene $C_{10}H_8S$), I (methylenedithiophene $C_9H_8S_2$). **Phenols:** ϕ (phenol, C_6H_6O), ϕ_2 (bisphenol A derivative?, $C_9H_{12}O$), ϕ_3 (bisphenol A derivative?, $C_{15}H_{16}O$), ϕ_4 (bisphenol A, $C_{15}H_{16}O_2$). **(B) Total GC-MS mass spectrum**.

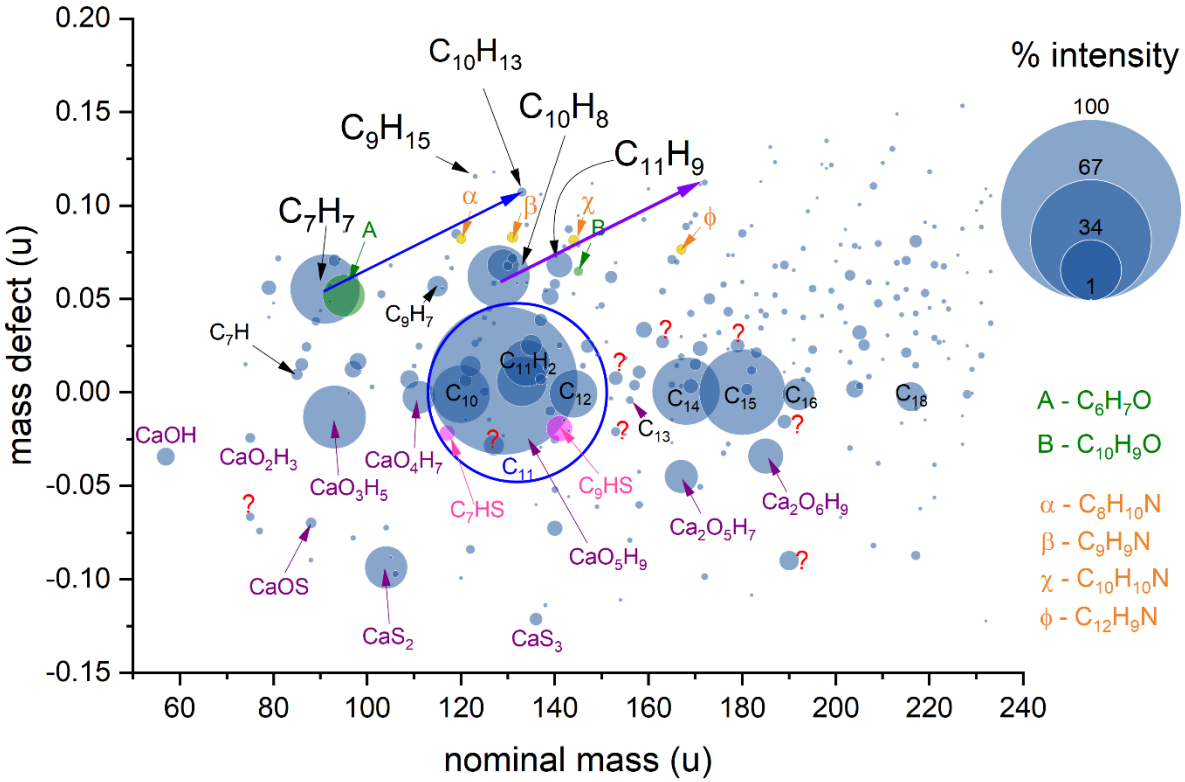

Fig. 9. Freshly-fractured rock: mass-defect plot from L2MS spectrum recorded at 0.2 J/cm² desorption fluence (532 nm) with 0.05 J/cm² ionization laser (266 nm), positive polarity. Blue and purple arrows indicate alkyl-benzene and alkyl-naphthalene series, respectively.

Characterization of sulfur-rich microbial organic matter in Jurassic carbonates using laser-assisted mass spectrometry

S. Thlaijeh, K. Lepot, Y. Carpentier, A. Riboulleau, D. Duca, M. Vojkovic, A. Tewari, J. Sarazin, M. Bon, N. Nuns, N. Tribovillard, C. Focsa

Supplementary Materials

Table S1

	ion formula assignments †	exact m/z	error ppm ‡	H/C	RDBE (¥)	pattern
A1	**C7H7+**	**91.0542**	**-1.1**	**0.9**	**5**	**97.3**
comment on formula attribution: single candidate						
B1	C2H7O5+	111.0288	-20.4	3	0	85.5
B2	**C6H7S+**	**111.0263**	**2.1**	**1**	**4**	**89.5**
B3	H5N3O4	111.0275	-8.3	n/a	0.5	86.3
comment on formula attribution: B1 unlikely compound with 5 oxygens; B3: unlikely ionorganic species in the bitumen; peak at m+2 (m/z 113.x) for the 34S isotopologue of B2 (see Fig. S1)						
C1	C5H8N2O2+	128.058	29.1	1.4	3.5	21
C2	**C10H8+**	**128.0621**	**-2.3**	**0.7**	**7.5**	**25.8**
C3	***C7H12S+***	***128.0654***	***-28.6***	***1.6***	***2.5***	***43.8***
comment on formula attribution: C1 unlikely N2O2 compound; C3: 34S-isotopologue shoulder not seen at m+2 (130.x m/z), but high contribution of C10H10+ or other compound at m+2; mixture of C1+C3 compounds remains possible						
D1	**C10H9+**	**129.0699**	**2.5**	**0.8**	**7**	**80.6**
D2	**C7H13S+**	**129.0732**	**-23.7**	**1.7**	**2**	**68.2**
comment on formula attribution: D2: 34S-isotopologue shoulder very clear at m+2 (131.x m/z); mixture of D1+D2 compounds is still likely with an important contribution of D1 suggested by the position of the peak being closer to that of D1 (less error for the D1 assignment)						
E1	**C11H10+**	**142.0777**	**-14.1**	**0.8**	**7.5**	**30.3**
E2	C6H10N2O2+	142.0737	14.2	1.5	3.5	25.5
comment on formula attribution: E2 unlikely N2O2 compound						
F1	C13H9NO2+	211.0628	-28.3	0.6	10.5	49.4
F2	C5H13N3O4S+	211.0621	-25.3	2.4	1.5	50
F3	C11H7N4O+	211.0614	-22	0.5	11	48.9
F4	C11H15S2+	211.061	-19.8	1.3	5	57.4
F5	C10H11O5+	211.0601	-15.6	1	6	48.6
F6	C8H9N3O4+	211.0588	-9.3	1	6.5	48.1
F7	**C14H11S+**	**211.0576**	**-3.8**	**0.7**	**10**	**52.4**
F8	C6H15N2O2S2+	211.0569	-0.7	2.3	1	53.1
F9	C17H7+	211.0542	12.2	0.4	15	50.5
F10	C9H11N2O2S+	211.0536	15.3	1.1	6	51.1
F11	C7H17NS3+	211.0518	23.9	2.3	0.5	58.6
F12	C6H13NO5S+	211.0509	28	2	1.5	50.2
comment on formula attribution: F7: 34S-isotopologue shoulder at m+2 (m/z 213.x). F9 is unlikely due to very low H/C (unknown molecule) and may only represent a fragment / fragment cluster ion, which is not expected in this experiment due to low abundance of Cn+ clusters in the mass spectrum; other moieties appear unlikely (c.f. main heteroatom classes observed in LDI-FTICR by Cho *et al.* (2012)						
†	assignments made with mMass allowing an error in mass of ±30 ppm					
‡	error in mass assignements in ppm = 10^6*(measured m/z - assigned ion exact m/z)/(measured m/z)					
¥	RDBE = Ring + double-bond equivalent = 1 + (#C atoms) - 0.5*(#H atoms) + 0.5*(#N atoms)					
pattern	correspondance of the mass spectrum with calculated isotope pattern					
colors indicate assignments made; see main text for explanation						

Table S2

Analysis parameters			Figure(s)	ions	main results
desorption (ionization)		post-ionization			
λ (nm)	fluence (J/cm²)	fluence (J/cm²)			
ORBA3 bitumen					
266	0.6	n/a (LDI-MS)	2, S1, S2A, S3A	+	$C_xH_y^+$ with including alkylbenzenes, alkyl-PAHs, and high H/C series including $C_5H_7(CH_2)_n^+$
					$C_xH_yS^+$ ion with $+(CH_2)_n$ series, likely alkylthiophenes, alkylbenzothiophenes, etc..
					$C_6H_7O^+$ and $C_{10}H_9O^+$ main oxygenated species
					$C_6H_7N^+$ main N species
					$C_nH_{0-3}^+$ and C_nHS^+ clusters absent
532	0.12	0.14	3, S2B, S3B	+	$C_xH_y^+$ with consistent with alkylbenzenes, alkyl-PAHs, and high H/C series including $C_5H_7(CH_2)_n^+$; predominance of the high H/C compounds over (alkyl)-PAHs and sulfurated ions
					Small alkylthiophenes
532	0.12	n/a (LDI-MS)	3, S2B, S3C	+	decreased $C_xH_y^+$ compred to above L2MS analysis
					inorganics detected (V, As, Ca, Fe,…. species)
					low H/C sulfur-bearing ions (e.g., $C_8H_4S^+$) increase compared to L2MS = fragments?
					$C_nH_{0-3}^+$ and C_nHS^+ clusters
532	0.24	0.14	3, S2B, S3D	+	now good detection of the inorganics in L2MS
					$C_nH_{0-3}^+$ and C_nHS^+ clusters now dominant
532	0.24	n/a (LDI-MS)	S3E		$C_nH_{0-3}^+$ and C_nHS^+ clusters dominant
532	0.24	n/a (LDI-MS)	4A	-	$C_nH_{0-3}^-$ and C_nHS^- clusters, mostly
ToF-SIMS 25 kV Bi_3+	primary ions 0.29 pA	n/a	5	+	dominance of small, high H/C fragments ($C_3H_5^+$, $C_4H_7^+$, $C_4H_9^+$), alkylbenzenes, PAHS
					S-molecules, likely small alkylthiophenes and alkylbenzothiophenes
					fragmented S-molecules, including CHS^+
					inorganics including Na^+, K^+, Cr^+, Fe^+, Mn^+, Ni^+, VO^+
ORBA3 kerogen					
266	0.07	n/a (LDI-MS)	7	+	PAHs appear abundant (± short alkyl chains); faint alkylbenzenes
					weak signal of high H/C $C_xH_y^+$, in particular at m/z<100
					Thiophene, benzothiophene abundant ± their alkylation series likely (difficult to identify with isotoplogues due to faint signal), limited to short chains.
					higher signal at m/z >175 compared to bitumen
					$C_6H_7O^+$ and $C_{10}H_9O^+$ main oxygenated species
					nitrogenated species not seen in bitumen
266	0.07	0.08	7	+	main difference compared to LDI-MS (above):
					increased signal / additional peaks of higher H/C ions at low Kendrick mass defect
266	0.07	n/a (LDI-MS)	4B	-	$C_nH_{0-3}^-$ and C_nHS^- clusters, mostly, additional $C_2S_2^-$
ORBA3 rock					
532	**0.2**	**0.05**	**9**	**+**	**$C_xH_y^+$ dominated by $C_7H_7^+$ and small PAHs, with small number of alkylations**
					$C_6H_7O^+$ and $C_{10}H_9O^+$ main oxygenated species
					some of the N species seen in kerogen also detected
					$C_nH_{0-3}^+$ and C_nHS^+ clusters dominant
					abundant inorganics, likely various Ca-bearing clusters
532	0.3	n/a (LDI-MS)	4C	-	$C_nH_{0-3}^-$ and C_nHS^- clusters, mostly

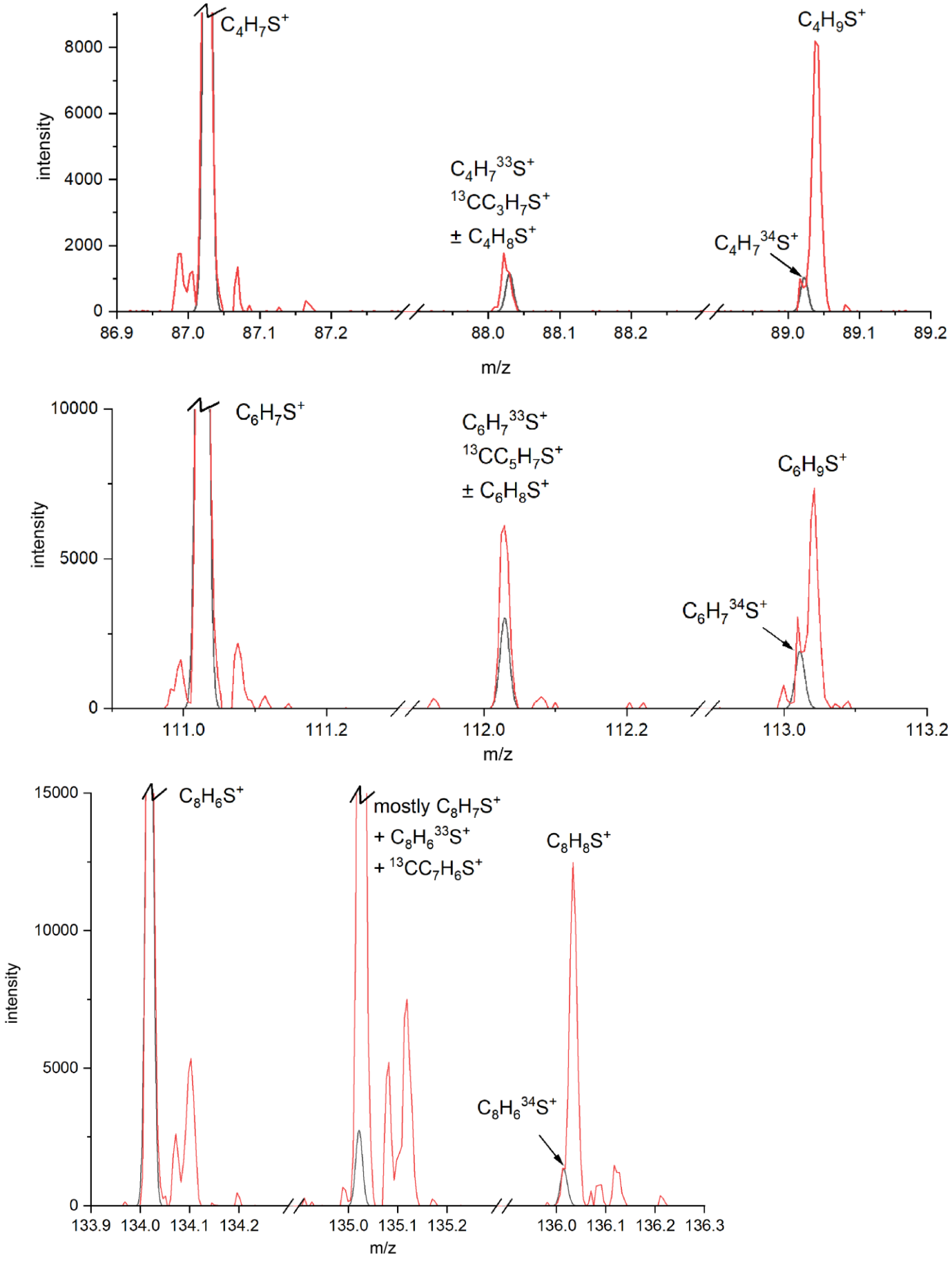

Fig. S1. Examples of isotope patterns generated using mMass (in grey) compared to LDI-MS spectra (in red) recorded on bitumen using 266 nm desorption (c.f. Fig. 2).

S2**a – Bitumen 266 nm LDI-MS**

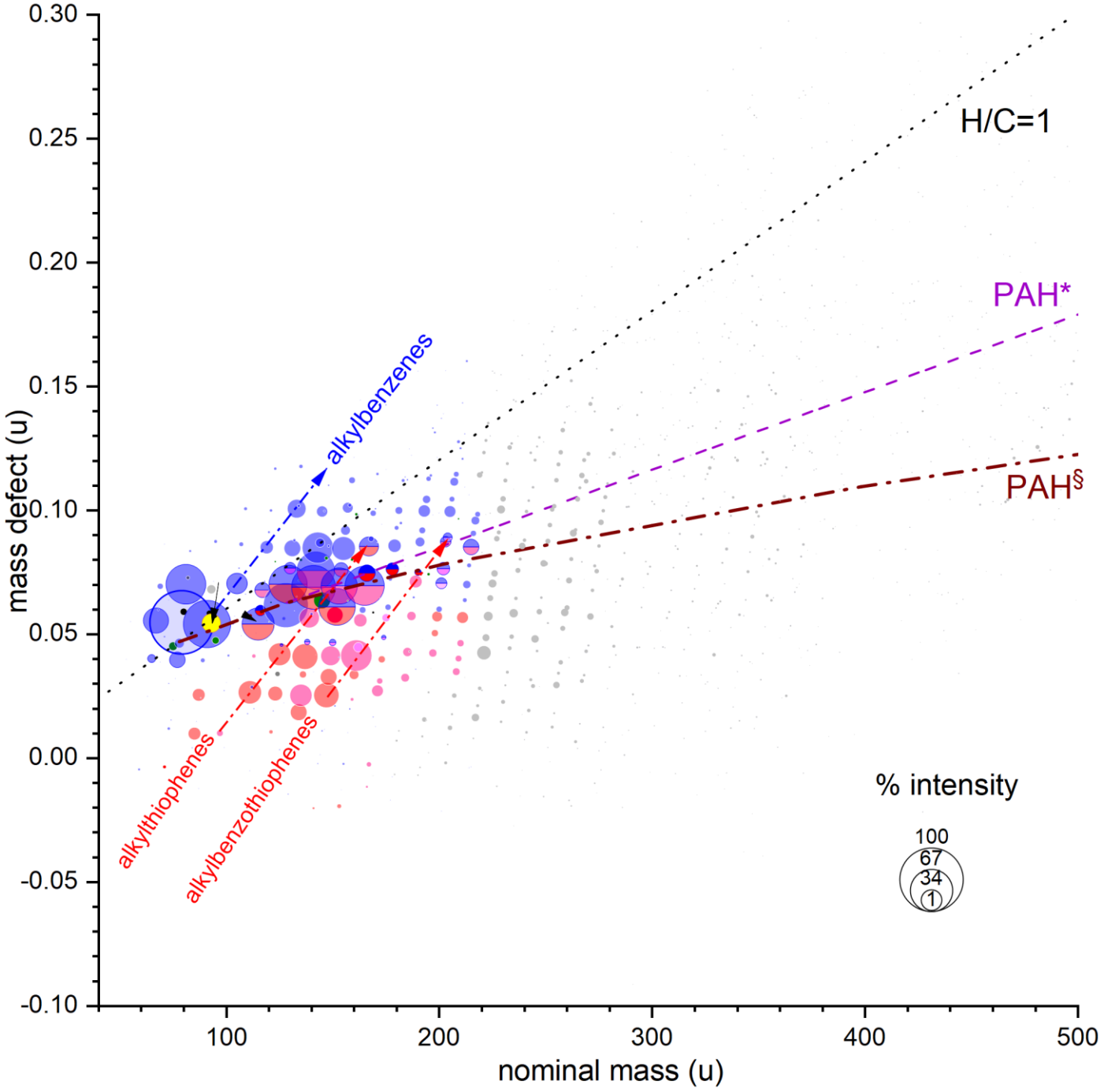

Fig. S2. Mass-defect plots recorded on **(a)** ORBA3 bitumen with 266 nm (LDI-MS) desorption-ionization, from the spectrum of Fig. 2 and S3A, **(b -next page)** LDI-MS and L2MS of ORBA3 bitumen with 532 nm desorption-ionization (LDI-MS) or 532 nm desorption with 266 nm ionization (L2MS), see zoom with detailed color code in Fig. 3, and spectra in Figs. S3B-D, (**c – following page**) Mass-defect plots of kerogen in LDI-MS and L2MS (see color codes in Fig. 7 and associated spectra in Fig. S3F-G).

In (A-C) the upper dotted lines show the H/C ratio frontier applicable for C_xH_y species only, the dashed purple lines (PAH*) show the upper mass-defect limit of non-alkylated PAH compositions defined by catacondensed PAHs and the dash-dot brown lines ($PAH^{§}$) show the composition domain of pericondensed PAHs. Vertical and horizontal scales and position of the scales are nearly equivalent for (a-c) for ease of comparison of the general mass distribution patterns. Note the higher masses and mass-defects observed in the kerogen in (c) .

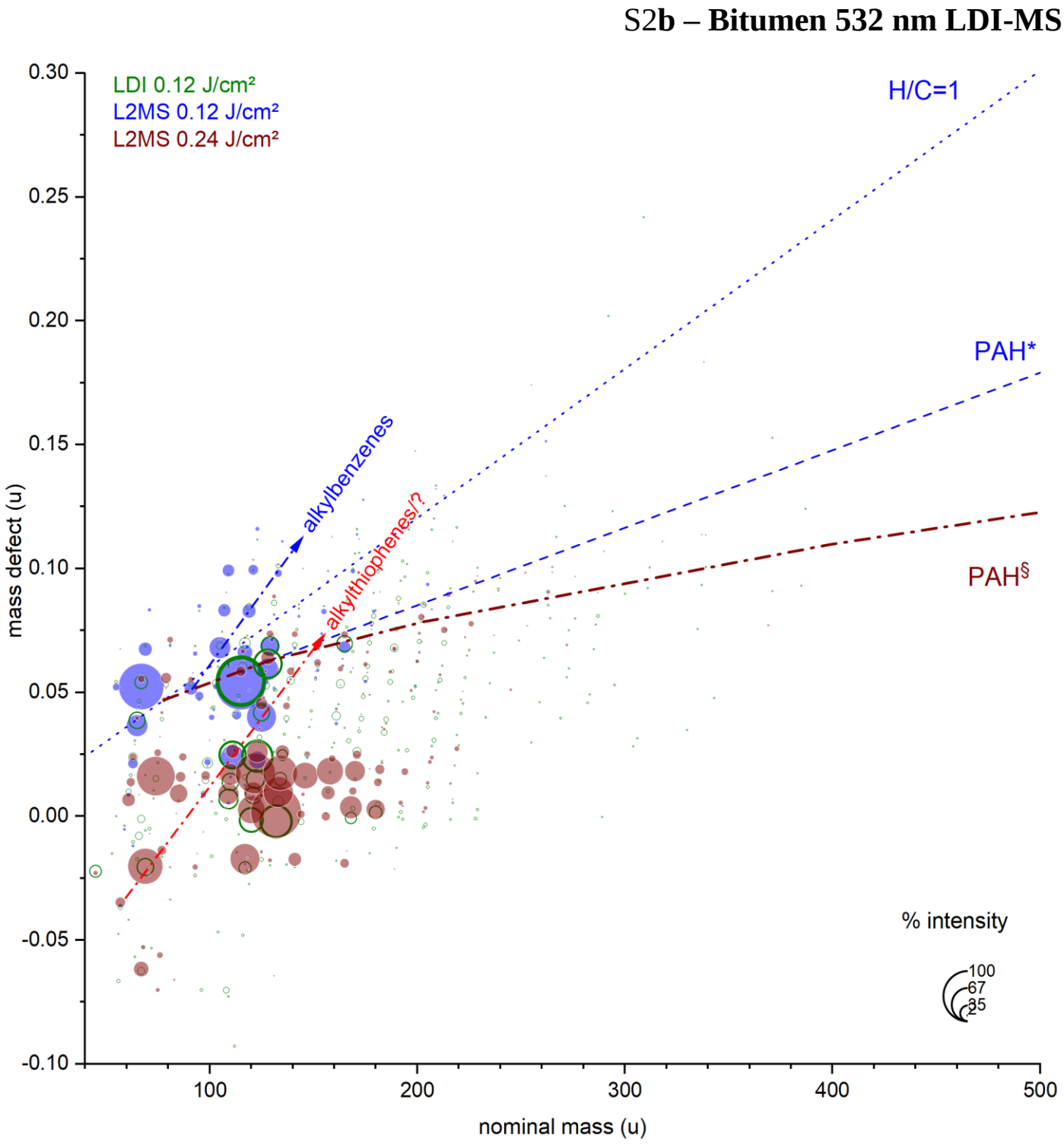

Fig. S2, continued

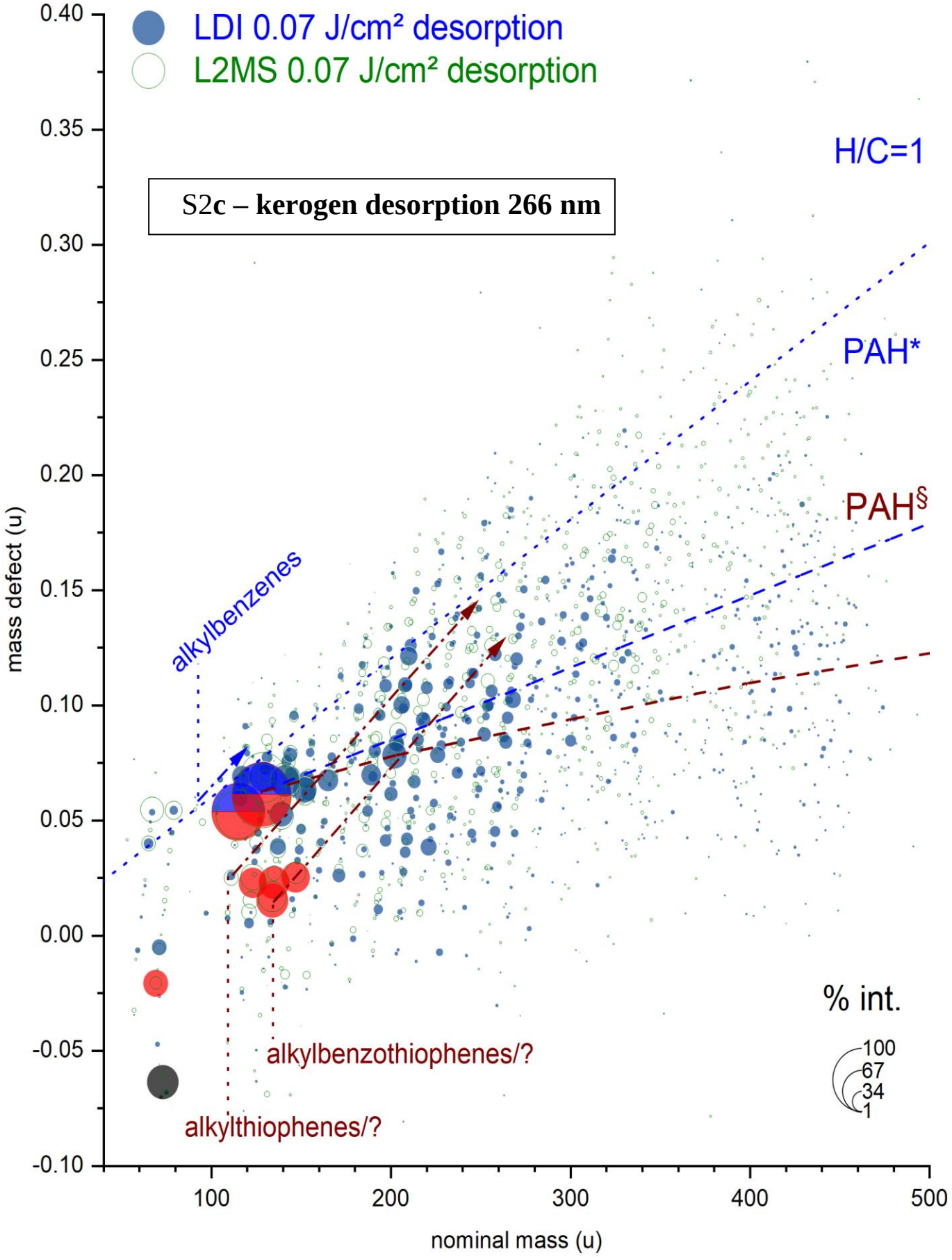

Fig. S2, continued

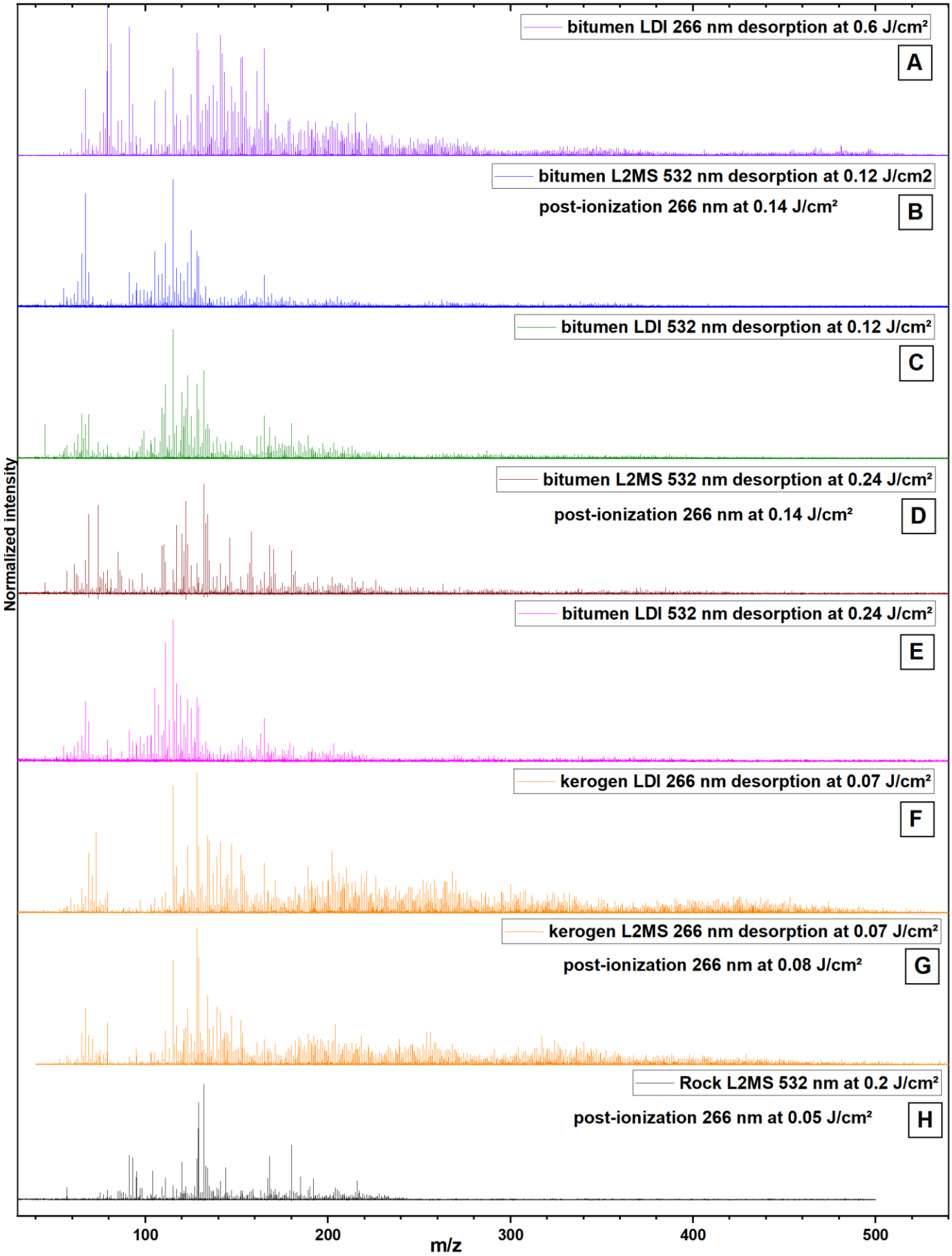

Fig. S3. LDI-MS and L2MS mass spectra recorded on ORBA3 bitumen, kerogen and rock subsamples (analytical conditions in insets). Colors used in A-G correspond to those used in Table S2.

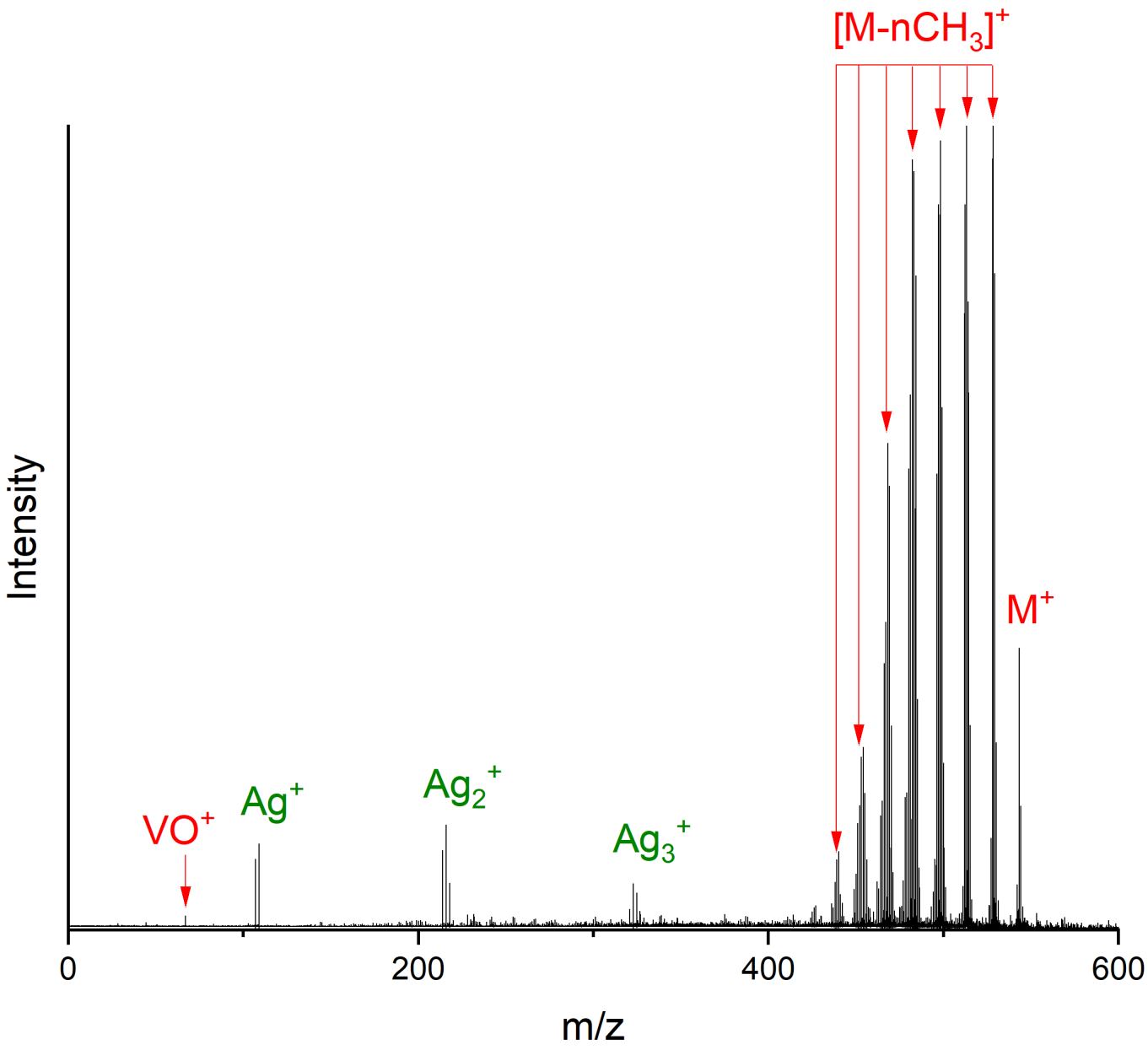

Fig. S4. L2MS spectrum of vanadium etioporphyrin ($C_{32}H_{36}N_4OV$) reference molecule, deposited on a silicon wafer in dichloromethane, after deposition of an $AgNO_3$ calibration standard. Desorption performed using 532 nm at <0.07 J/cm² (100 µJ over a 420 µm-large elliptic spot), ionization at 266 nm (8.9 mJ).

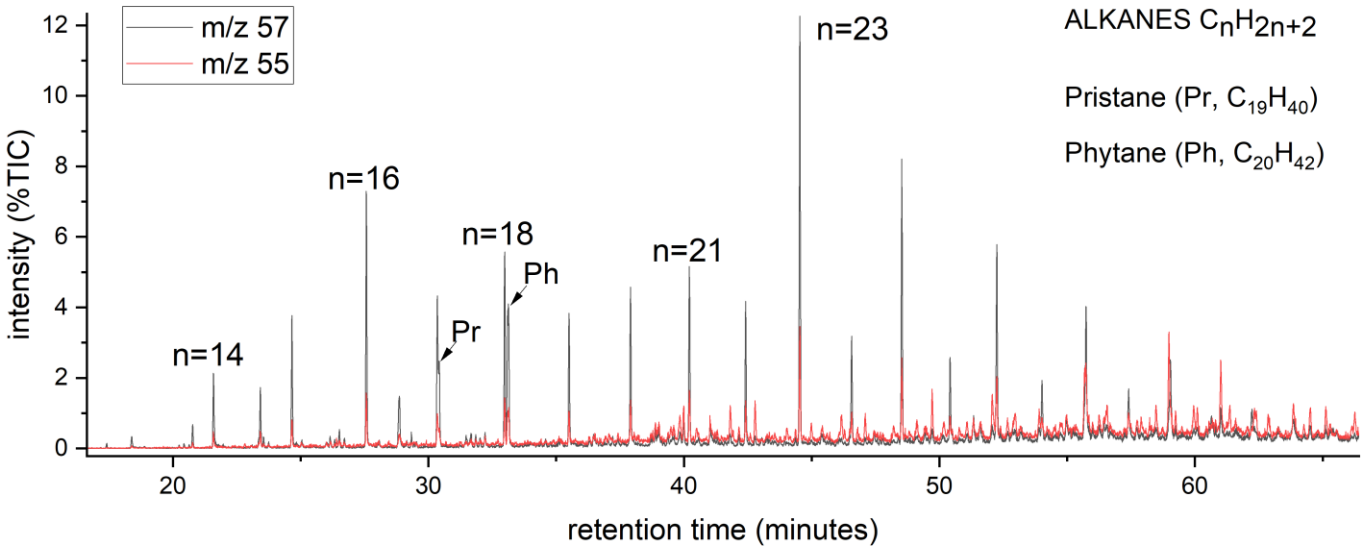

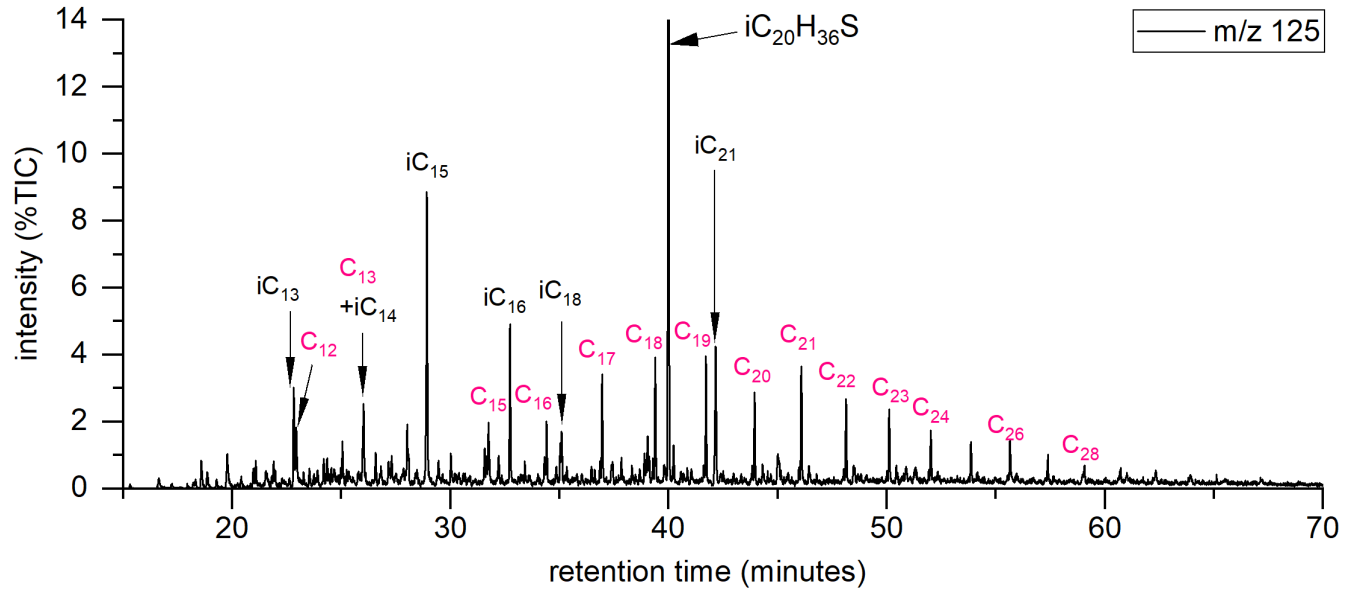

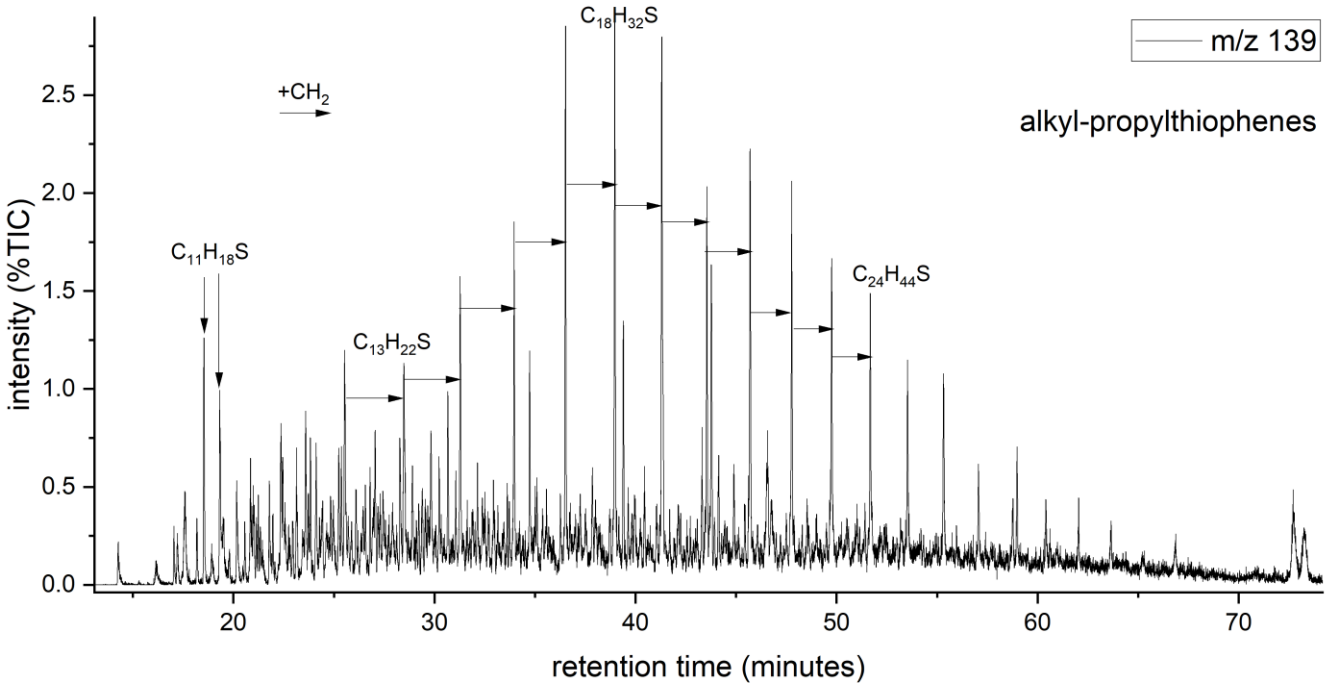

Continued and legend next page.

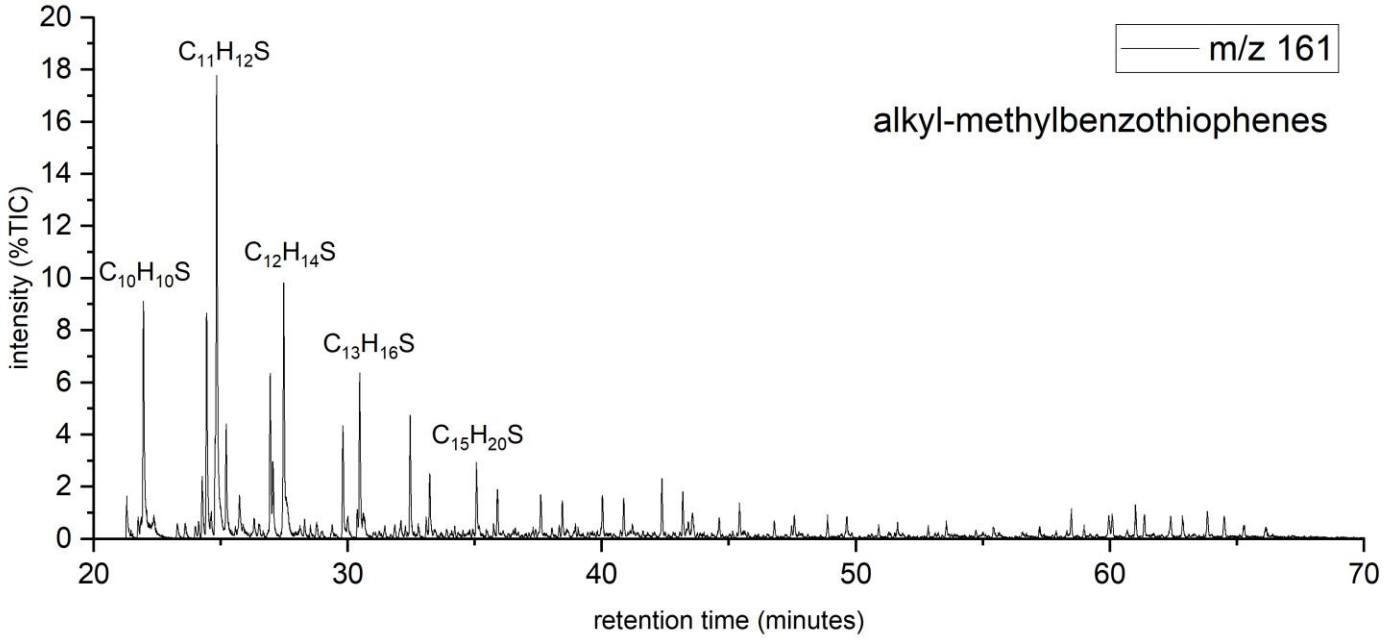

Fig. S5. GC-MS of the bitumen of Orbagnoux sample DP, selected mass chromatograms. **Both m/z 57 and 55** are dominated by alkane fragments. **The peaks at m/z 125** comprise a series of *n*-alkyl-ethylthiophenes (indicated by C_y, with y = total C number), and a series of isoprenoid alkylthiophenes (indicated by iC_y) including the base peak assigned to 2,3-dimethyl-5-(2,6,10-trimethylundecyl)thiophene ($iC_{20}H_{36}S$), and isoprenoid thiophene with a phytane skeleton that has also been identified in Orbagnoux by van Kaam-Peters and Sinninghe Damsté (1997). **The signal at m/z 139** is dominated by alkyl-propylthiophenes. **That at m/z 161** is dominated by alkyl-methylbenzothiophenes. Note that the most intense peak of the ion chromatogram at m/z 97 (not shown) had an intensity (relative to TIC) of 1.25%, showing the low abundance of alkylthiophenes relative to the alkyl-methylthiophenes.

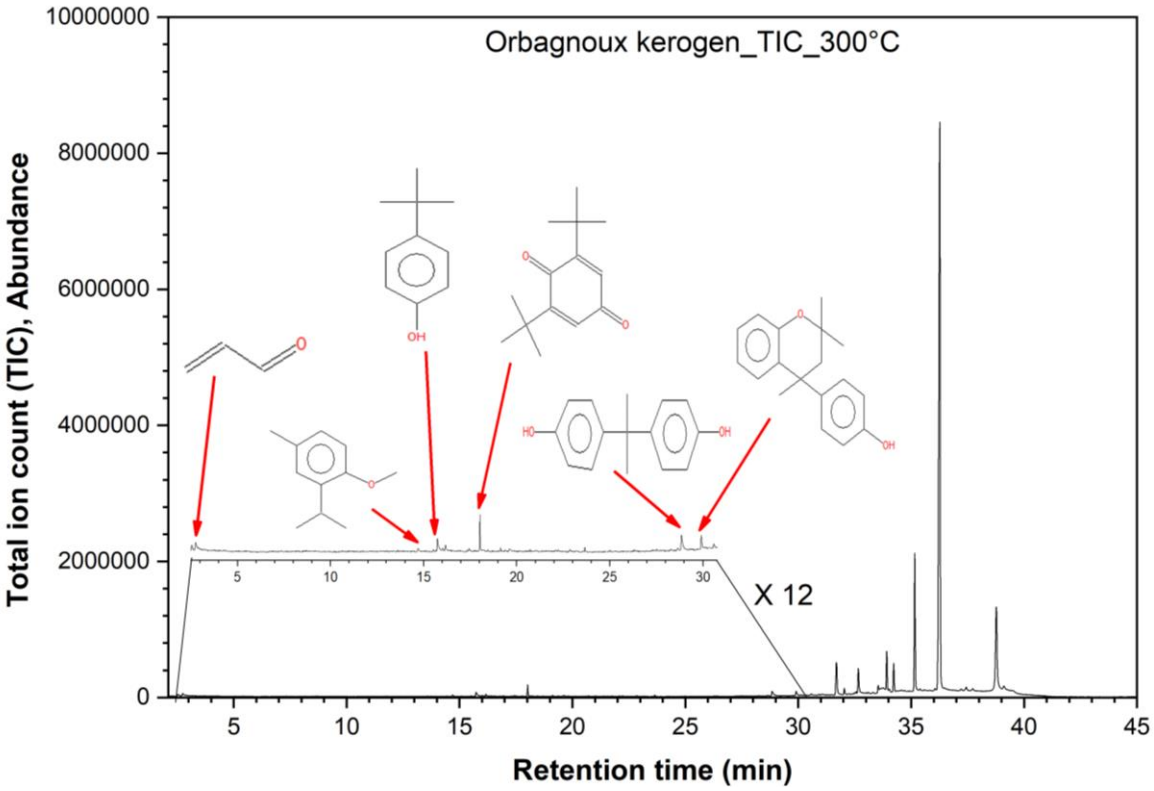

Fig. S6. Total ion count (TIC) chromatogram of Orbagnoux kerogen at 300 °C. We detected propenal (C_3H_4O) at 2.733 mins; 1-methoxy-4-methyl-2-(1-methylethyl)benzene ($C_{11}H_{16}O$, m=164 u.), 14.692 mins; p-tert-butyl-phenol ($C_{10}H_{14}O^+$, m= 150 u.) at 15.733 mins; 2,6-bis(1,1-dimethylethyl)-2,5-cyclohexadiene-1,4-dionecyclohexadiene-dione ($C_{14}H_{20}O_2^+$, m/z 220), at 18.017 mins; 4,4'-(1-methylethylidene)bis-phenol ($C_{15}H_{16}O_2$, m/z 228 – bisphenol A) at 28.842 mins, and 4-(3,4-dihydro2,2,4-trimethyl-2H-1-benzopyran-4-yl)-phenol ($C_{18}H_{20}O_2^+$, m/z 268) at 29.908 mins. Note that some of the main peaks recorded in the pyrolysis at 600°C are not detected here (benzene, toluene, dimethylthiophene, naphthalene, methylbenzothiophene, etc.). Chemical structures shown here were generated using the software NIST MS Search 2.3.

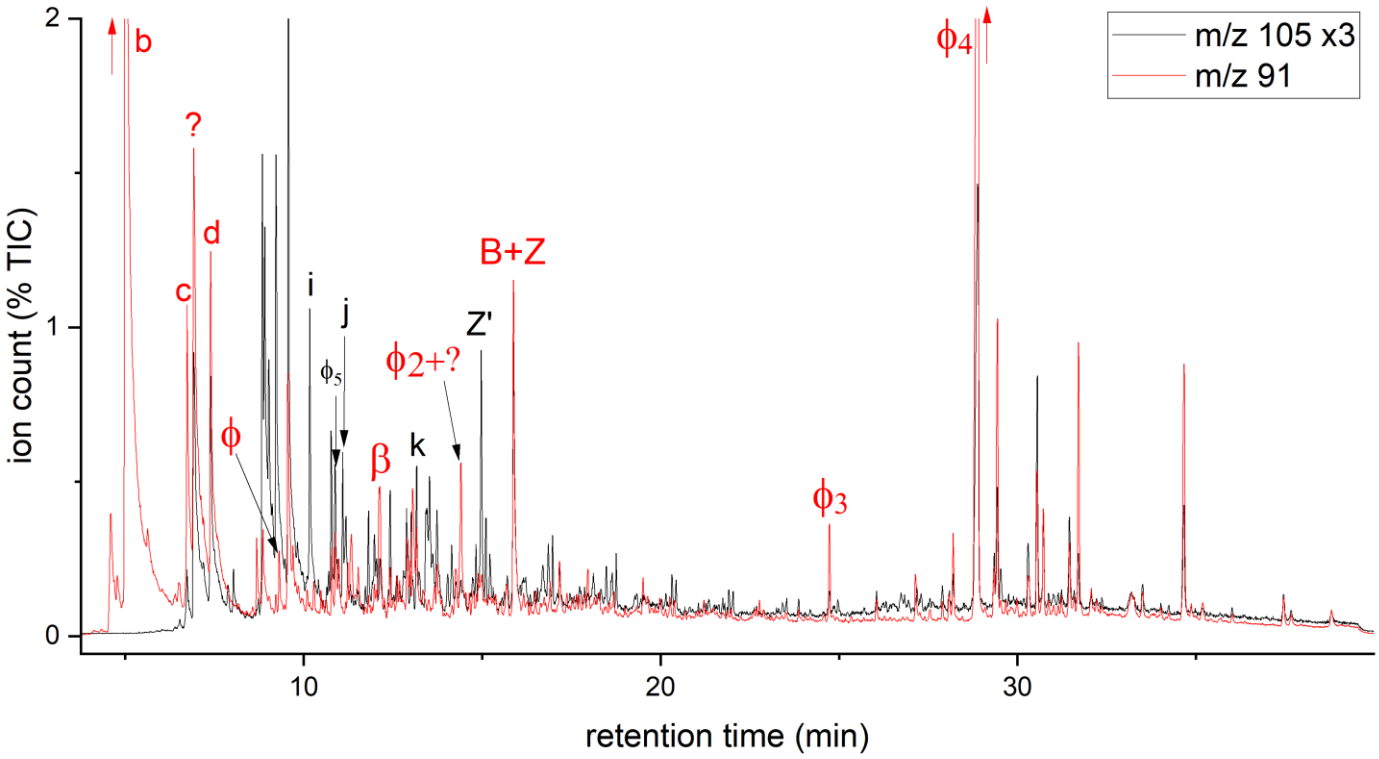

Fig. S7. Orbagnoux kerogen, 600°C pyrolysis GC-MS, selected ion mass chromatograms. Peaks indicated in red come from the m/z 91 ion signal, and those from in black from the m/z 105 ion signal; they comprise alkylbenzenes and functionalized alkylbenzenes: b (toluene C_7H_8), c (ethylbenzene C_8H_{10}), d (xylene C_8H_{10}), i (ethyl-methylbenzene, C_9H_{12}), j (methyl-propylbenzene, $C_{10}H_{14}$), k (tetrahydronaphthalene, $C_{10}H_{12}$), B (methylbenzothiophenes C_9H_8S), ϕ (phenol, C_6H_6O), ϕ_5 (2-Me-phenol), ϕ_2 (bisphenol A fragment?, $C_9H_{12}O$), Z'(2,5-dimethyl-Benzaldehyde, $C_9H_{10}O$), Z (Isopropenylphenol $C_9H_{10}O$), ϕ_3 (bisphenol A fragment?, $C_{15}H_{16}O$), ϕ_4 (bisphenol A, $C_{15}H_{16}O_2$).

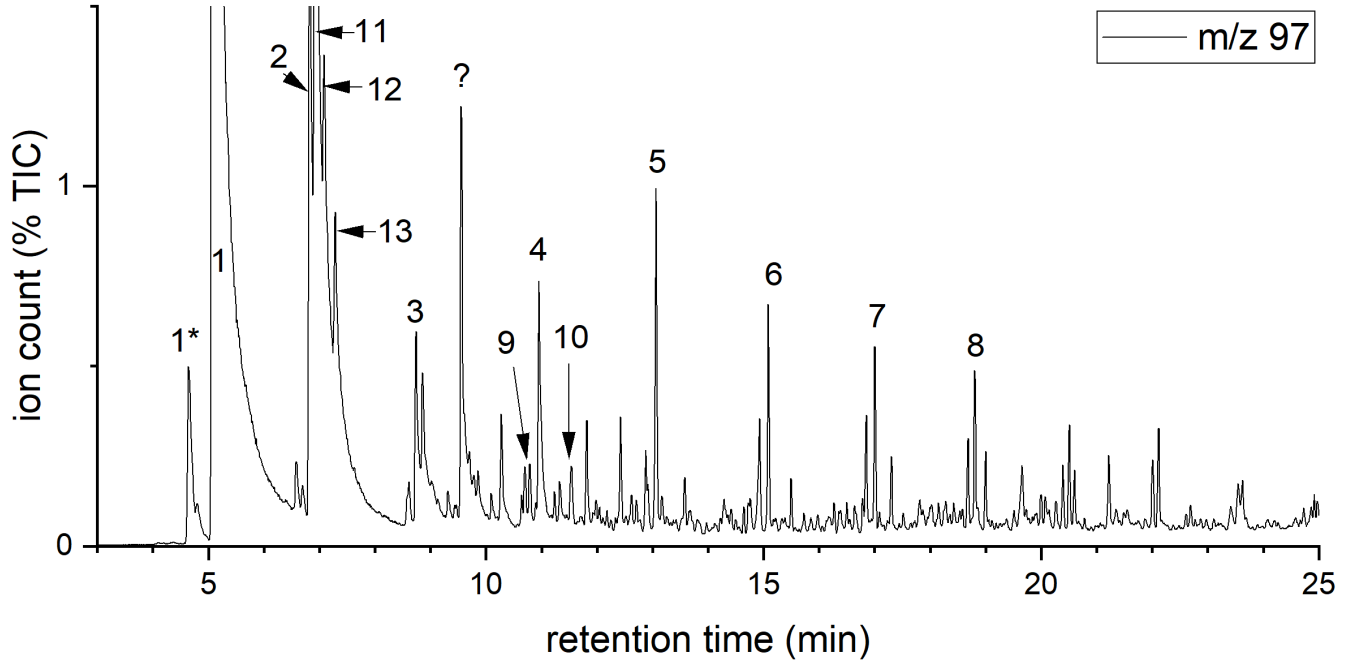

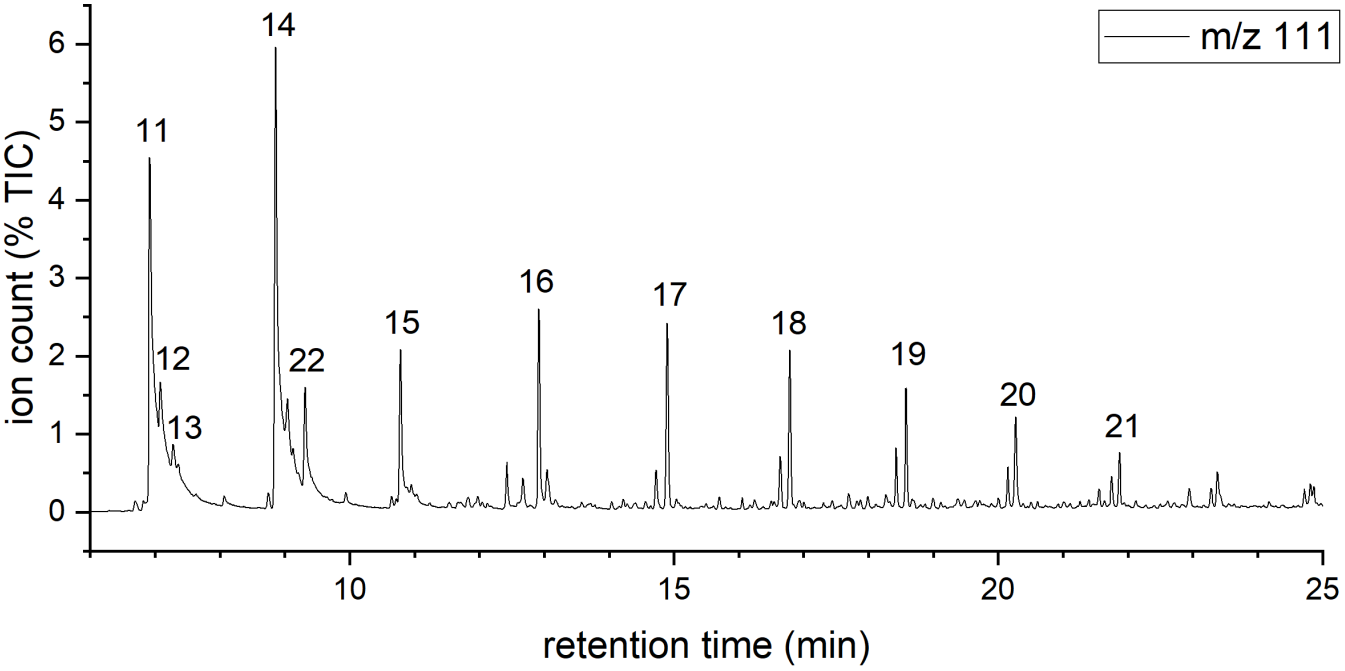

***n*-alkylthiophenes**

1/1* - methylthiophene C_5H_6S
2 - ethylthiophene C_6H_8S
3 - propylthiophene $C_7H_{10}S$
4 - butylthiophene $C_8H_{12}S$
5 - pentylthiophene ? $C_9H_{14}S$
6 - hexylthiophene $C_{10}H_{16}S$
7 - heptylthiophene $C_{11}H_{18}S$
8 - octylthiophene $C_{12}H_{20}S$

alkyl-methylthiophenes

11-13 dimethylthiophenes C_6H_8S
14 - ethyl-methylthiophene $C_7H_{10}S$
15 - methyl-propylthiophene $C_8H_{12}S$
16 - butyl-methylthiophene $C_9H_{14}S$
17 - methyl-penthylthiophene $C_{10}H_{16}S$
18 - hexyl-methylthiophene $C_{11}H_{18}S$
19 - heptyl-methylthiophene $C_{12}H_{20}S$
20 - methyl-octylthiophene $C_{13}H_{22}S$
21 - methyl-nonylthiophene $C_{14}H_{24}S$

other

9 - diethylthiophene $C_8H_{12}S$
22 - trimethylthiophene $C_7H_{10}S$
10 - butenylthiophene $C_8H_{10}S$

Fig. S8. Orbagnoux kerogen, 600°C pyrolysis GC-MS, selected ion mass chromatograms. At m/z 97, *n*-alkyl-thiophene molecules (noted 1-8) dominate, along with a few other thiophene-related molecules (9, 10, and 22). **At m/z 111**, alkyl-methylthiophenes dominate.

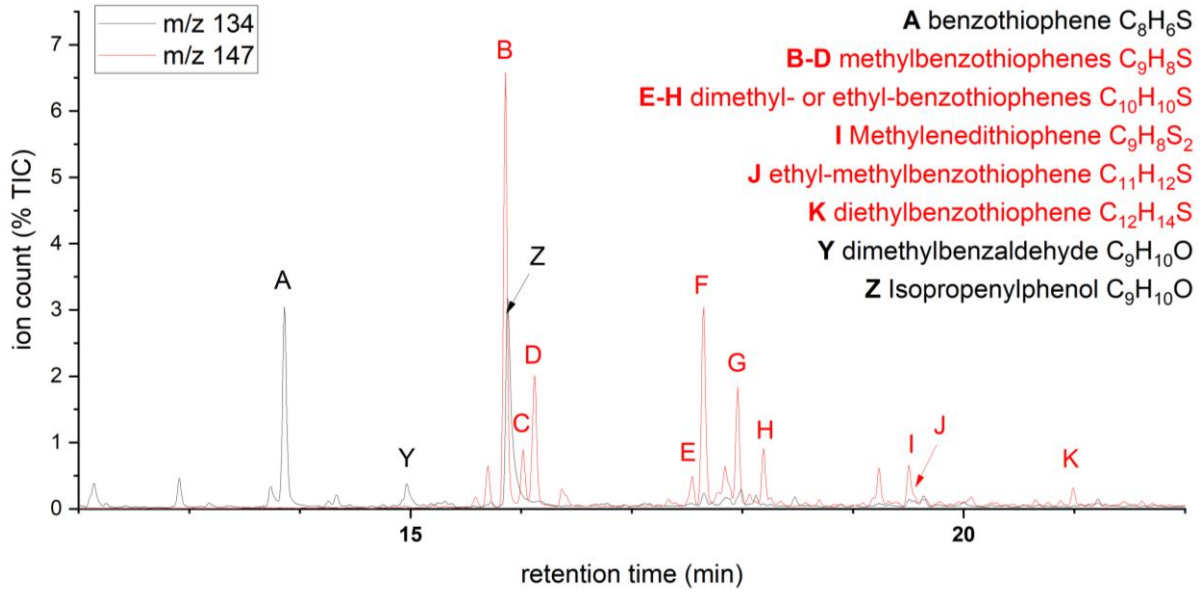

Fig. S9. Orbagnoux kerogen, 600°C pyrolysis GC-MS, selected ion mass chromatograms. Showing the main molecules contributing to **m/z 134** (named A, Y and Z) and the dominance of alkylbenzothiophenes (B to K) at **m/z 147**.

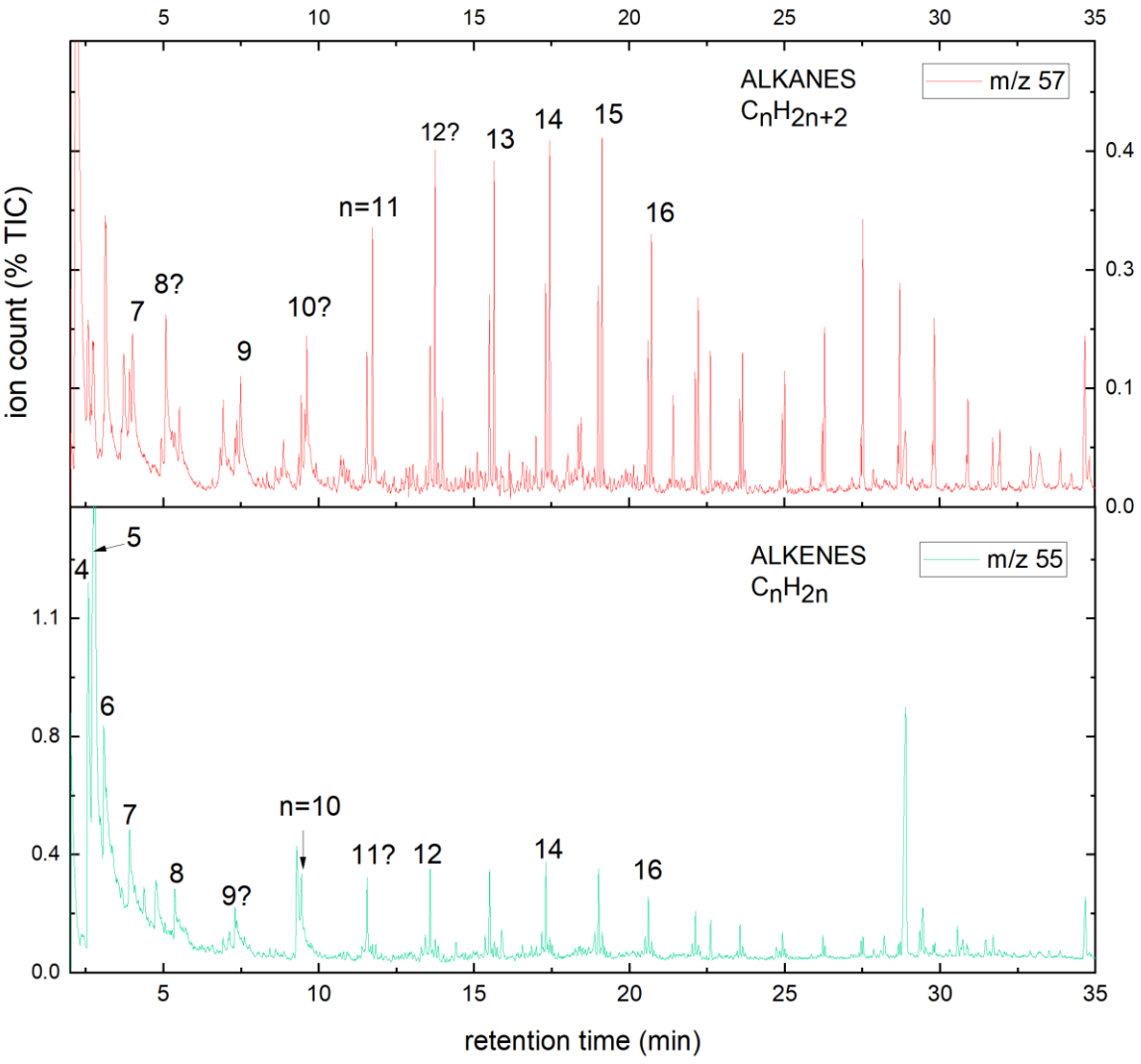

Fig. S10. Orbagnoux kerogen, 600°C pyrolysis GC-MS, selected ion mass chromatograms. The mass chromatograms at m/z 57 and m/z 55 are dominated by *n*-alkanes and *n*-alkenes, respectively (*n* values shown with each peak).

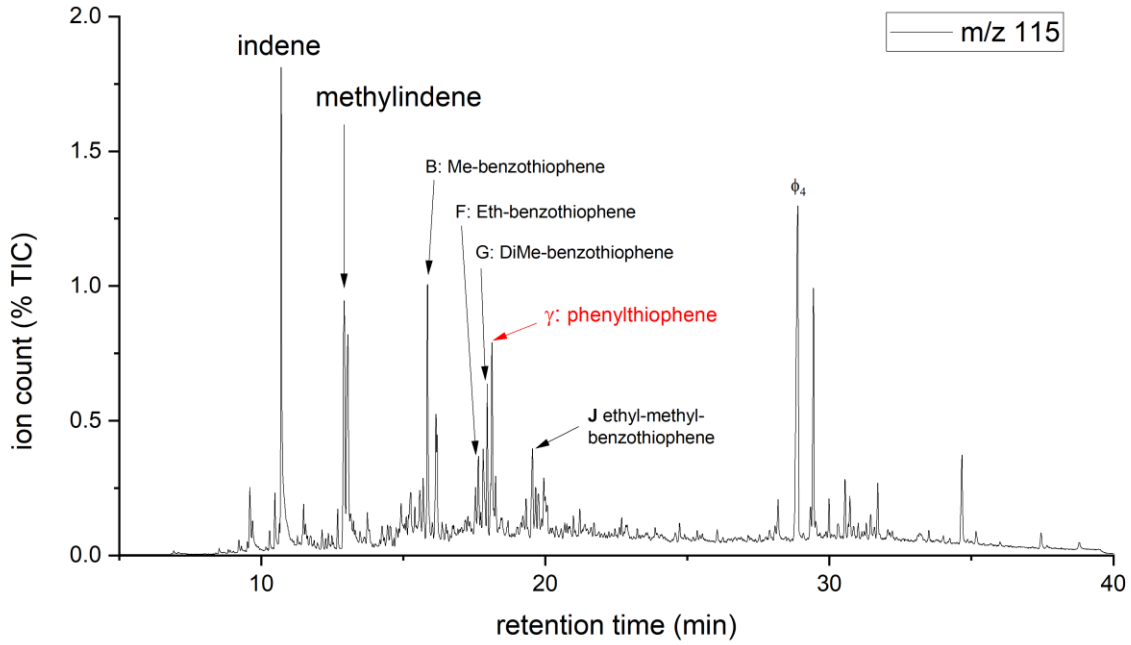

Fig. S11. Orbagnoux kerogen, 600°C pyrolysis GC-MS, selected ion mass chromatogram, m/z 115, showing the main contributing molecules.

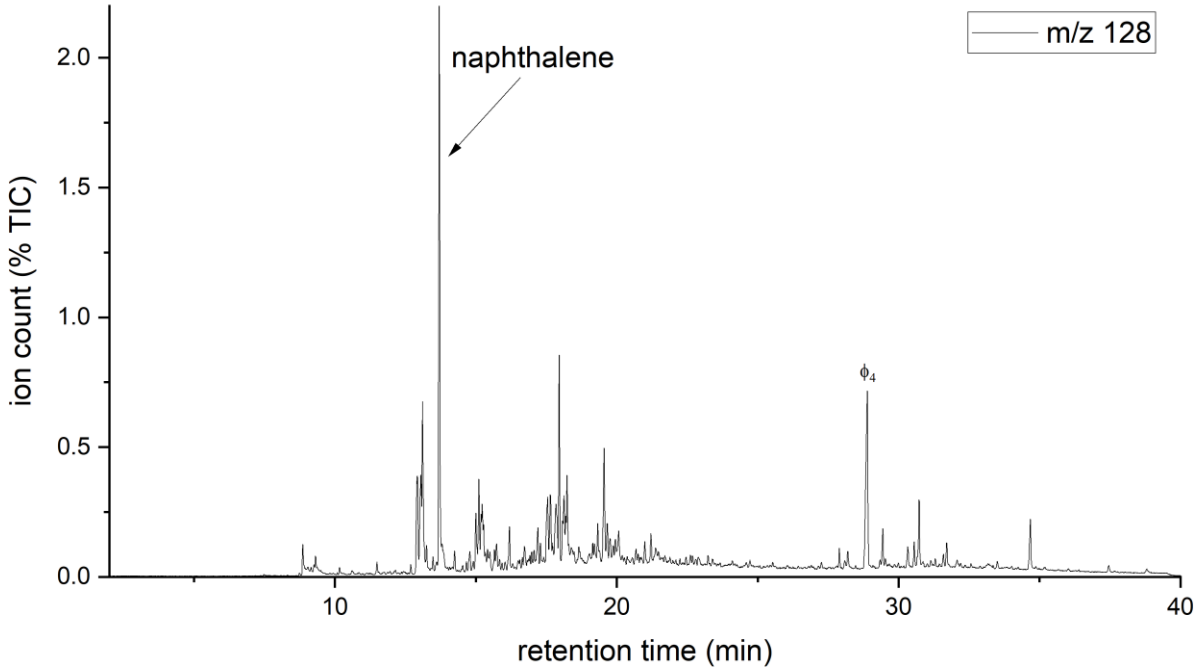

Fig. S12. Orbagnoux kerogen, 600°C pyrolysis GC-MS, selected ion mass chromatogram, m/z 128, dominated by the contribution of naphthalene.